8-1-2009

Structure-property relations for monotonic and fatigue loading conditions for a powder metal steel

Paul Galon Allison

STRUCTURE-PROPERTY RELATIONS FOR MONOTONIC AND FATIGUE LOADING CONDITIONS FOR A POWDER METAL STEEL

By

Paul Galon Allison

A Dissertation
Submitted to the Faculty of
Mississippi State University
in Partial Fulfillment of the Requirements
for the Degree of Doctor of Philosophy
in Mechanical Engineering
in the Department of Mechanical Engineering

Mississippi State, Mississippi

August 2009

STRUCTURE-PROPERTY RELATIONS FOR MONOTONIC AND FATIGUE

LOADING CONDITIONS FOR A POWDER METAL STEEL

By

Paul Galon Allison

Approved:

Mark F. Horstemeyer Center for Advanced Vehicular Systems Chair in Computational Solid Mechanics Professor of Mechanical Engineering (Major Professor)	Youssef Hammi Research Professor Center for Advanced Vehicular Systems (Committee Member)
Steven R. Daniewicz Professor of Mechanical Engineering (Graduate Coordinator)	John T. Berry Professor of Mechanical Engineering (Committee Member)
Haitham El Kadiri Research Professor Center for Advanced Vehicular Systems (Committee Member)	Sarah A. Rajala Dean of the Bagley College of Engineering

Name: Paul Galon Allison

Date of Degree: August 7, 2009

Institution: Mississippi State University

Major Field: Mechanical Engineering

Major Professor: Dr. Mark F. Horstemeyer

Title of Study: STRUCTURE-PROPERTY RELATIONS FOR MONOTONIC AND FATIGUE LOADING CONDITIONS FOR A POWDER METAL STEEL

Pages in study: 112

Candidate for Degree of Doctor of Philosophy

Developing a multi-scale math-based model for powder metallurgy (PM) component design and performance prediction requires experimental calibration and validation. Monotonic tension, compression and torsion tests were performed at various porosity and temperatures to obtain the set of plasticity and damage constants required for model calibration. Uniaxial fatigue experiments were performed to determine the constants required for capturing the low cycle and high cycle fatigue characteristics of a PM steel. Optical microscopy of the material was performed prior to testing to quantify the initial state microstrucutral characteristics of each specimen.

Tension tests on two different Bridgman notched specimens were undertaken to study the damage-triaxiality dependence for model validation. Validation of the model was further performed by monotonic component testing using PM bearing caps. Fracture surface analysis was performed using Scanning Electron Microscopy (SEM) to quantify

the void nucleation and void sizes of the different specimens. The developed model will be used for optimizing component performance and design for PM parts.

Key words: Powder Metallurgy, FC-0205, Mechanical Testing, Fatigue

DEDICATION

I would like to dedicate this dissertation to my family. Without their support I would not have had the determination and diligence to accomplish the body of work presented here. I am extremely appreciative of my sister, Georgina, who has helped shape me into the man I am today. If it would not have been for you I would have never came this far.

ACKNOWLEDGMENTS

I would first like to thank my advisor, Dr. Mark Horstemeyer, who has provided me with guidance, mentoring, and friendship that allowed me to complete this dissertation. I would also like to especially thank Dr. John Berry, Dr. Haitham El Kadiri, Dr. Youssef Hammi, Dr. Ric Carino, and Dr. Doug Bammann for their guidance and assistance. I will treasure the friendships I made while in graduate school and the many discussions I was able to have with Hayley, Brian, Tonya, Matt, Kiran, Harpreet, Laura, Wes, Claudio, Raj, Raul, Don, Stephen, John, Jason, and Joseph. I thank you very much for your friendship and kindness over the years and look forward to collaborating with you all in the future. I owe Hayley Brown special thanks for all the experimental work and assistance with my research. I would also like to thank MSU-CAVS, USAMP, and the James Worth Bagley College of Engineering for their financial assistance. Finally, I want to thank my Lord and Savior for the many blessing He has bestowed upon my life.

TABLE OF CONTENTS

LIST OF TABLES

LIST OF FIGURES

CHAPTER I

INTRODUCTION

The DOE Freedom Car/USAMP Lightweight Metals group has funded MSU to develop a database of experimental data and the associated material models for a powder metal FC-0205 steel alloy to be used in a main bearing cap, which is an engine component. In order to develop a powder metal component, the design requires models that can capture the plasticity-damage and fatigue of the associated component and material. As such, a comprehensive experimental plan that captures the structure-property relations for model correlation and validation is required.

Computational and mathematical based modeling of the thermo-mechanical behavior for powder metallurgy (PM) component design and performance prediction are recognized as significant contributions to improving efficiency, quality and cost of current production and generating new business opportunities for the automotive industry. PM techniques are being incorporated to manufacture various complex shaped engineering components, which prove difficult to cast or shape by alternative procedures. A motivating factor driving the development of a mathematical based model is the ability to accurately predict the variation in property performance caused by inhomogeneous density distribution. Research addressing mathematical modeling will provide several benefits including: near net shape components, complex geometries, high strength and

minimal or eliminated finishing operations Hammi, Stone et al. (2006). These microstructure and mechanical property tests on PM components will calibrate and validate an internal state variable (ISV) plasticity-damage model and a multistage fatigue (MSF) model allowing for accurate predictions of automotive parts.

The primary goal of this research is establishing foundations for understanding and further investigations of the issues related to calibration and validation of a math-based PM model.

Chapter II provides a theoretical study of the effect materials processed with pores have on the elastic constants. Current porosity dependent modulus models are then compared to experimental compression, tension, torsion, and ultrasound FC-0205 data.

Chapter III presents the microstructural and associated plasticity and fracture characteristics under finite deformations for quantifying dfferent applied stress state, strain rate, and temperature effects on a porous powder metal steel (FC-0205)

Chapter IV discusses calibration and validation of a microstructure-based internal state variable (ISV) plasticity-damage model that was used to model the mechanical behavior of an FC-0205 steel powder. The model incorporates a new coalescence ISV equation to include the local stress interaction of the intervoid ligament distance between pores and is physically motivated by the highly porous powder metals.

Chapter V presents fatigue experiments for FC-0205 PM steel at high and low initial porosity levels. A microstructural analysis of the fatigue fracture surfaces allowed for calibration of a microstructurally-based fatigue model to be used next for validation of PM main bearing cap components.

Lastly, Chapter VI summarizes the results of the work performed in this research and also presents recommendations for future research.

CHAPTER II

ELASTIC MODULUS DEPENDENCE ON LARGE SCALE POROSITY

Using porous solids for a variety of engineering applications has led to the experimental and theoretical study of the effect of materials processed pores have on the elastic constants [Mackenzie (1950), McAdam (1950), Hill (1965), Budiansky (1965), Walpole (1969), Buch and Goldschimdt (1970), Lemaitre and Dufailly (1987), Spitzig, Smelser et al. (1988), Ramakrishnan and Arunachalam (1993), Chawla and Deng (2005), and Hardin and Beckermann (2007)].

Earlier work of the effective bulk and shear moduli calculations by Mackenzie (1950) was conducted when developing a theory for sintering. The pores were assumed to be homogeneous in size and spherical in shape and were embedded in a sphere of dense material. The calculation presented in the article was only valid when a linear relationship between stress and strain was present. The relationships derived for the shear and bulk moduli were

$$1 - \frac{G}{G_0} = \frac{5(3K_0+4G_0)}{9K_0+8G_0}\varphi + X\varphi^2 \tag{2.1}$$

$$\frac{1}{K} = \frac{1}{K_0(1-\varphi)} + \frac{3c}{4G_0(1-\varphi)} + X\varphi^3 \tag{2.2}$$

where G is the shear modulus, K is the bulk modulus, and the subscript 0 refers to the zero porosity (fully dense) material. The coefficient X was not determined by Mackenzie

resulting in his formulas being exact only when the porosity was much less than unity so the modulus is then linear with porosity.

Experimental work by McAdam (1950) on sintered ferrous alloys allowed for the elastic modulus to be determined from static bending tests. The elasticity of the alloys decreased with an increasing porosity where a more prominent decrease was observed when the porosity was higher than 20%. A theoretical expression for the effective elastic modulus relating to porosity was determined by curve fitting the experimental data giving the following expression

$$\frac{E}{E_0} = (1 - \varphi)^x \tag{2.3}$$

where E/E_0 is the ratio of the aggregate elastic modulus divided by the dense elastic modulus, and x is a material dependent constant.

An approach by Hashin (1962) and Hashin and Shtrikman (1963) consisted of finding upper and lower bounds for the elastic moduli. The bounds were determined by regarding the change in strain energy of a homogenous matrix caused by the addition of nonhomogeneities. The research concluded that for many practical applications accurate predictions of shear modulus bounds were determined except when the nonhomogeneities were pores or rigid inclusions.

Later independent work by both Hill (1965) and Budiansky (1965) developed a self-consistent theory that focused on a void imbedded in the matrix of a simple geometrical configuration with unknown effective moduli. An implicit equation of moduli is then obtained by determining the average stress and strain distributions in the matrix and void when there is an externally applied stress or strain.

Buch and Goldschimdt (1970) extended Hashin's model (1965) to examine the porosity effects on the elastic moduli for sintered metals. Experimental and theoretical results were compared for sintered iron, copper and tungsten. The authors assumed that the expression for the upper bound of the shear modulus developed by Hashin was equivalent to Young's modulus if the Poisson's ratio was constant over a certain range yielding the expression

$$\frac{E}{E_0} = 1 - \frac{15\,(1-\nu_0)\varphi}{7-5\nu_0+2(4-5\nu_0)\varphi} \tag{2.4}$$

where E is Young's modulus, ν is the Poisson's ratio, and the subscript 0 refers to the fully dense material. This simplified expression provided fairly accurate predictions when there was a constant sintering temperature and high relative density material.

An equation that incorporated a stress concentration factor was introduced by Bert (1985) that predicted normalized Young's modulus with porosity. The expression was introduced as

$$\frac{E}{E_0} = (1-\varphi)^{K_0 V_{max}} \tag{2.5}$$

where the normalized Young's modulus is E/E_0, the porosity is φ, K_0 is an isolated pore's stress concentration factor, and V_{max} is the maximum possible pore length for a nonequiaxed pore. Values of K_0 and V_{max} were given in tabular form for different pore geometries and loading directions. This expression was more accurate for spherical pores embedded in a matrix when the porosity value was less than 20%. As porosity was increased, Equation (2.5) predicted lower values than was experimentally determined.

Lemaitre and Dufailly (1987) combined the laws of elasticity and damage for the one dimensional case as,

$$\varepsilon_e = \frac{\sigma}{E_0(1-\varphi^{2/3})} = \frac{\sigma}{E} \tag{2.6}$$

where ε_e is the elastic strain, σ is the stress, E and E_0 are the damaged and undamaged moduli, respectively, Young's modulus. For pure ductile damage with no residual microstress,with φ being the porosity, which resulted in the modulus expressed in terms of porosity by

$$\frac{E}{E_0} = \left(1 - \varphi^{2/3}\right) \tag{2.7}$$

Experimental work by Spitzig, Smelser et al. (1988) on sintered iron compacts showed that the Young's and shear moduli compared well to the theoretical work by Hill (1965) and Budiansky (1965). Although a close correlation of the theoretical work to the data was observed, the data was linear because porosity levels up to 12% were tested. The researchers also noticed that the expression

$$\frac{E}{E_0} = \frac{G}{G_0} = (1 - 2\varphi) \tag{2.8}$$

accurately predicted the relationship of the experimental data. Where E and G are the Young's and shear moduli, respectively, and the subscript 0 refers to the pore free material.

Ramakrishnan and Arunachalam (1993) modified the work by Hashin and Shtrikman (1963) by using a spherical pore surrounded by a spherical matrix with an increasing pressure on the pore surface caused by the interaction of multiple pores in

relating the modulus to the porosity. The resulting expression for normalized Young's modulus was

$$\frac{E}{E_0} = \frac{(1-\varphi)^2}{1+(2-3\nu_0)\varphi} \tag{2.9}$$

where E is Young's modulus, the subscript 0 refers to the pore free material, and ν is the Poisson's ratio of the material. The theoretical results matched porous ceramics experimental data except for when the porosity level increased to 40%, and the Poisson's ratio was around 0.3.

Porous sintered steel experimental data for Young's modulus as a function of porosity was also compared to the theoretical equation of Ramakrishnan and Arunachalam (1993) by Chawla and Deng (2005). A close correlation was noted with a linear relationship to the maximum porosity of 10%.

A constitutive model developed by Bammann, Chiesa et al. (1993) for predicting failure in ductile materials uses the expression

$$\frac{E}{E_0} = (1 - \varphi) \tag{2.10}$$

to capture the effect that voids have on the degradation of the elastic moduli.

A study of porosity effects on the elastic response of cast steels was detailed by Hardin and Beckermann (2007). The empirical relationship for elastic modulus by Bert (1985) was compared to experimental data at varying porosities where the elastic modulus was found to decrease nonlinearly with increasing porosity. For cast steels Hardin and Beckermann (2007) found the following relationship,

$$\frac{E}{E_0} = \left(1 - \frac{\varphi}{0.5}\right)^{2.5} \tag{2.11}$$

Hardin and Beckermann (2007) also discovered that besides the amount of porosity, factors such as porosity distribution, pore shape, and pore size dictate the stiffness of porous materials.

A review by Haynes (1981) examined multiple theoretical analyses on the effect porosity has on the elastic response of sintered porous metals that had been presented up to the time of the publication. Steel experimental data from McAdam (1950) was plotted against theoretical results showing that Mackenzie (1950), Budiansky (1965), Hashin and Shtrikman (1963), Walpole (1969), and Yeh (1970) predicted linear and nonlinear modulus dependent porosity with higher Young's modulus values than experimentally determined when the porosity level was less than 20%. The best agreement between experimental and theoretical results was portrayed by Hashin and Shtrikman (1963) who captured satisfactorily the material response at low porosities. Hashin and Shtrikman (1963) attributed the lack of correlation to experimental data at higher porosity levels to irregular shaped and lower density necks between sintered particles that were assumed to have lower elastic modulus than the fully dense material. However, Haynes (1981) reported that no evidence has been provided that sintered necks are physically different than the bulk solid, and suggests that differences between experiments and theory are caused by the stress concentrations of voids.

A theoretical comparison to experimental data is shown in Figure 2.1. Pores were assumed spherical and randomly distributed in the matrix for the theories with the Young's modulus derived from the bulk and shear modulus when no expression for Young's modulus was supplied. Normalized Young's modulus experimental results

plotted are from compression, tension, and ultrasound experiments for FC-0205 powder metallurgy steel that have been detailed in earlier work (Allison, Grewal et al. (Under Review).

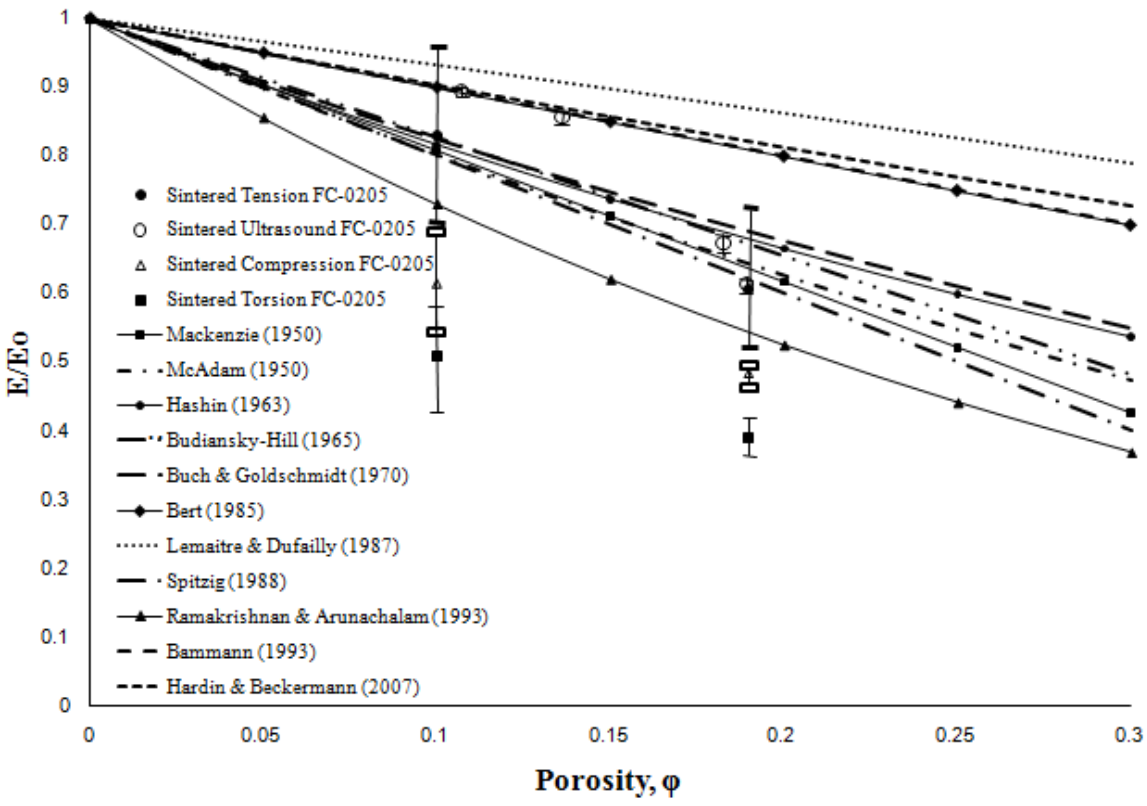

Figure 2.1 Young's modulus dependence on porosity comparison of FC-0205 experimental data to theoretical analyses.

The theoretical work compared to the experimental data is plotted in Figure 2.1 depicting the elastic modulus dependence related to porosity. When plotting the tensile elastic modulus as a function of porosity for FC-0205 steel, the models of Mackenzie, McAdam, Hashin, Budiansky, Hill, Buch, Spitzig, and Ramakrishnan all capture the

effect when considering the uncertainty within the experimental data. The lower bound predictions were from Ramakrishnan, while the upper bound predictions were from Lemaitre. Spitzig was not only able to capture the tensile data but also the ultrasound based data at 19% porosity. Bert and Bammann were able to predict the 10% porosity tensile data and the ultrasound based data at 12% and 14% porosities. However, the data at higher porosities was overestimated by Bert and Bammann. Hardin captured the 10% porosity tensile data and 12% porosity ultrasound based data, but at higher porosity levels the modulus was overpredicted. McAdam's equation was able to most accurately predict the experimental data by adjusting the material constant to capture the tensile data and the higher porosity ultrasound based data.

CHAPTER III

MICROSTRUCTURE-PROPERTY RELATIONS OF A POWDER METAL STEEL (FC-0205) UNDER VARYING TEMPERATURES, STRAIN RATES, AND STRESS STATES

Introduction

Powder metallurgy (PM) steel mechanical properties are very dependent on porosity and alloying additions. This section examines the influence of the porosity and alloying additions on mechanical behavior, and then concludes with an investigation of the current PM models.

For the case of monotonic tensile loading, strength, and ductility are decreased by porosity reducing the load bearing cross-sectional area, which becomes a stress concentration site for damage and localized strain Hadrboletz and Weiss (1997). Below 4% porosity, according to German (2005), most pores are isolated and closed, where pores are either isolated or interconnected between 5-15% porosity, and finally most pores are interconnected above 15% porosity. The interconnected porosity results in a strain localization increase at smaller sintered regions between particles, but the isolated porosity results in a deformation that is more homogenous.

The interconnected porosity is the most detrimental of the three cases causing a larger reduction in macroscopic ductility compared to isolated porosity Chawla and Deng

(2005). An inhomogeneous porosity distribution in a material is not uncommon to cause strain localization at pore clusters Chawla and Deng (2005).

Several studies have focused on tensile properties of iron-based materials at different porosities. O'Brien (1988), Dustoor, Taylor et al. (1989) and Stossel and Prucher (1993) tested iron-nickel and iron-copper materials reporting that ultimate tensile stress and yield stress increased with a decrease in porosity. However, the porosity type was not reported in the aforementioned work. Only a relationship of mechanical properties to porosity level was provided. Recent work by Kalashnikova, Gulyaev et al. (2004) examined the effect of 7-19% porosity on mechanical properties of Fe-4Ni-1.5Cu-0.5Mo sintered steel and determined that a decrease in porosity increased the monotonic mechanical properties of the steel. Pores were irregular in form and congregated at the periphery of the particles. Chawla and Deng (2005) provided monotonic analysis on Fe-Mo-Ni-C alloys at 3%, 5%, and 10% porosities. Decreasing the porosity increased the Young's modulus, proportional limit stress, tensile strength, and strain-to-failure for the material. Micrographs showed that at high porosities localized void growth was observed, while at lower porosities void growth and brittle cleavage fracture were observed.

To obtain higher performance in PM steels, alloying elements have been added to increase the strength of Fe. Copper is a common addition to iron, because it creates a transient liquid phase at sintering temperatures above the melting point of Cu. According to German (1996) Fe particles are wetted by the liquid Cu that brazes and bonds grains together. Cu will cause swelling of iron during sintering, but carbon is usually added to

control swelling. Copper provides precipitation strengthening while carbon provides strength to the iron by interstitial solid solution strengthening.

Research conducted by Klumpp, Eifler et al. (1992), Lowhaphandu and Lewandowski (1999), Saritas, Causton et al. (2005), Polasik, Willliams et al. (2002) demonstrated that the alloying addition of Cu increased tensile and fatigue strength. This work attributed strengthening to not only precipitation strengthening but to the development of secondary porosity in sintered materials. Primary porosity develops from the packing of particles and binder burnout, while secondary porosity develops as a result of liquid-phase formation and alloy diffusion leaving residual pores. Up to a critical size, smaller copper particles improved mechanical properties by leaving behind smaller residual pores.

Mechanical property experimental data ranging over varying temperatures has been published in the open literature for different powder metallurgy material by authors such as Firstov, Pechkovsky et al. (2006), Aly (2005), and Fedorchenko, Shevehuk et al. (1976). Compression data is more prevalent in the literature than tension and torsion.

Fedorchenko, Shevehuk et al. (1976) reported hardness, impact, transverse rupture, and compression results for sintered iron-base materials containing 6 and 9 wt. % calcium fluoride with porosity in the range of 28 – 30%. The test temperature ranged from ambient conditions up to 923 K. The transverse rupture and compression tests allowed Fedorchenko et al. (1976) to determine the temperature effects on ductile failure. Hardness values also displayed a decreasing Vickers hardness as the temperature

increased. Impact strength behavior was very dependent on the material without displaying a common observable trend.

Micro and macro indentor tests and uniaxial compression experiments were performed by Firstov, Pechkovsky et al. (2006) at temperatures varying from 293-1573 K. The materials investigated in his research were powder metallurgy titanium nanolaminates. When the test temperature increased, the compressive strength did not show a significant decrease when porosity in the sample was lower than 10% even though a minimal increase in plastic deformation before the fracture strain was observed. However, when porosity was greater than 20% a noticeable decrease in compressive strength and plastic deformation occurred with increasing temperature. Hardness values exhibited a trend of decreasing as temperature and porosity increased.

Sintered steel foams were compression tested at temperatures ranging from ambient to 873 K according to Aly (2005). The foams exhibited an increase in compressive strength up to a temperature of 723 K. As the temperature was further increased, a decreasing compressive strength was reported by the authors.

Stress state comparisons of PM tensile and torsion properties at ambient temperature has been reported by Yu and Prucher (1993) and Stossel and Prucher (1993) for Iron-Copper and Iron-Nickel systems. Mechanical testing of torsion and tensile specimens were reported by Stossel and Prucher (1993) while resonant frequency testing of the specimens was reported by Yu and Prucher (1993) and compared to the elastic properties from mechanical testing.

Shear yield for the PM materials was 0.56 times that of the tensile yield according to Stossel and Prucher (1993) and compared closely to the shear strength to tensile strength ratio of 0.6 for wrought steels reported by (2000). Tensile and shear strengths both exhibited a decrease as density was decreased. The resonant frequency determination of Young's modulus and shear modulus correlated as functions of density with different values for sponge iron and atomized iron powder. The resonant frequency values were also higher than the results obtained from mechanical testing. The Poisson's ratio did not appear to have a clear relationship to density although one might expect that since the Young's modulus showed a porosity dependence.

Material and Experimental Procedures

Water atomized iron powder, Atomet 1001, from Quebec Metal Powders (QMP) is the base iron powder for the FC-0205 material used in the study. The material code for FC-0205 steel grade is given by the Metals Powder Industries Federation (MPIF) Standard 35, "Materials Standards for PM Structural Parts" (2000). The nominal composition of the material is given in Table 3.1.

Table 3.1 Chemical Composition of FC-0205 Steel

MPIF Designation	Element			
	Fe	Cu	C	Acrawax C
FC-0205	97.1	2.00	0.5	0.4

Prefixes F and C in the designation represent the base material, iron, and the major alloying element, copper, respectively. The percentage of the major alloying element is given by the first two digits, 02, which indicate a 2% nominal copper addition within the range of 1.5% – 3.9%. The third and fourth digits provide information about the percentage of combined carbon, where 05 indicates a nominal value of 0.5% within a composition of 0.3% to 0.6% carbon. The base iron powder, Atomet 1001, chemical composition is provided in Table 3.2.

Table 3.2 Atomet 1001 Chemical Composition by Weight %.

Base Iron	Element							
Nomenclature	C	O	S	P	Mn	Cr	Cu	Ni
Atomet 1001	<0.01	<0.15	0.014	0.02	<0.22	0.09	0.04	0.10

A nominal composition of 2 wt% Cu, 0.5 wt% graphite, and balance iron was blended and binder treated were pressed and sintered into rectangular compacts with sintered densities of 6.35 g/cm^3 (we define these as "high porosity" for this study) and 7.05 g/cm^3 (we define this as "low porosity" for this study) via a proprietary process developed by Metaldyne (2007).

Because the internal state variable plasticity-damage model had not been used before for powder metals, the structure-property relations needed quantification. A series of compression, tension, and torsion experiments were conducted to quantify the microstructure-property correlations. Tension and compression tests were performed on standard ASTM specimens machined from the sintered blanks. ASTM E8 flat specimens

with a gage width of 6.35 mm and a gage thickness of 6.35 mm were used for tension testing (2004). Cylindrical compression specimens were machined with a diameter of 8.20 mm and a height of 9.84 mm. The torsion tests employed Lindholm type specimen design with an outside diameter of 19.05 mm, an inside diameter of 9.53 mm, and a gage length of 2.08 mm.

All tests were performed at a strain rate of 10^{-4}/sec and at one room temperature of 293 K. Additionally, tension and compression tests were also performed at a temperature of 593 K. High rate compression experiments were also performed on cylindrical specimens at 293 K to capture strain rate effects. All tests were performed on specimens machined from rectangular blanks compacted and sintered by Metaldyne, LLC at a sintered density of 6.35 g/cm3 and 7.05 g/cm3.

Tension and compression experiments were performed on an Instron 5882 testing machine, with a +100 kN maximum loading capacity. An Instron 3119-407 add-on cooling/heating environmental chamber allowed for the Instron 5882 to perform tests at a temperature range of 123K to 623K. Monitoring and controlling the strain rate during the tension tests was done by a water-cooled Instron 2630-052 extensometer. The extensometer had a 2.54 cm gage length with the capability of accurately measuring strains up to a temperature of 773K. However, due to the size of compression specimens, the strain rate was controlled by the displacement of the crosshead. High temperature strain gages (model CEA-06-032UW-120 by Vishay) were used for measuring the strain. Strain data acquisition was obtained by using a PC and DAQ system using LabVIEW version 7.1.

Torsion testing was conducted on an Instron model 8850 bi-axial load frame with a maximum axial load of +1MN and a torsional capacity of +10kN-m. As with the compression tests, strain rates for the torsion tests were controlled by monitoring the rotation of the load cell. Due to the large size of the machine with respect to size and load applied to the specimen, no compliance correction factor was used.

The high strain rate compression tests were conducted using a split Hopkinson pressure bar (Kolsky) apparatus with striker, incident, and transmitted bars all consisting of maraging steel 12.5 mm in diameter. The tests specimen is loaded by a stress wave propagated by the striker bar impacting the incident bar. Once the wave reaches the specimen, a portion of the wave is reflected back through the incident bar, and the rest is passed through to the transmitted bar. Since the incident and reflected bars remain elastic during the testing, they act as force and displacement transducers during the test. The high strain rate compression data was analyzed using the DAVID software package Gary (2005), which compensates for the inherent dispersion of the wave and the calculation of the force and velocities at both faces of the specimen during the test to verify force equilibrium. All strain rates were calculated as the best linear correlation of a strain versus time plot from a strain level of 0.02 to the end of the data. The strain rate was then rounded to the nearest 100/s. Microstructural quantifications of porosity and grain size was performed on the initial porosity states of high and low porosity specimens as detailed in a companion article currently under review by Stone, Tucker et al. (2009).

Results and Discussion

Porosity measurements resulting from Archimedes' oil-intrusion method of sintered densities and image analysis are provided in Table 3.3.

Table 3.3 Sintered density and porosity in FC-0205.

Sintered density (g/cm3)	Porosity from sintered density (%)	Porosity from image analysis (%)
6.35	18.6 + 0.0007	18.8 + 0.0046
7.05	9.6 + 0.00190	9.3 + 0.0006

The porosity values determined from image analysis were 18.8% for 6.35 g/cm3 and 9.3% for 7.05 g/cm3. (For communication purposes, we designate "low porosity" for the 9% case and "high porosity" for the 19% case.) A measurement of the porosity determined from the sintered density is comparable the image analysis porosity values. From the image analysis, pore characteristics were determined for pore diameter and the pore nearest neighbor distance as displayed in Table 3.4.

Table 3.4 Average pore characteristics from image analysis of the FC-0205 alloys with standard deviations.

Sintered density (g/cm3)	Average pore diameter (microns)	Maximum pore diameter (microns)	Average pore nearest neighbor distance (microns)	Maximum pore nearest neighbor distance (microns)
6.35	6.6 + 1.4	160.1 + 23.5	9.8 + 0.9	59.1 + 7.9
7.05	6.5 + 0.7	99.4 + 19.8	10.5 + 0.3	50.4 + 6.7

An increase in alloy density exhibited a decrease in pore size and an increase in the distance between pores (nearest neighbor distance) according to Table 3.4. Grain size

measurements for the two alloys show no distinguishable difference between the grain sizes due to the uncertainty band of the results in Table 3.5.

Table 3.5 ASTM Grain size measurements for FC-0205 alloys.

Sintered density	Grain size (microns)
6.35	11.62 + 0.57
7.05	11.54 + 0.64

Optical micrographs of the two densities depict microstructures with different pore morphologies, pore size, and pore distribution as shown in Figure 3.1.

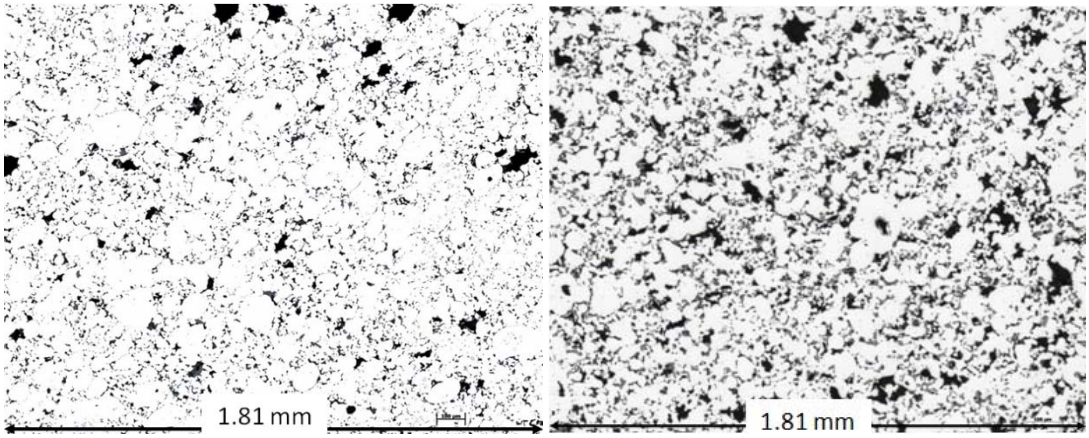

(a) (b)

Figure 3.1 Microstructure of FC-0205 steel at densities of (a) 7.05 g/cm3 (initial porosity level = 9%) and (b) 6.35 g/cm3 (initial porosity level = 19%).

Specifically, an increase in the irregular shape of pores appears for the low density material while the high density material has smaller pores. SEM was used to reveal the pearlite in the steel observed in Figure 3.2.

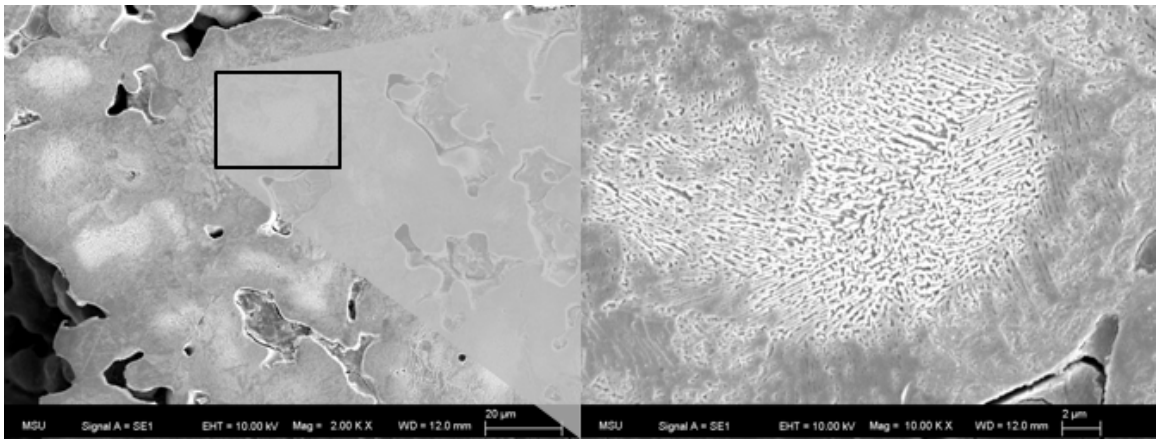

Figure 3.2 Pearlite shown in the microstructure of FC-0205 using SEM.

Experimental mean tension test results with their associated error bands of high and low porosity specimens are compared at a temperature of 293K and 573K in Figure 3.3. The number of data points represented three tests where fracture occurred in the gage section.

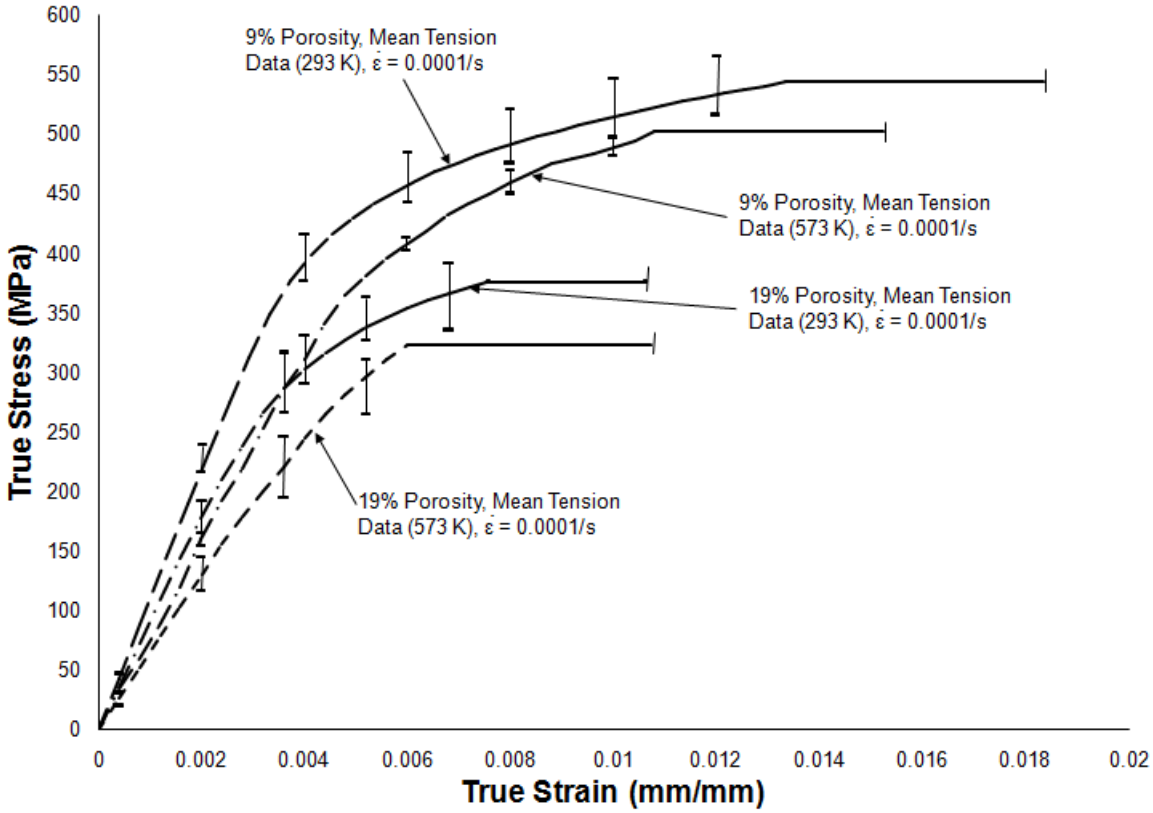

Figure 3.3 True stress-strain behavior with different porosities (9% and 19% initial porosity levels) under tension at 293 K and 573 K. For the low porosity tested at 573 K, only one test was performed. Note that the error bars illustrate not only the uncertainty in the work hardening but the failure strains as well.

Figure 3.3 displays a porosity dependence on the elastic modulus and work hardening rate. As the initial porosity level increased, the elastic modulus and work hardening rate decreased. The elongation to failure decreased as the initial porosity level increased. Also, there is no clear temperature dependence on the elongation to failure as well. However, we see a clear lower work hardening rate as the temperature increased. An increasing temperature degraded the elastic modulus as observed for both the low and

high porosity tensile data. Similarly, as the temperature increased, the ultimate tensile strength decreased more for the low porosity specimens when compared to the high porosity specimens. More scatter in the high porosity data makes the ultimate tensile strength degradation not as clear as the low porosity data but the trends are qualitatively clear.

Fracture surfaces of the specimens associated with the ambient stress-strain data in Figure 3.3 are shown in Figure 3.4. The fracture surfaces were imaged using a SUPRA 40 field emission gun scanning electron microscope (FEG-SEM) from Carl Zeiss SUPRA.

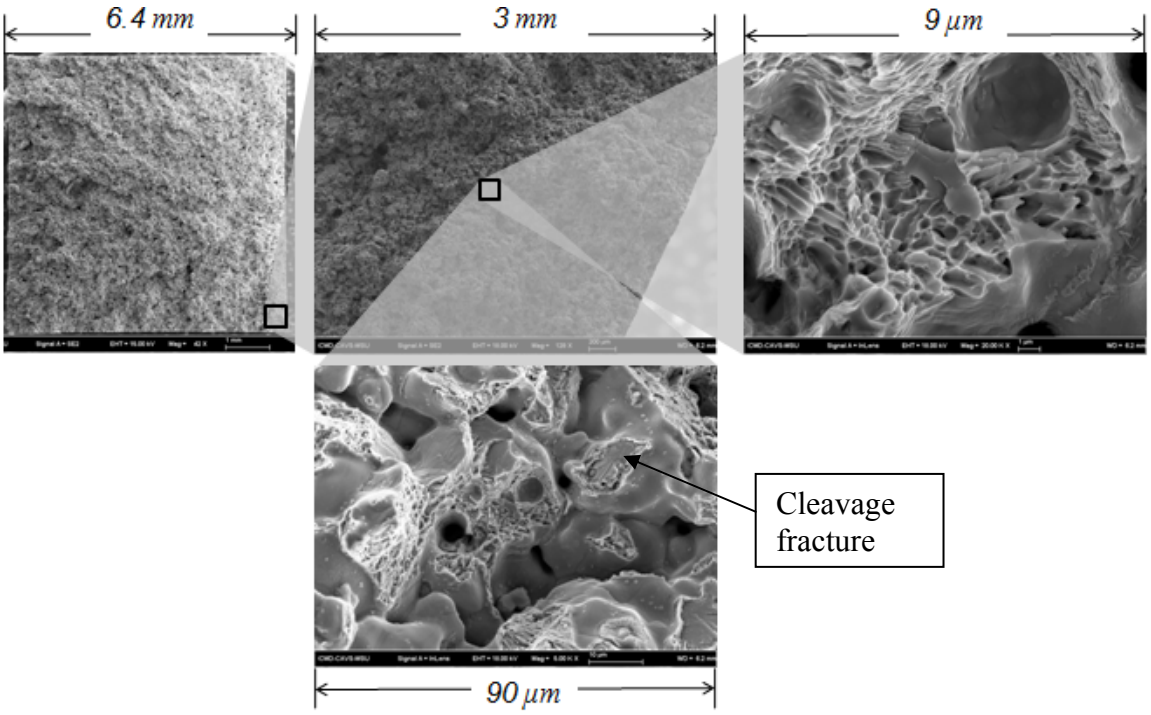

(a)

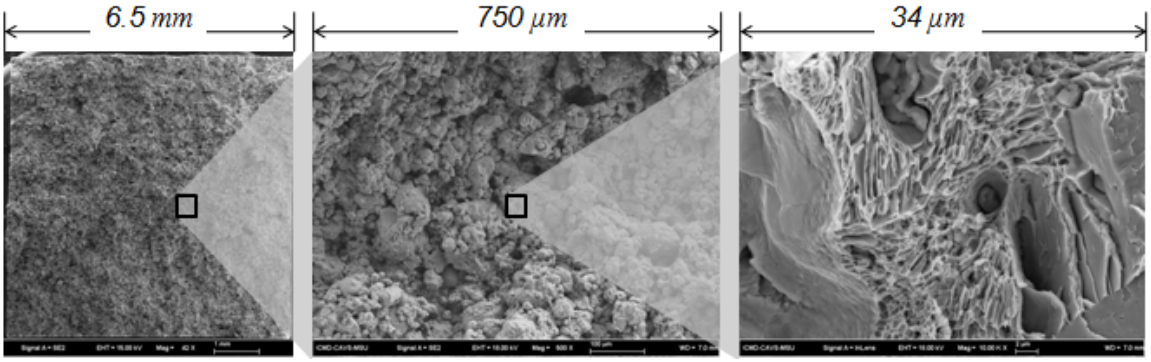

(b)

Figure 3.4 Fracture surfaces of (a) low porosity (9%) and (b) high porosity (19%) tensile specimens tested at 293K.

The low porosity micrographs of Figure 3.4a exhibits cleavage fracture and microvoids as was indicative of the fracture surface of all the tensile specimens. The high porosity fracture surface of Figure 3.4b depicts the microvoids and dimples seen also with the low porosity specimen.

Tension tests at 573K display fracture surfaces in Figure 3.5 that are similar to those observed for tests at 293K. Pores are visible in the macroscopic micrographs on the left side of the figure while zoomed-in images on the right side of the figure displays dimples, microvoids, and cleaved surfaces.

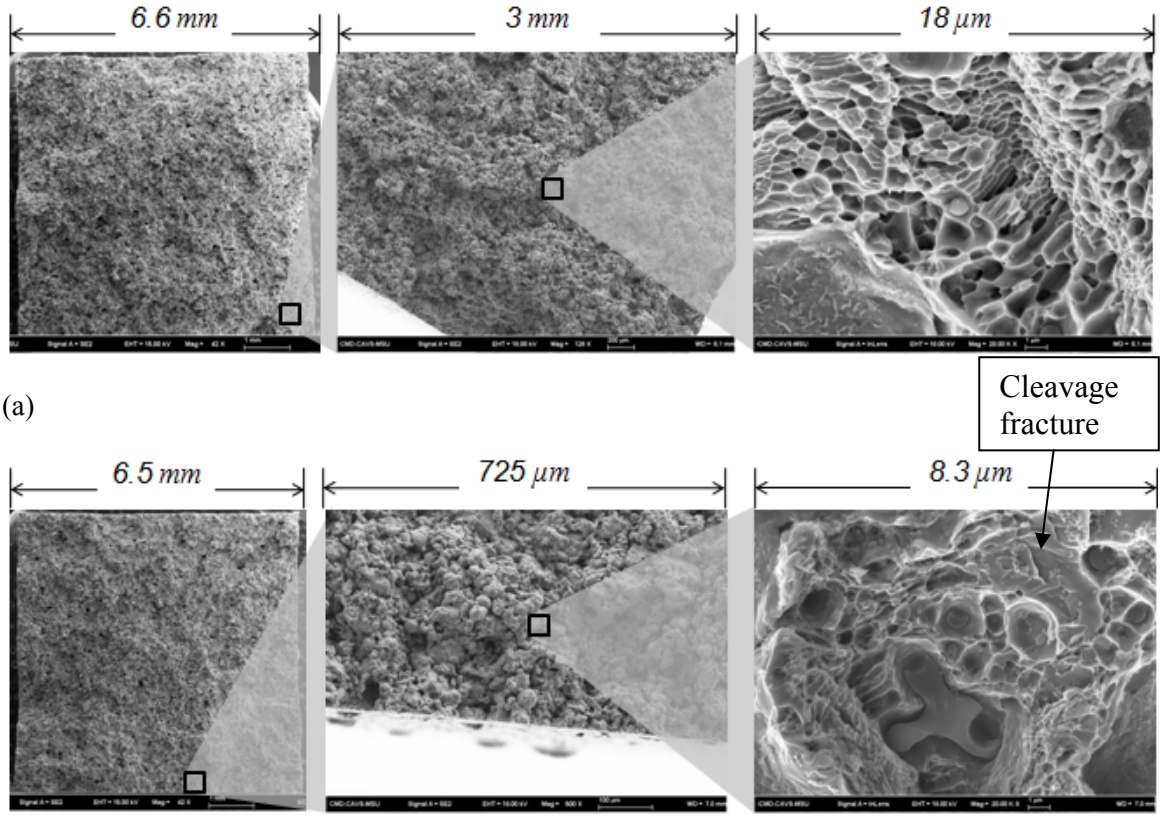

Figure 3.5. Fracture surfaces of (a) low porosity (9%) and (b) high porosity (19%) tensile specimens tested at a temperature of 573K.

The cleaved fracture point is illustrated in Figure 3.5a. Although cleaved surfaces were present, they were not as abundant on the fracture surfaces of the tension specimens as the microvoids and dimples.

The microstructure quantification of the tensile fracture surfaces are provided for the macrovoids and microvoids in Table 3.6 and Table 3.7, respectively.

Table 3.6 Macrovoid tensile fracture surface characteristics.

Initial Porosity Level	Temperature (K)	Volume Fraction Macro-voids	Average NND (μm)	Maximum NND (μm)	Average Pore Diameter (μm)	Maximum Pore Diameter (μm)
Low	293	0.73	10.63	84.25	32.03	368.64
High	293	0.92	5.55	15.05	27.44	109.42
Low	573	0.81	21.97	91.31	34.71	155.00
High	573	0.91	10.54	44.19	11.48	126.95

Table 3.7 Microvoid tensile fracture surface characteristics.

Initial Porosity Level	Temperature (K)	Volume Fraction Micro-voids	Average NND (μm)	Maximum NND (μm)	Average Pore Diameter (μm)	Maximum Pore Diameter (μm)	Inter-void Ligament Distance (μm)
Low	293	0.79	0.23	1.10	0.16	4.60	0.07
High	293	0.86	0.83	2.59	0.58	9.41	0.25
Low	573	0.80	1.55	2.39	1.48	5.53	0.08
High	573	0.82	0.30	1.57	0.20	8.33	0.10

A lower volume fraction for the low initial porosity specimens is shown in Tables 3.6 and 3.7. The average nearest neighbor distance (NND), the distance between the center of two pores, and average pore diameter is lower for the specimens with the higher initial porosity at the macrovoid scale for the respective temperatures, while the microvoid scale does not exhibit any clear trends. Macrovoid quantification of the maximum NND at the macroscale displays a greater value for the low initial porosity specimens, while the no specific trend is observed at the microscale. The larger average pore diameter at the macroscale is observed for the low initial porosity specimens while

the trend is not as distinguishable at the microscale. Fracture surfaces of the macrovoid showed the low initial porosity specimens containing the larger maximum pore diameters while the opposite was seen at the microvoid level. The microvoid fracture surfaces had the intervoid ligament distance (IVL), distance between the closest edge of two neighboring pores, where the higher initial porosity specimens contained a larger IVL at both temperatures.

Mean compression results at high and low porosity are shown in Figures 3.6 for testing at 293 K and 573 K.

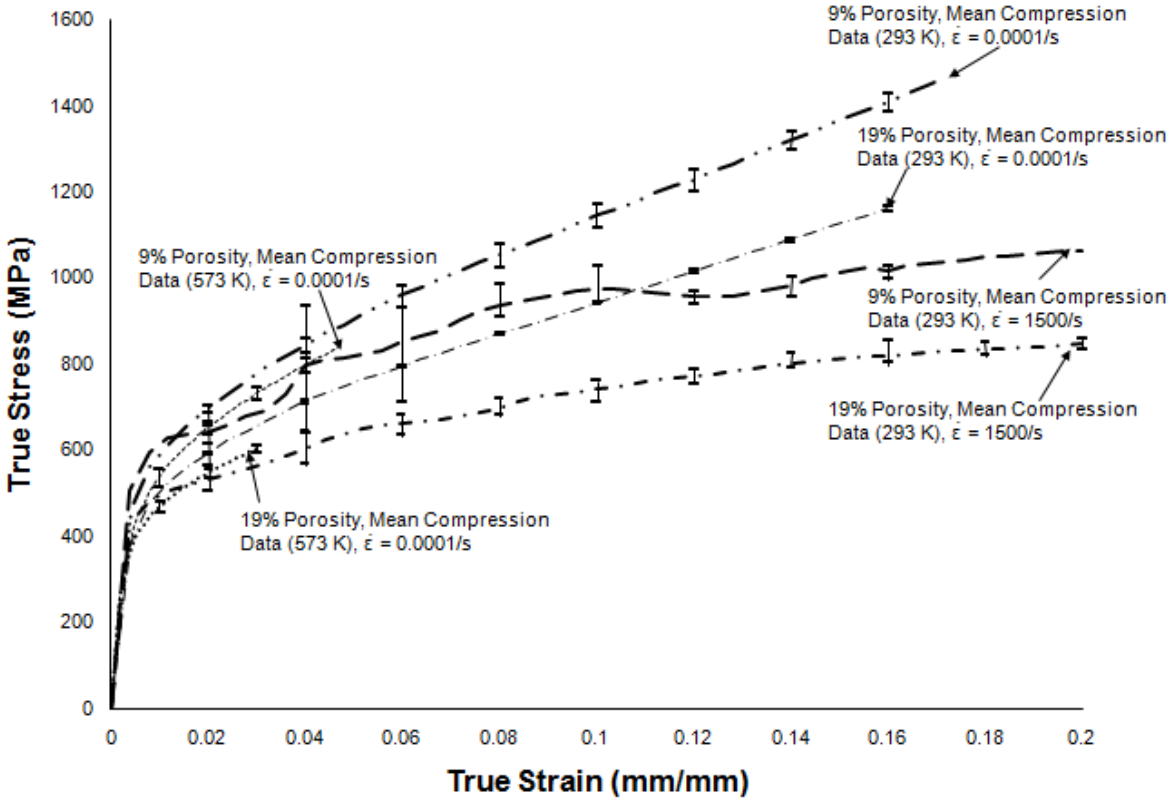

Figure 3.6 True stress-strain compression behavior with different porosities (9% and 19% porosity levels), temperatures (293K and 573K), and strain rates (quasi-static (0.0001/s) and high rate (1500/s).

The compression experiment results are not reported to fracture in Figure 3.5, but only report data recorded until testing was stopped due to machine loading capacity. As porosity level increased no distinct dependence on the elastic modulus could be determined even though a dependence on work hardening rate is observed. The work hardening rate decreased as the porosity level increased. No concise temperature affect on work hardening rate or elastic modulus is displayed; however the yield stress is decreased for both porosity levels as the temperature is increased. Strain rate decreased the yield stress at lower strain rates, while the work hardening rate considerably increased.

Similar mechanical property attributes for the torsion results are observed as the compression and tension experimental results as shown in Figure 3.7. The effective true stress and effective true strain are plotted for low and high porosity torsion experiments at 293K.

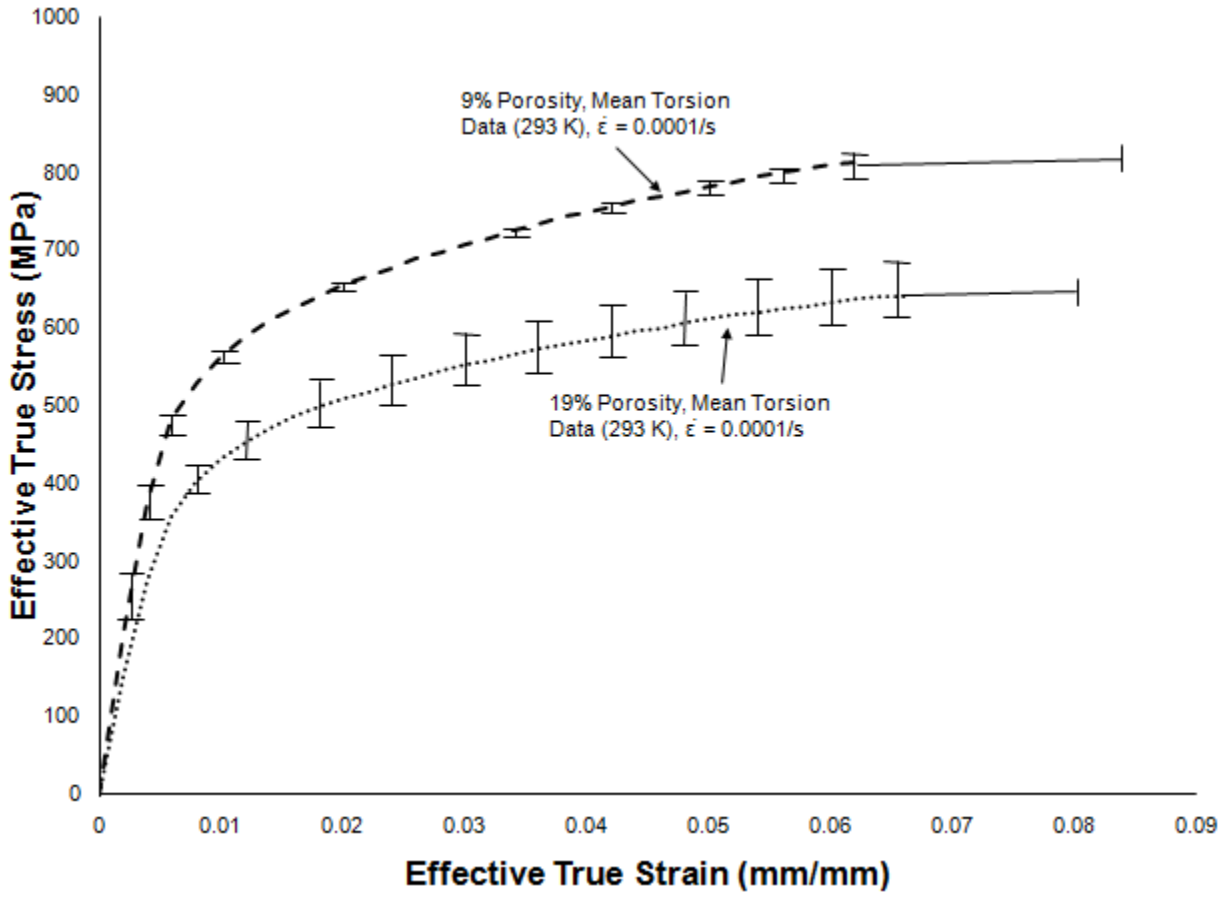

Figure 3.7 High and low porosity torsion effective stress-strain curves with different initial porosity levels (9% and 19%) at 293K.

Increase in the initial porosity level resulted in decreased elastic modulus and work hardening rate in Figure 3.7. The low porosity specimens displayed a lower yield strength when compared with the high porosity specimens. However, the porosity affect on elongation to failure is not concise due to the scatter in the experimental data. Fracture surfaces of the Lindholm torsion specimens also depict the porosity in the material as observed in Figure 3.8.

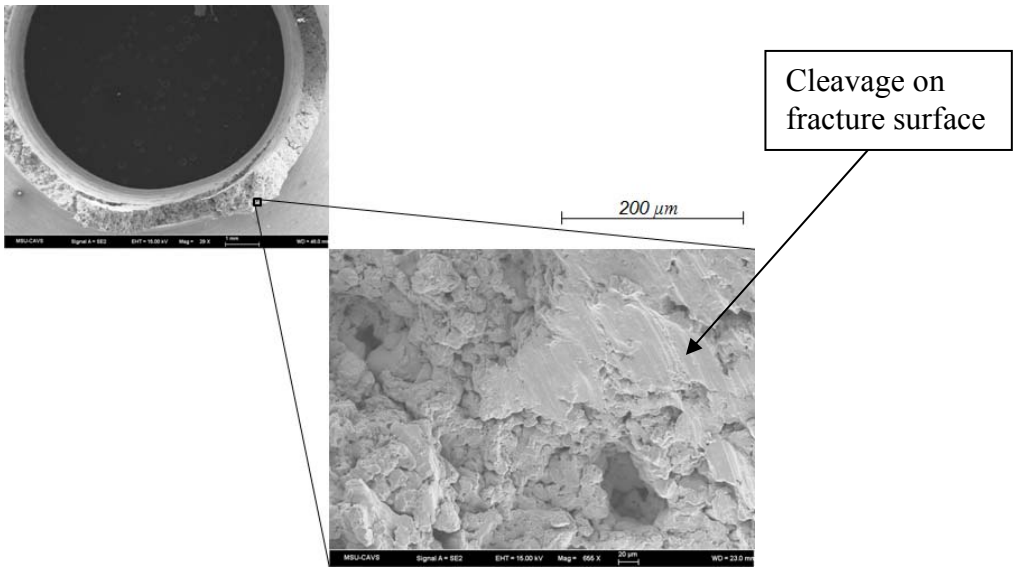

(a)

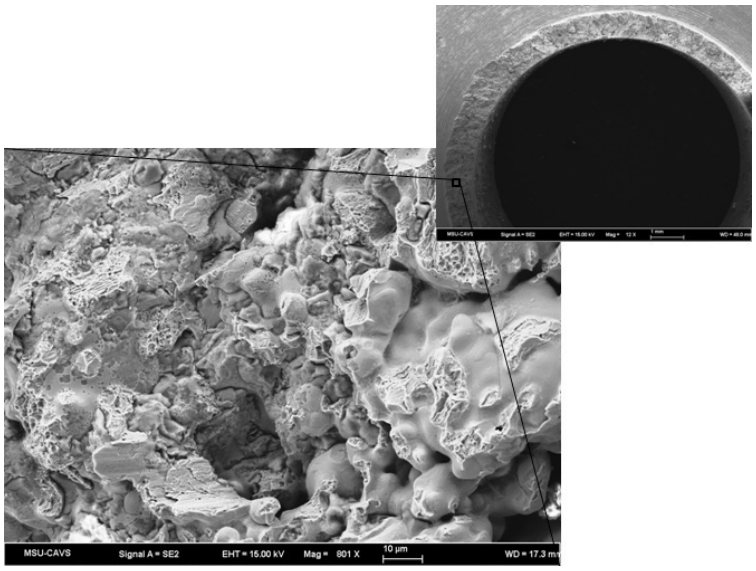

(b)

Figure 3.8 Lindholm torsion specimen fracture surfaces of (a) low porosity (9%) and (b) high porosity (19%) specimens.

Microvoids and dimples are observable on the torsion fracture surfaces. Cleaved areas are depicted by the arrow in Figure 3.8a. A comparison of the compression, tension, and torsion data up to a strain of 0.02 mm/mm is given in Figure 3.9.

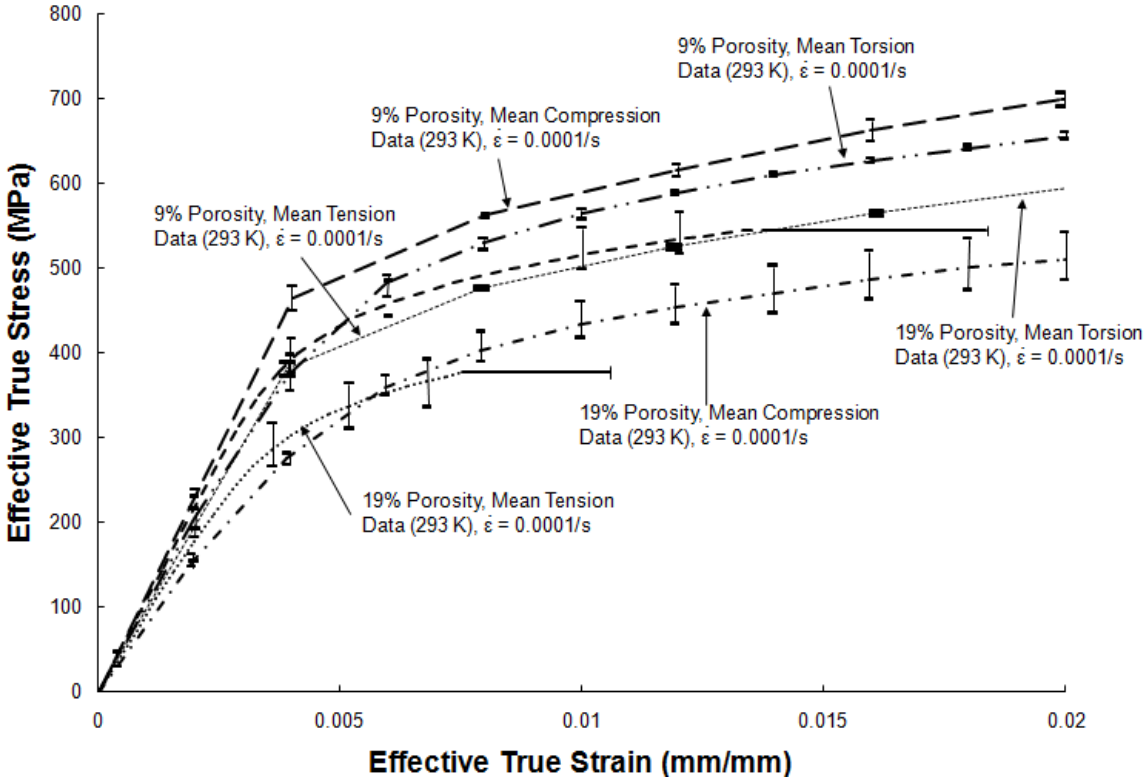

Figure 3.9 Comparison of low porosity (9%) and high porosity (19%) tension, torsion, and compression experiments performed at ambient temperature.

For both initial porosity levels in Figure 3.9, the tension data exhibited the highest elastic modulus, while the torsion data displayed the lowest elastic modulus. Work hardening rate was a maximum for the compression results and a minimum for the tension results for both porosity levels. Only the tension and torsion experiments were tested to failure, and the tension data exhibited a much lower failure strain than the

torsion data for both porosities. Evidently, compression data was not tested to failure but still exhibits the largest ultimate strength for both porosity levels tested while tension data showed the lowest ultimate tensile strength.

Ambient tension and torsion data available in the open literature for FC-0208 PM steel was compared with the FC-0205 PM steel results from this study.

FC-0208 and FC-0205 contain similar amounts of copper (1.5 – 3.9 wt%), whereas the difference is that FC-0205 contains between 0.3-0.6 wt% carbon and FC-0208 has carbon levels from 0.6-0.9 wt%. Average elongation to failure for published data are plotted with the experimental results from this study in Figure 3.10.

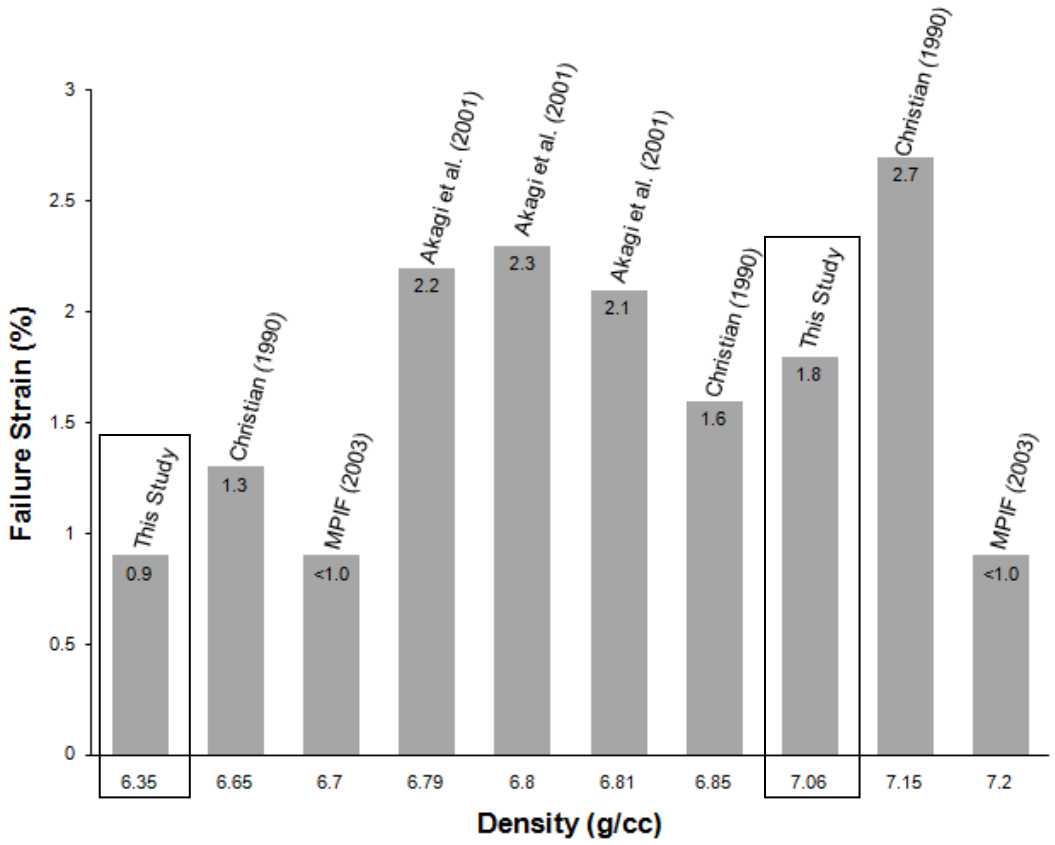

Figure 3.10 Comparison of failure strain for published FC-0208 data and FC-0205 experimental results from this study.

The trend in Figure 3.10 shows the elongation to failure of this study increasing as the sintered density was increased as Christian (1990) noted with his data.

Figures 3.11 and 3.12 compare the published FC-0208 ultimate tensile strength and 0.2% yield strength results, respectively, to the FC-0205 results of this study.

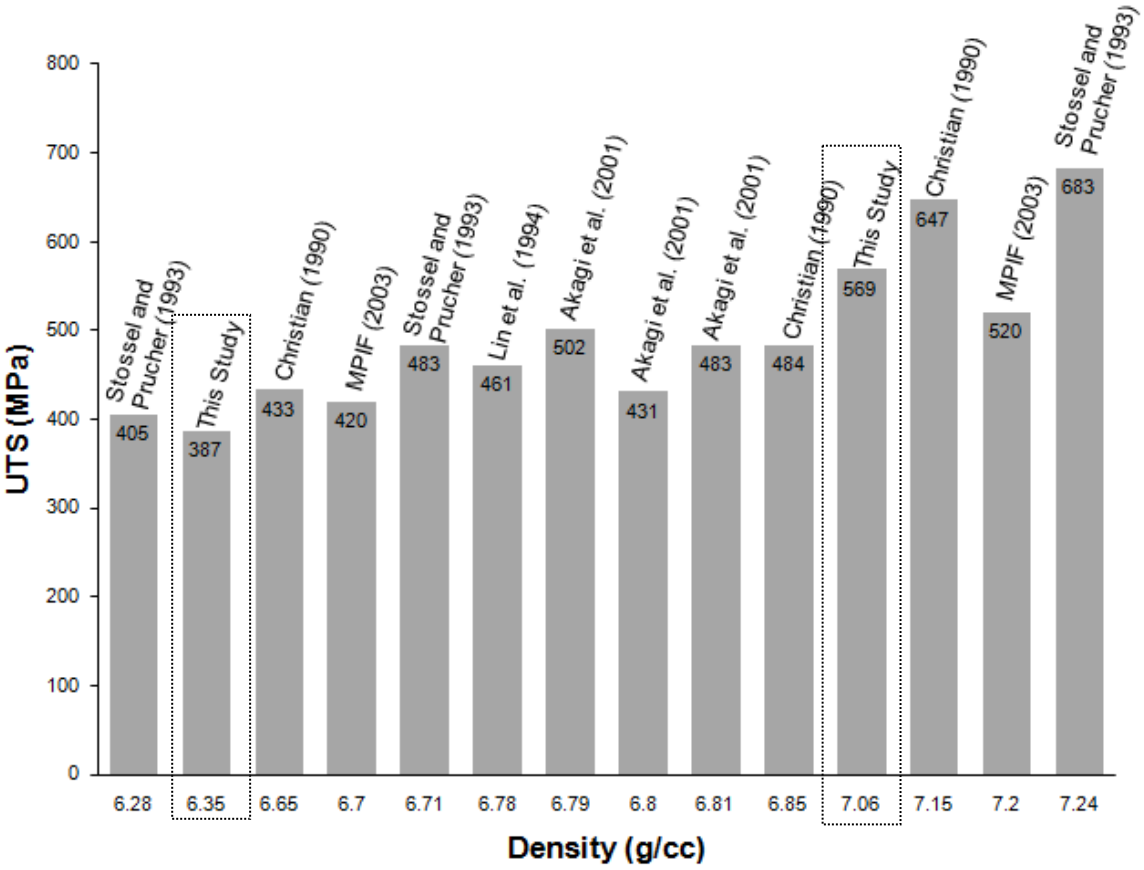

Figure 3.11 Comparison of UTS for published FC-0208 data to the FC-0205 experimental results from this study.

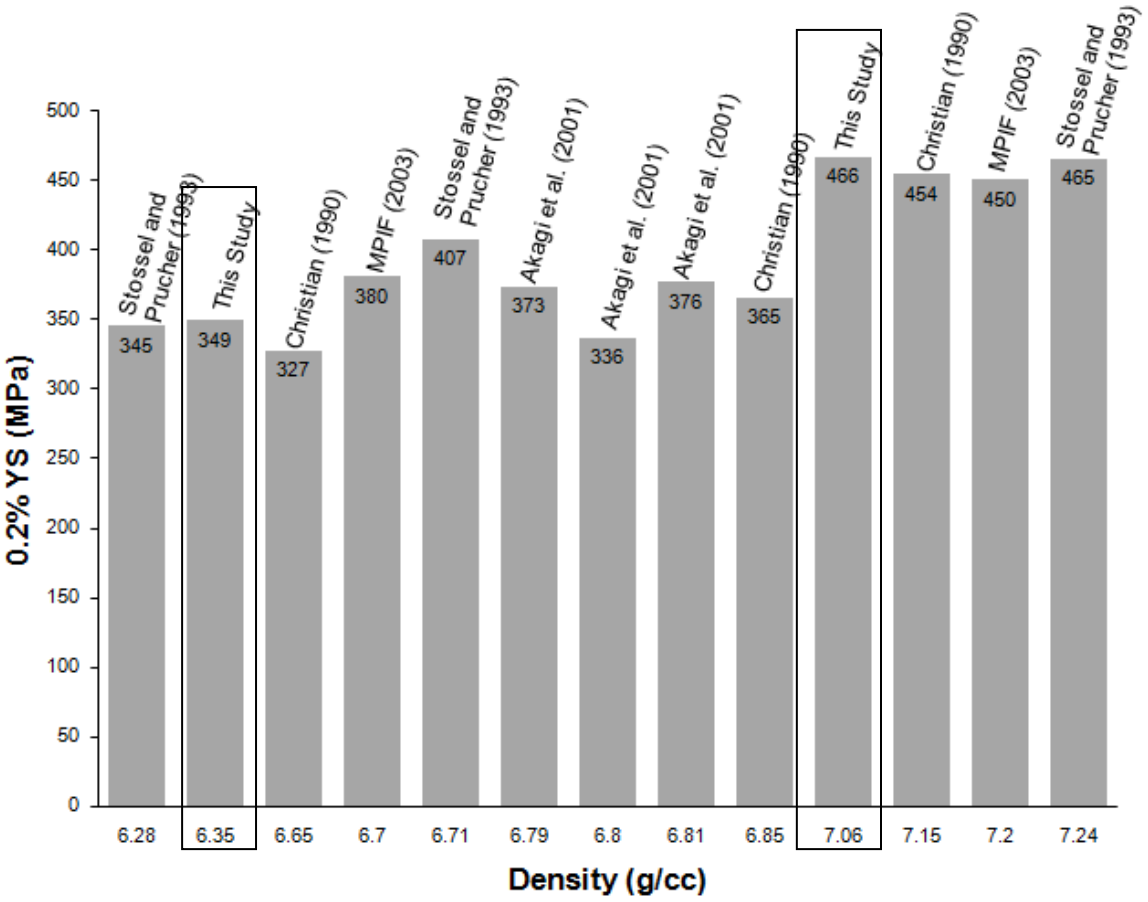

Figure 3.12 Comparison of 0.2% offset YS for published FC-0208 data to the FC-0205 experimental results from this study.

The UTS graphed in Figure 3.11 exhibited qualitatively a trend of increasing strength with increasing density significantly more than the 0.2% YS data plotted in Figure 3.12. Below the density of 7.06 g/cc, Figure 3.12 does not qualitatively depict a crisp relationship between density and 0.2% YS.

Comparison of published data to results from this study for shear rupture strength and shear yield strength plotted against density are graphed in Figures 3.13 and 3.14,

respectively. The determination of shear yield strength was provided by Stossel and Prucher (1993).

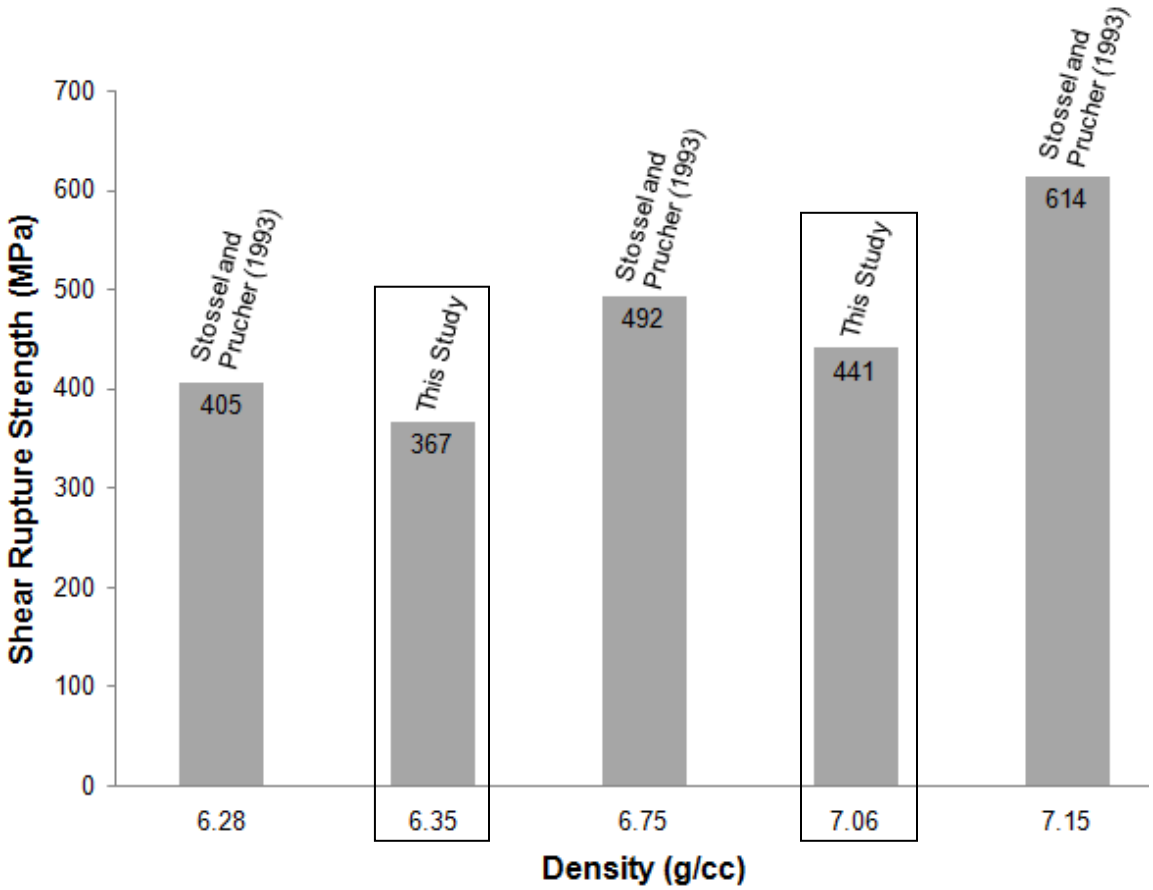

Figure 3.13 Comparison of shear rupture strength for published FC-0208 data to the FC-0205 experimental results from this study.

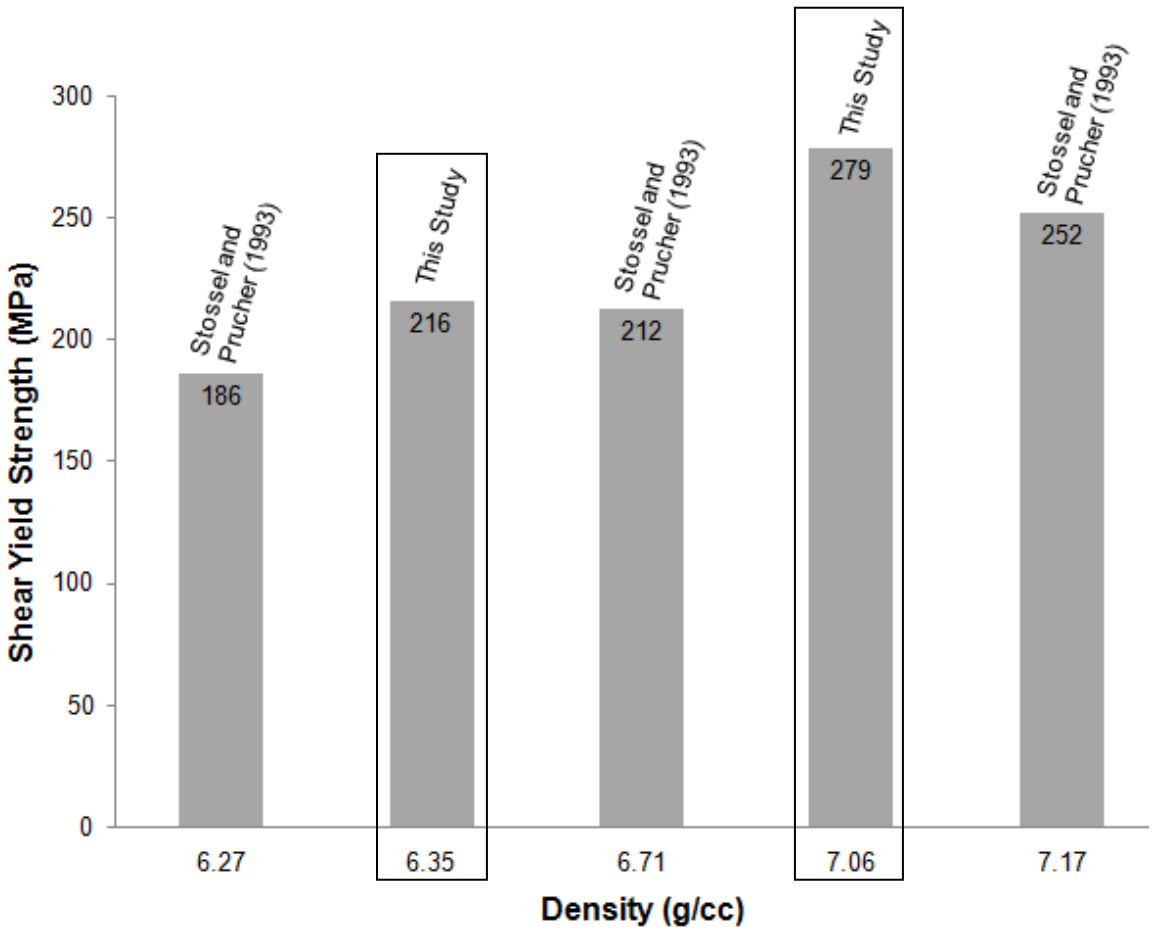

Figure 3.14 Comparison of shear yield strength for published FC-0208 data to the FC-0205 experimental results from this study.

Both Figures 3.13 and 3.14 display an increasing strength with increasing density for the specific material designation. However, the shear rupture data comparison resulted in higher values for FC-0208 while the shear yield strength comparison displayed higher values for the FC-0205 material.

Conclusions

The experimental parameters that varied included different porosity levels, different applied stress states (tension, compression, and torsion), and different temperatures. Some of the experimental observations include the following:

1. greater elongations-to-failure with a lower initial porosity level,
2. higher work hardening for compression followed by tension followed by torsion,
3. typical work softening at higher temperatures,
4. typical higher flow stresses for higher applied strain rates, and

   a reduced failure strain for tension when compared to torsion or compression.

CHAPTER IV

INTERNAL STATE VARIABLE MODELING OF PLASTICITY AND FRACTURE OF A STEEL POWDER METAL UNDER VARIOUS STRAIN RATES, TEMPERATURES, AND STRESS STATES

Introduction

Computational and mathematical based modeling of the thermomechanical behavior for powder metallurgy component design and performance prediction are recognized as significant contributions to improving efficiency, quality and cost of current production and generating new business opportunities for the automotive industry. PM techniques are being incorporated to manufacture various complex shaped engineering components, which prove difficult to cast or shape by alternative procedures. A motivating factor driving the development of a mathematical based model is the ability to accurately predict the variation in property performance caused by inhomogeneous density distribution. Research addressing mathematical modeling will provide several benefits including: near net shape components, complex geometries, high strength and minimal or eliminated finishing operations Hammi, Stone et al. (2006).

In this chapter, we address stress-state dependence and associated material modeling to capture the effects. Typical finite element analysis employs a von Mises criterion that essentially makes equivalent any stress state. However, the experimental results in this

paper clearly indicate that a von Mises criterion would be a gross approximation. Furthermore, a material model is presented that captures the differing stress state, strain rate, and temperature effects. A physics-based model that includes microstructure-based internal state variables for plasticity and damage based upon the Bammann (1984), Bammann and Aifantis (1989), Bammann Bammann (1990), Bammann, Chiesa et al. (1993), and Bammann, Chiesa et al. (1997), and later improved by Horstemeyer and Gokhale (1999) and Horstemeyer, Lathrop et al. (2000) by including void nucleation, void growth, and void coalescence evolution equations is used to correlate to the experimental data. The McClintock (1968) void growth rule is used for voids growing from particles, while the Cocks and Ashby (1982) void growth rule is applied for pre-existing voids growing. This model is capable of predicting stress-strain and ductile fracture behavior under various strain rate, temperature, and stress-state conditions.

Microstructure-based ISV Plasticity-damage Model

A physically-based model including microstructure-based internal state variables including plasticity and damage is based on the Bammann (1984), Bammann and Aifantis (1989), Bammann (1990), Bammann, Chiesa et al. (1993), and Bammann, Chiesa et al. (1997) with the addition of void nucleation, void growth, and void coalescence evolution equations by Horstemeyer and Gokhale (1999) and Horstemeyer, Lathrop et al. (2000). The McClintock void growth rule is incorporated for voids growing from particles

McClintock (1968), while the Cocks and Ashby (1982) void growth rule is used for pre-existing void growth.

The assumption of multiplicative decomposition of the deformation gradient into elastic and plastic parts is made. The deformation gradient, F, connects a point in the reference (non-deformed) configuration to the same point in the current (deformed) configuration. Work by Kroner (1960) showed that the decomposition of the deformation gradient, F, into elastic, Fe, and plastic, Fp, parts as

$$\underline{F} = \underline{F^e}\,\underline{F^p} \tag{4.1}$$

Here the elastic deformation gradient, Fe, represents the reversible elastic stretching and rotation of the crystal lattice in the current (deformed) configuration. The plastic deformation gradient, Fp, describes the irreversible plastic deformation due to crystallographic slip. Further multiplicative decomposition has been done Bammann and Aifantis (1989) on work by Lee (1969). Here the plastic deformation gradient splits into an isochoric inelastic, Fdp, and volumetric inelastic, Fvp, parts. The multiplicative decomposition of the deformation gradient is now

$$\underline{F} = \underline{F^e}\,\underline{F_d^p}\,\underline{F_v^p} \tag{4.2}$$

which is shown graphically in Figure 4.1.

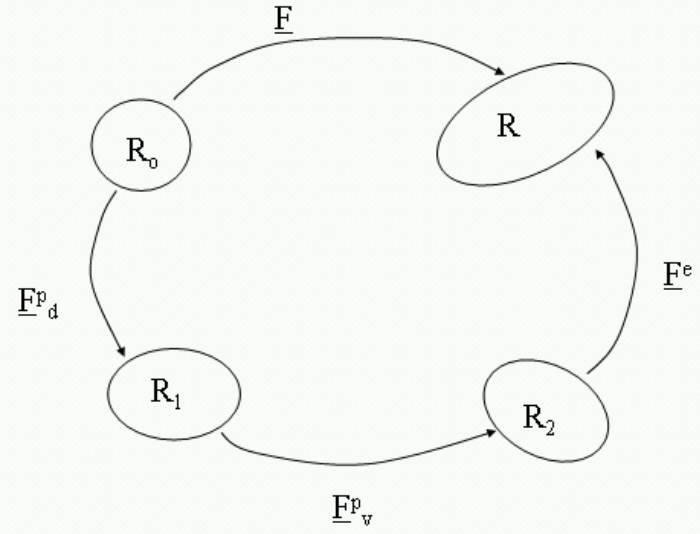

Figure 4.1 Schematic illustration of the multiplicative decomposition of the deformation gradient.The Jacobian of Equation (2.2.2) characterizes the change in volume or change in density due to voids nucleating and growing for a constant mass.

$$J = \det(\underline{F_v^p}) = \frac{V_2}{V_0} = \frac{\rho_0}{\rho_2} \tag{4.3}$$

Assuming that the volume in State 0 and State 1 are equal due to inelastic incompressibility, then the change in volume from State 0 (reference configuration) to State 2 (intermediate configuration) is,

$$V_2 = V_0 + V_v \tag{4.4}$$

where V2 and ρ2 are the volume and density in State 2, respectively. Then V0 and ρ0 are the volume and density in State 0, respectively. The term Vv is a new term added from the volume of the voids.

From Equation (4.3), damage, φ, is defined as the ratio of volume in elastically unloaded State 2 from the reference volume, State 0, to the volume in State 2.

$$\varphi = \frac{V_2 - V_0}{V_2} = \frac{V_v}{V_2} \tag{4.5}$$

The evolution of damage given by Horstemeyer (2001) is,

$$\varphi = \left(\eta \nu + \varphi_{pore}\right)c \tag{4.6}$$

where c is a coalescence term, η is a void nucleation term, ν is a void growth term, and φpore is the damage originating from pre-existing pores.

The nucleation term, η, is the number of voids per unit volume with Horstemeyer (2001) expressing the term in rate form as

$$\dot{\eta} = \left\|D_d^p\right\|\left(\frac{d^{0.5}}{K_{IC} f^{1/3}}\eta\left\{a\left[\frac{4}{27} - \frac{J_3^2}{J_2^3}\right] + b\frac{J_3}{J_2^{3/2}} + c\left\|\frac{I_1}{\sqrt{J_2}}\right\|\right\}\right)\exp\frac{C_{T\eta}}{T} \tag{4.7}$$

where Ddp is the deviatoric plastic rate of deformation, d is the average inclusion particle size, KIC is the fracture toughness, f is the initial void volume fraction, a, b, c and CTη are material constants, J2 and J3 are the second and third deviatoric stress invariants, I1 is the first invariant of stress.

The void growth equation currently used is from McClintock (1968)

$$\nu = \frac{4}{3}\left[R_0 \exp\left(\varepsilon(t)\frac{\sqrt{3}}{2(1-n)}\right)\sinh\left(\sqrt{3}(1-n)\frac{\sqrt{2}I_1}{3\sqrt{J_2}}\right)\right]^3 \tag{4.8}$$

where R0 is the initial void radius, ε(t) is the strain obtained from time (t), and n is the strain-hardening exponent.

The damage originating from the initial pores in the material is from Cocks and Ashby (1982)

$$\dot{\varphi}_{pores} = \left[\frac{1}{(1-\varphi_{pores})^{V(T)/Y(T)}} - (1-\varphi_{pores}) \right] \sinh\left\{ \frac{2(2m-1)}{2m+1} \frac{\sigma_h}{\sigma_e} \right\} \left\| D_d^p \right\| \tag{4.9}$$

where m is a material constant, σh and σe are the hydrostatic and equivalent von Mises stresses, respectively.

A new coalescence equation is based on previous work by Horstemeyer, Matalanis et al. (2000) where coalescence effects were studied as a function of temperature and void arrangement in a matrix. The equation introduced here is a function of both pore size and pore spacing.

$$\dot{C} = TC \left(\frac{4d_0}{NND} \right)^{\zeta} \dot{\varepsilon} \tag{4.10}$$

where T is the temperature, d0 is the pore diameter, NND is the pore nearest neighbor distance, ε is the total strain, and ζ is a material constant. The coalescence equation implements the findings of Horstemeyer, Matalanis et al. (2000) that the critical distance between voids resulting in maximum coalescence was four pore diameters between voids. The coalescence equation is illustrated by a non-linear behavior as observed in Figure 4.2 where the effect d_0 has on coalescence is depicted.

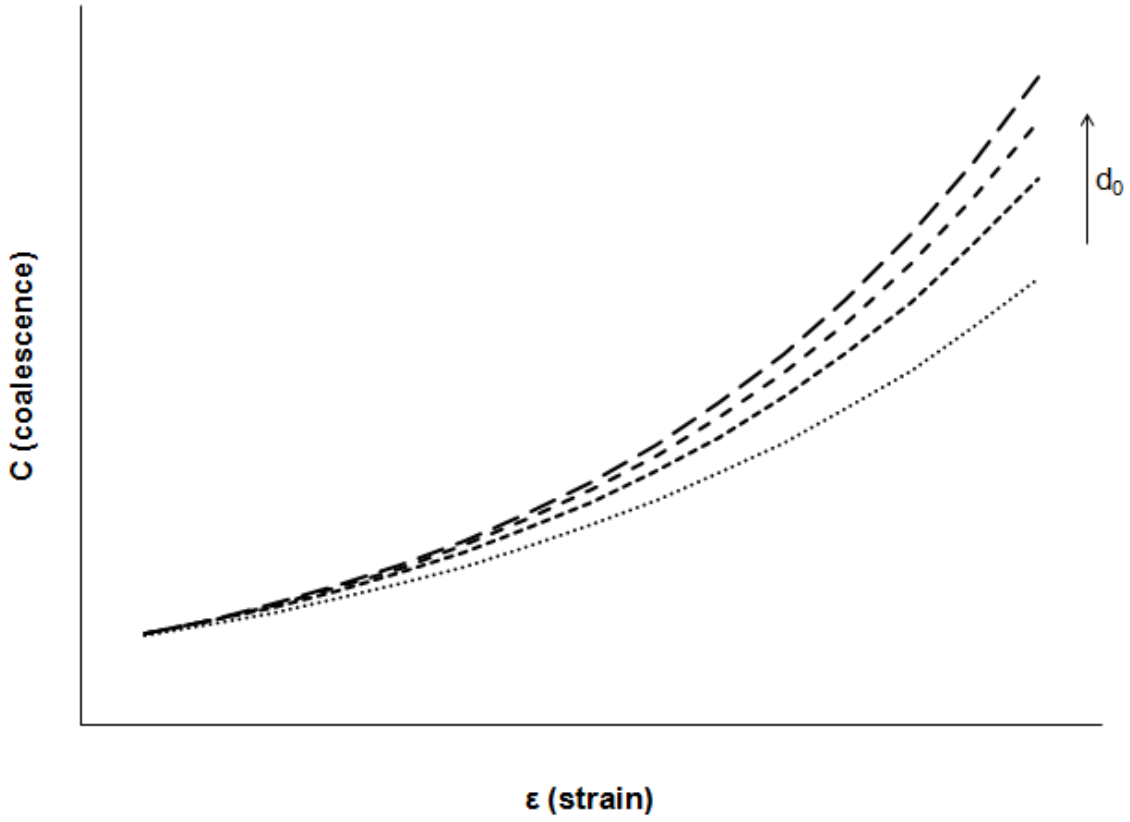

Figure 4.2 Plot portraying how an increasing pore diameter effects the coalescence equation.

The trend in Figure 4.2 depicts the coalescence increasing more noticeably at higher strain levels when the average pore diameter, d_0, was increased. A similar trend is observed in Figure 4.3, which illustrates the effect of how increasing the material constant, ζ, adjusts the coalescence equation.

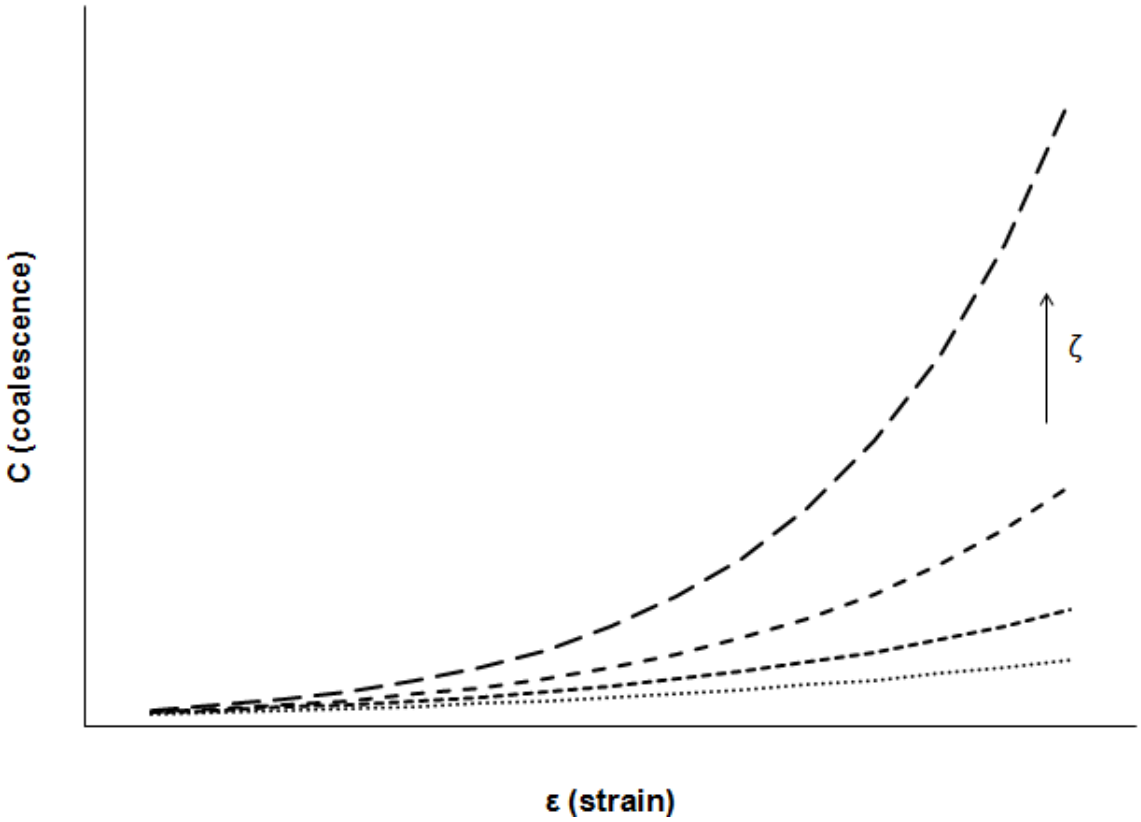

Figure 4.3 Increasing material constant, ζ, resulting in an increase in the coalescence equation.

As the constant ζ is increased more non-linearity is observed for the coalescence at higher strain levels than lower values as seen in Figure 4.3. A higher value of coalescence is also illustrated with an increasing ζ. The dependence of how increasing the distance between voids adjusts the coalescence equation is clarified in Figure 4.4.

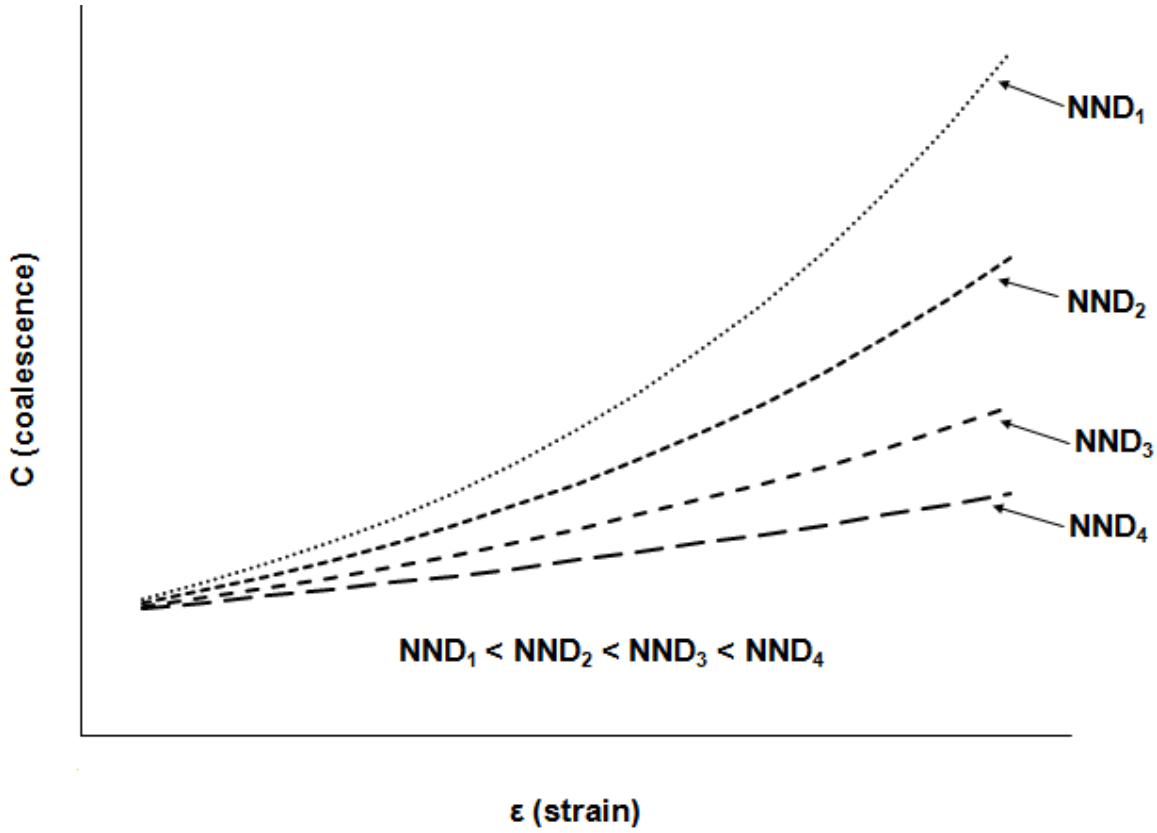

Figure 4.4 Change in void nearest neighbor distance, NND, effecting the coalescence equation.

The increase in void spacing is depicted in Figure 4.4 as reducing the amount of coalescence. More non-linearity and higher values of the coalescence equation curve are observed as the distance between voids decreased.

Model Set-up and Calibration on FC-0205

The plasticity-damage model required calibration before use in the design optimization process. To calibrate the model, a set of constants are determined that describe the model for a certain material. One set of the constants are determined by

using experimental data's true stress-true strain response for different stress states, strain rates, and temperature effects. The other set of the constant are determined from the microstructure information of the experimental specimens and the open literature.

Material Composition

Water atomized iron powder, Atomet 1001, from Quebec Metal Powders (QMP) is the base iron powder for the FC-0208 material used in the study. A nominal composition of 2 wt% Cu, 0.05 wt% graphite, and balance iron was blended and binder treated were pressed and sintered into rectangular compacts with sintered densities of 6.35 g/cm3 and 7.05 g/cm3 via a proprietary process developed by Metaldyne (2007).

Experimental Procedure

A series of compression, tension, and torsion experiments were performed to quantify the microstructure-property correlations for calibration of the internal state variable plasticity-damage model that admits heterogeneities of microstructures and defects. Tension and compression tests were performed on standard ASTM specimens machined from the sintered blanks. ASTM E8 flat tensile specimens with a gage width of 6.35 mm, a gage thickness of 3.2 mm, and a gage length of 25.4 mm were used for tension testing (2004). The flat specimens were used since the elongation to failure correlated better with published data from the open literature provided in Chapter III, which depicted larger elongation to failures with lower initial porosity levels. The round specimens abnormal elongation to failure results are possibly due to faulty machining

since the flat specimens were machined from the same lot of sintered blanks. Additional round specimens were not machined due to lack of sintered blanks large enough to machine the specimens from. Cylindrical compression specimens were machined with a diameter of 8.20 mm and a height of 9.84 mm. The torsion test employed Lindholm type specimen design with an outside diameter of 19.05 mm, an inside diameter of 9.53 mm, and a gage length of 2.08 mm.

All tests were performed at a strain rate of 10-4/sec and at one room temperature of 293K. Additionally, tension and compression tests were also performed at a temperature of 593K.

High rate compression experiments were also performed on cylindrical specimens at 293K to capture strain rate effects. All tests were performed on specimens machined from rectangular blanks compacted and sintered by Metaldyne, LLC at a sintered density of 6.35 g/cm3 and 7.05 g/cm3. A detailed explanation of the structure-property experimental procedure is detailed in Chapter III.

Description of the Model

The plasticity-damage model required calibration before use in the design optimization process. To calibrate the model, a set of constants are determined that describe the model for a certain material. One set of the constants are determined by using experimental data's true stress-true strain response for different stress states. The other set of the constant are determined from the microstructure information of the

experimental specimens and the open literature. The material constants are provided in Appendix A.

Fracture toughness, $K_{IC} = 40 MPa\sqrt{m}$ was obtained from literature, German (2005). However, the initial void radius, void volume fraction, initial particle size, particle volume fraction and grain size were determined from microstructural analysis as discussed previously in Chapter II.

Besides using image analysis for determining the constants, the program is used for examing the fracture surface of the specimens to quantify the damage parameters seen in Table 4.1.

Table 4.1 Damage parameters obtained from fracture surfaces of low and high porosity ambient (293K) tensile specimens.

	Low Initial Porosity Specimens	High Initial Porosity Specimens
φinitial	0.09	0.19
d (μm)	32.03	27.41
v·c (μm2)	806.72	591.38
η (#/μm2)	0.0009	0.0015
φfracture	0.73	0.92

The damage parameters are obtained from fracture surface image analysis of three specimens for each initial porosity level. Specimens with lower initial porosity exhibited a larger average pore diameter, d, on the fracture surface than the higher initial porosity specimens. The data also shows the specimens with less initial porosity experience more

void growth, v, and coalescence, c, than the specimens with higher initial porosity. Nucleation, η, shows the opposite trend for where the low initial porosity specimens showed decreased nucleation when compared with the high initial porosity specimens.

DMGFIT, a fitting software developed at MSU based on the ISV plasticity-damage model, was used for determining the plasticity and damage constants for the model. Simultaneous fitting of the different curves (tension, compression, and torsion) are capable with the DMGFIT software as shown for the low initial porosity and high initial porosity in Figure 4.5 and 4.6, respectively.

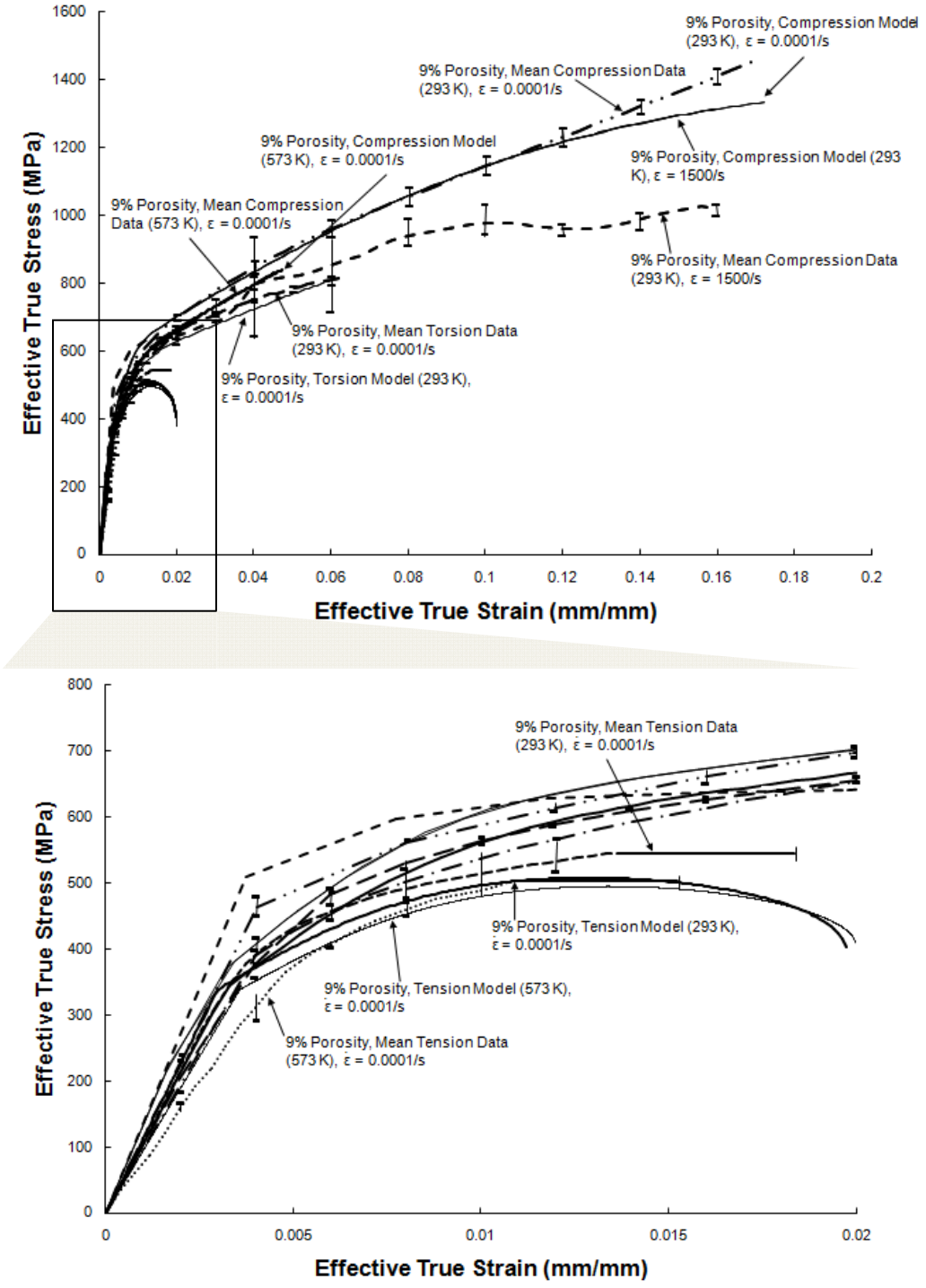

Figure 4.5 Internal state variable plasticity-damage model calibration for mean monotonic stress-strain behavior under different stress states and temperatures with a low initial porosity.

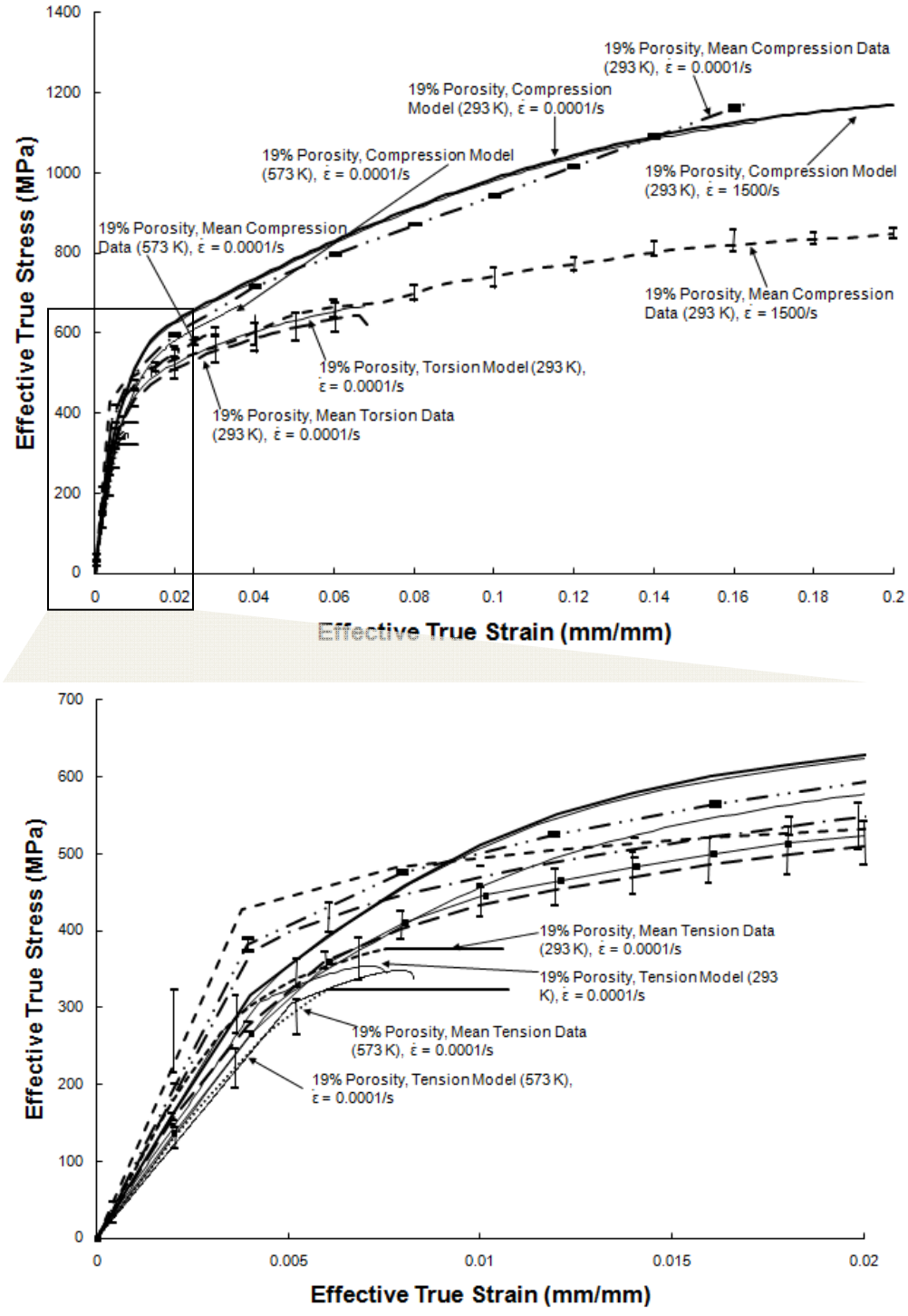

Figure 4.6 Internal state variable plasticity-damage model calibration for mean monotonic stress-strain behavior under different stress states and temperatures with a high initial porosity.

The smooth lines in Figures 4.5 and 4.6 are the model results, where the data points are averaged experimental data from experiments tested at different stress states, strain rates, and temperatures for low porosity specimens in Figure 4.5 and high porosity specimens in Figure 4.6. The hardening and recovery of the experimental data curves are predicted well by the model for low strain rate tests. Further fine tuning of the model constants would allow for more accurate prediction of the high rate compression data. The model captured the elongation to failure of the tension specimens within the uncertainty of the experimental data.

The high porosity of the bearing cap results in some pore growth but mainly through pore coalescence evolution more than nucleation. A finite element model of a unit cube was used for predicting tension and compression. The unit-cube has a shortened run-time, while still capturing the same uniaxial stress-strain response of a full scale specimen. Torsion prediction utilizes a full-scale specimen due to a more complex loading condition.

The unit cell prediction of model-experiment compression testing at 573K is plotted in Figure 4.7. The mean data is an average of two high porosity experiments and two low porosity experiments. The upper bound data are the maximum stress values at a certain strain level, while the lower bound data are the minimum stress values. An upper bound model curve utilizes the low porosity microstructure constants, while the lower bound model curve incorporates the high porosity microstructure constants. The plasticity-damage constants are the same for both of the model curves.

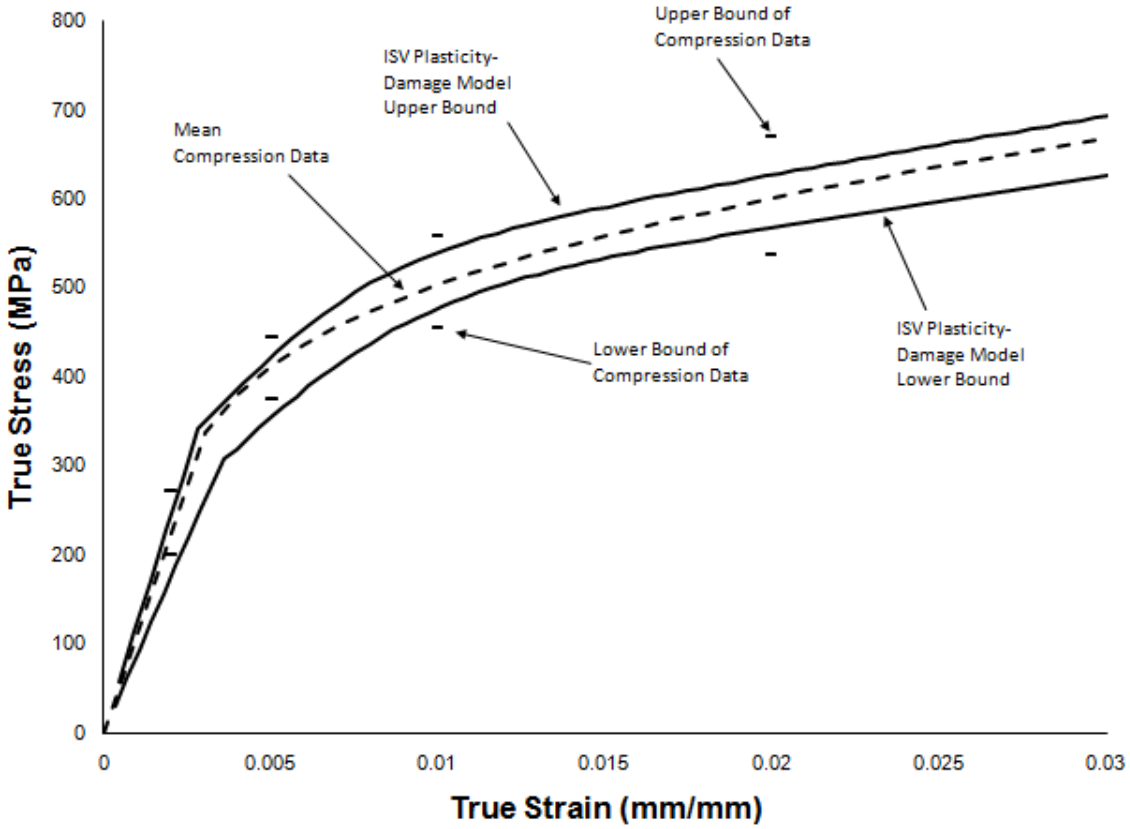

Figure 4.7 Compression experiment-model comparison at 573K.

The smooth curves representing the model prediction for the two different microstructures both predict a lower compressive modulus than the mean experimental data. The on-set of yield is also slightly under predicted for the high temperature compression experiments.

The mean ambient compression data is plotted in Figure 4.8. The mean data points are an average of two high porosity experiments and two low porosity experiments. The upper and lower bounds for ambient compression data are defined the same as the high temperature compression data.

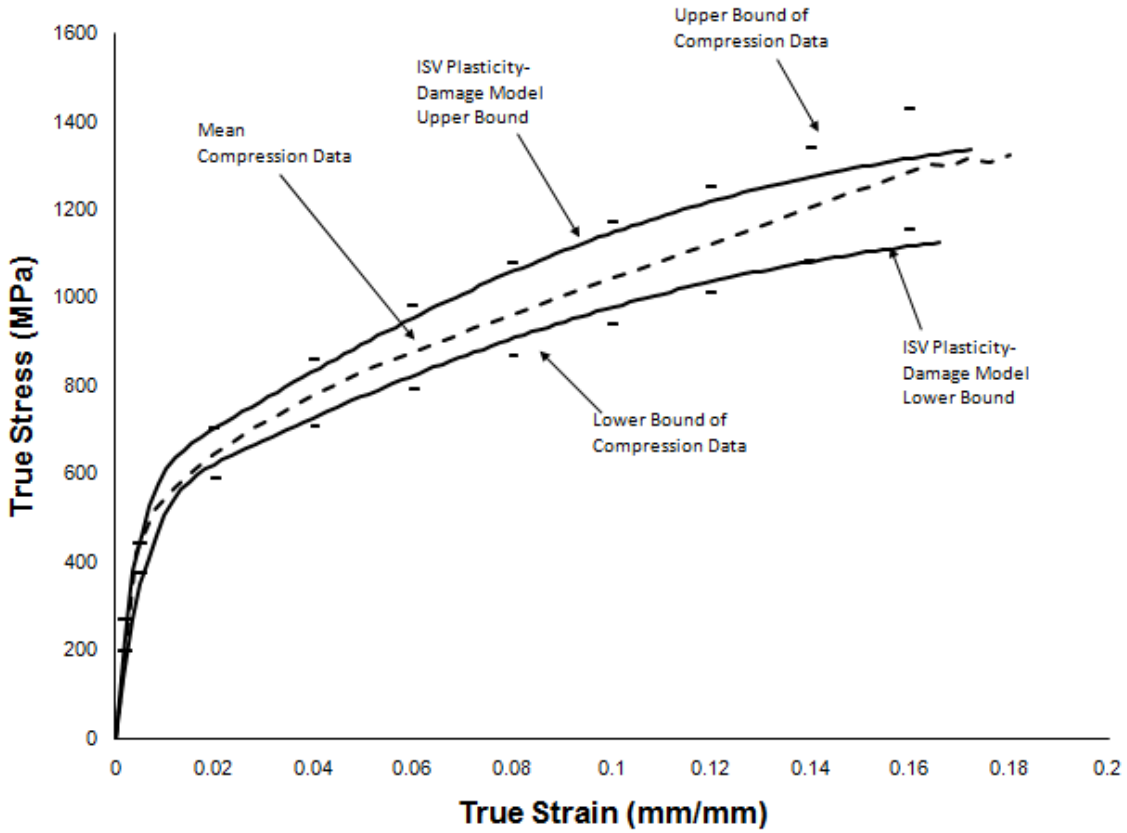

Figure 4.8 Compression experiment-model comparisons at 293K.

The upper bound model curve does a better job of predicting the compressive elastic response of the material at 293K than at 573K. The lower bound model curve still shows a slight under prediction of the materials elastic stress-strain response. The onset of plasticity is under predicted for both the upper and lower bounds of the experimental data. However, the model bounds the latter stages of the material's plastic behavior at ambient temperature.

Tension experiments at 573K are compared with the ISV plasticity-damage model in Figure 4.9. The upper bound data does not have a strain-to-failure uncertainty band due to only one low porosity experiment failing in the gage section of the test specimen. The

lower bound data does exhibit an uncertainty band for strain-to-failure. The mean data plotted is an average of three high porosity experiments and one low porosity experiment.

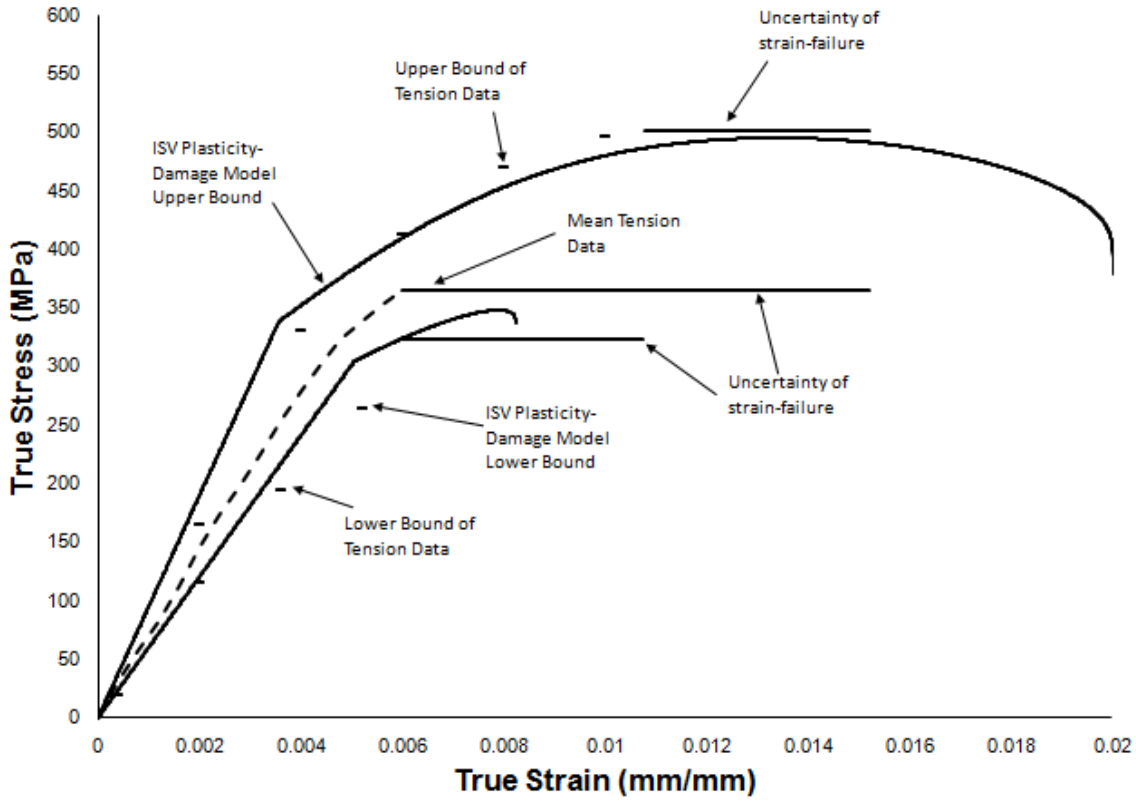

Figure 4.9 Tension experiment-model comparison at 573K.

The upper bound high temperature tension model curve predicts a stiffer elastic modulus than reported by the experimental data. The lower bound prediction of the elastic modulus is between the mean data and the lower bound of the experimental data. Both model curves portray more recovery than the experimental curves plotted, but do stay within the upper and lower experimental data bounds.

The ambient tensile test data in Figure 4.10 provides a mean data point curve from three high porosity experiments and three low porosity experiments. The upper bound and lower bound data curves both have an uncertainty band on the strain-to-failure in the figure.

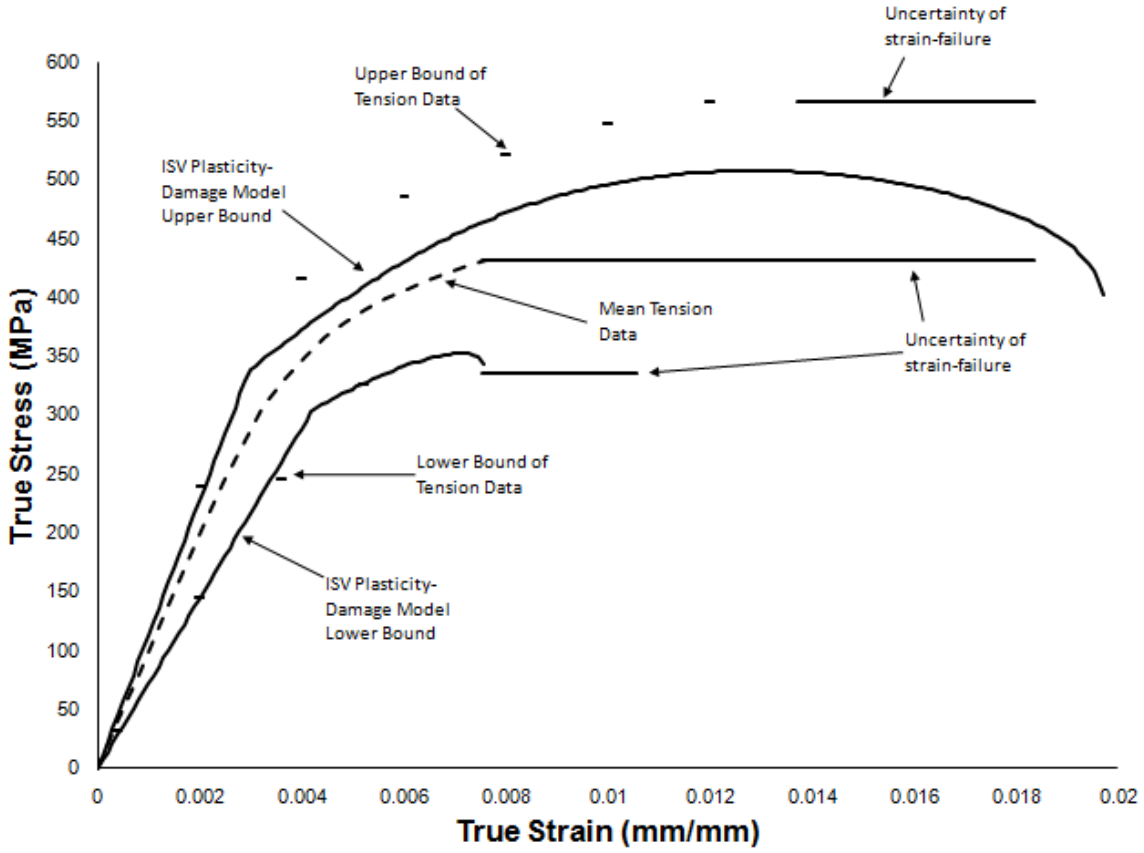

Figure 4.10 Tension experiment-model comparisons at 293K.

The on-set of yield is predicted by the model curves even though the elastic modulus appears slightly lower than the experimental data. For the upper bound model curve, the modulus is plotted lower than the mean data and the lower bound model prediction plots the curve below or on the lower bound data (data shows that experiment

is not linear all the way to where we are predicting yield.). The plastic hardening and recovery portions are captured by the model since the upper bound model is plotted between the mean and upper bound data. The plasticity portion of the lower bound model is graphed between the lower bound data and the mean data points.

The damage evolution curves are plotted in Figure 4.11 for both the 293 K and 573 K tensile experiments.

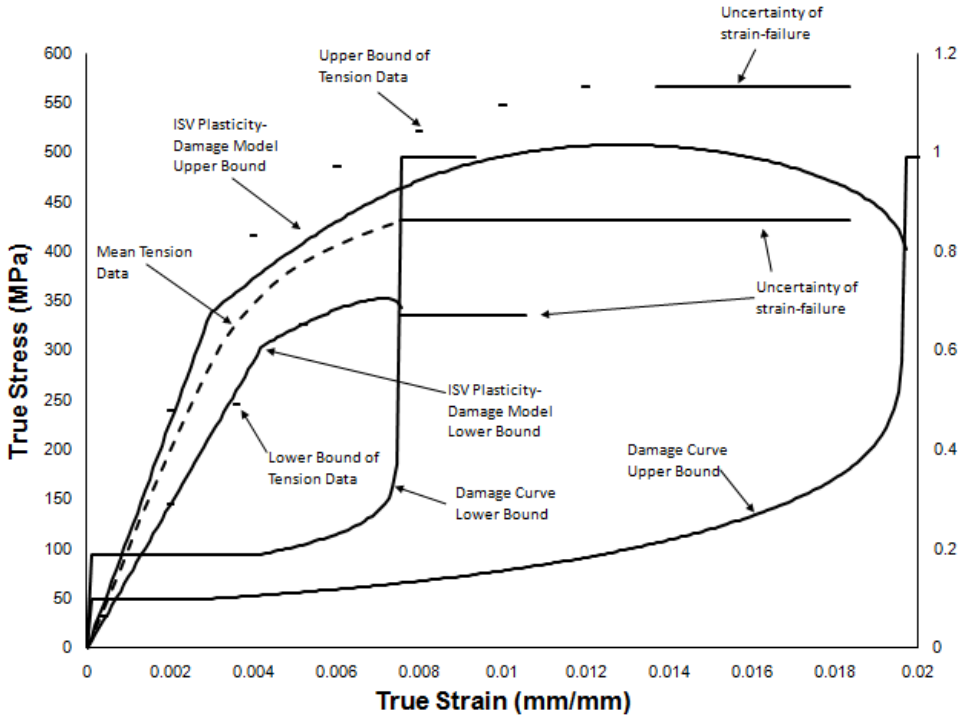

(a)

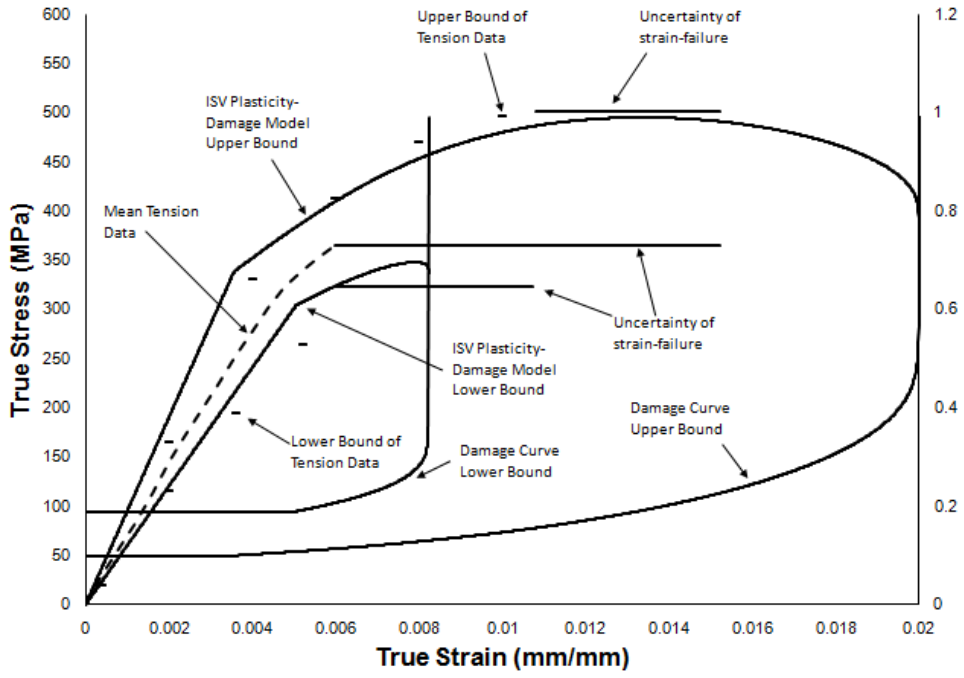

(b)

Figure 4.11 Experimental and finite element model simulated stress-strain curves and damage evolution for the uniaxial tension tests carried out at (a) 293 K and (b) 573 K.

The damage evolution in Figure 4.11a and 4.11b for the low initial porosity tensile specimens under predicts the damage evolution resulting in slightly larger strain-to-failures than what was observed experimentally. However, for the high initial porosity specimens the elongation-to-failure is within the uncertainty band of the experimental data for the two temperature levels.

Model Validation of FC-0205 Powder Metallurgy Steel

Once the material constants were determined during the calibration phase, they no longer should be altered. Validation of the model occurred by comparing the plastic and damage behavior of the material with notch Bridgman tensile specimens and the main bearing cap.

Bridgmann Notch Tensile Testing Validation

The notch Bridgman specimens allow for different triaxiality conditions to influence the damage behavior. Two different notch radii are chosen for the analysis. The specimens are labeled R60 and R150 having a notch radii of R = 0.15 cm and R = 0.38 cm, respectively. The ratio between one half of the cross-sectional diameter of the specimen at the centre of the notch, a, respect to the notch radius, r. Therefore, R60 has a ratio a/r=0.142/0.06 =2.367 and for R150 the a/r=0.142/0.075=1.893.

Monotonic loading of notch Bridgman specimens was performed up to and including failure. The use of the notch geometry creates stress triaxiality gradients in the specimens similar to structural components, allowing for experimental and numerical

methods to be validated since the model calibration experiments were conducted under homogeneous stress states. Once the mechanical testing was completed, the specimen's damage was determined using computed tomography.

Experiments on notch Bridgman specimens were performed to failure and then other specimens were tested to 98%, 95%, and 90% of the failure load using an Instron 5882 testing machine, with a +100 kN maximum loading capacity. Although the tests were run in strain control using an Instron 2630-052 extensometer at a strain rate of 0.0001/s in the unnotched region, the load was monitored to know when stoppage occurred. Next, a Phoenix X-ray Computed Tomography (CT) system was used to evaluate the specimens. Figure 4.12 and 4.13 show the load displacement curves for the 0.38 cm notch root radius and 0.15 cm notch root radius Bridgman specimens. A comparison of Figure 4.12 and Figure 4.13 reveals a size effect, with the larger radius exhibiting more plasticity than the smaller radius specimens during testing.

Image analysis results of the microstructure showing void characteristics of the notch tensile specimens are provided in Figure 4.14. The pore diameter, nearest neighbor distance and porosity level data obtained from image analysis of optical micrographs of the notch specimens examined as in Figure 4.14 is provided in Table 2.

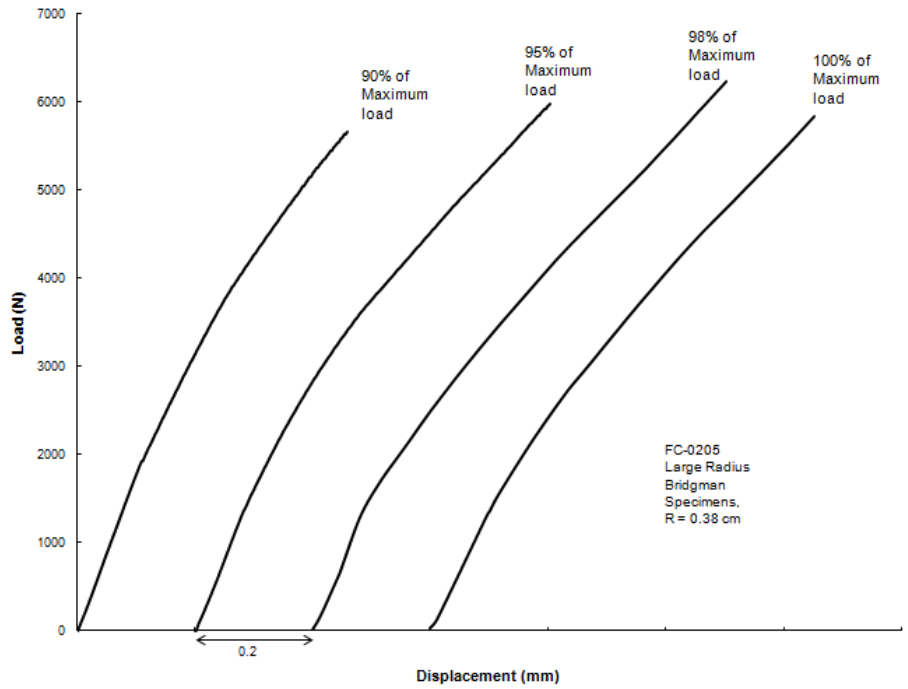

Figure 4.12 Bridgman specimens with a 0.38 cm notch root radius at 90%, 95%, 98% of failure load compared to a specimen tested to failure.

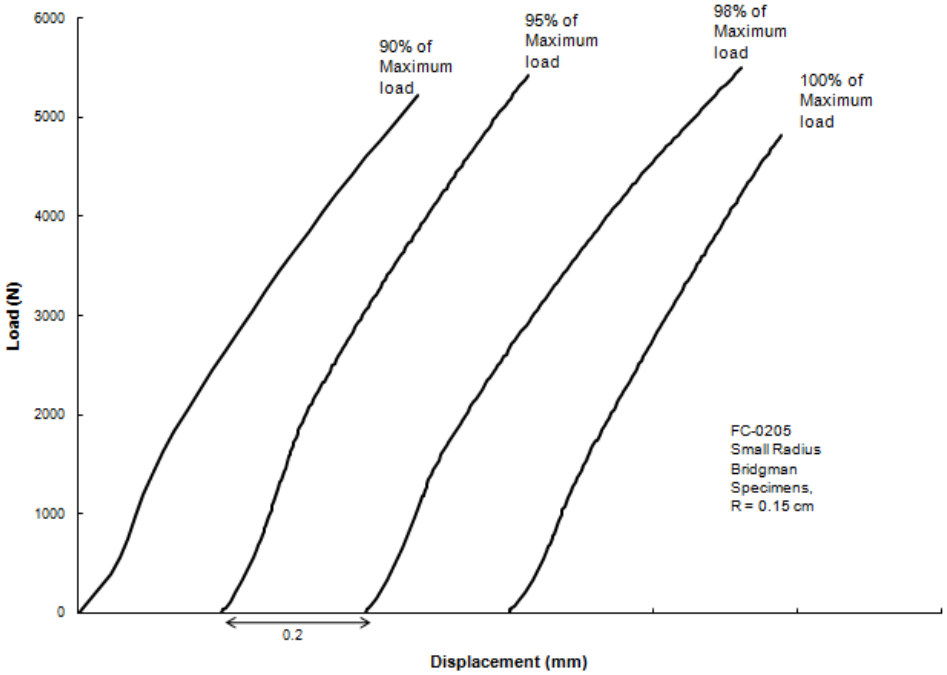

Figure 4.13 Bridgman specimens with a 0.15 cm notch root radius at 90%, 95%, 98% of failure load compared to a specimen tested to failure.

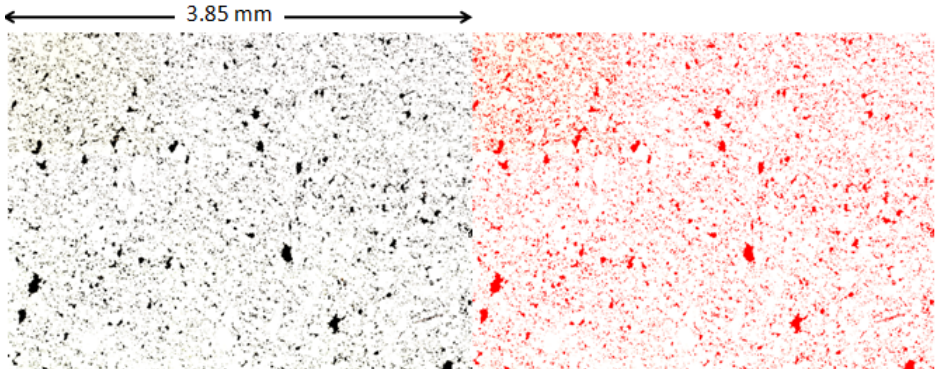

Figure 4.14 Initial porosity optical micrographs of notch tensile specimens at 293K before and after image analysis for the low porosity specimen.

Table 4.2 Image analysis of the initial porosity optical micrographs for the notch tensile specimens.

Low Porosity Image Analysis	Small Notch Root Radius		Large Notch Root Radius	
	Average	Maximum	Average	Maximum
Pore diameter, d (μm)	8.34	130.13	8.31	149.04
Nearest Neighbor Distance, *NND* (μm)	12.62	72.61	12.51	69.65
Porosity, φ	0.0972	-	0.0939	-
Void nucleation density, η (#/μm^2)	54.7	-	54.2	-
Void volume *coalescence, $v \cdot c$ (μm^2)	0.00178	-	0.00173	-

Fracture surfaces of the Bridgman specimens for both notch root radii are shown as SEM images in Figure 4.15. SEM analysis of the Bridgman fracture surfaces depict the powder particles with cleaved and microvoid fractures for both radii tested. The image analysis results of the fracture surface provided the damage information in Table

4.3. The results from these surfaces show that coalescence is the main source of damage growth, as there is not much void growth during deformation.

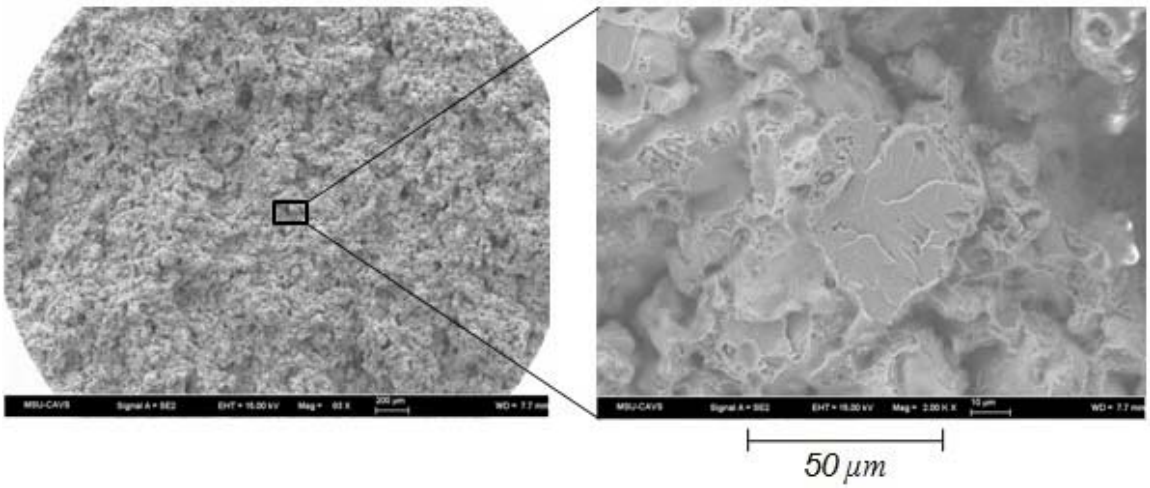

(a)

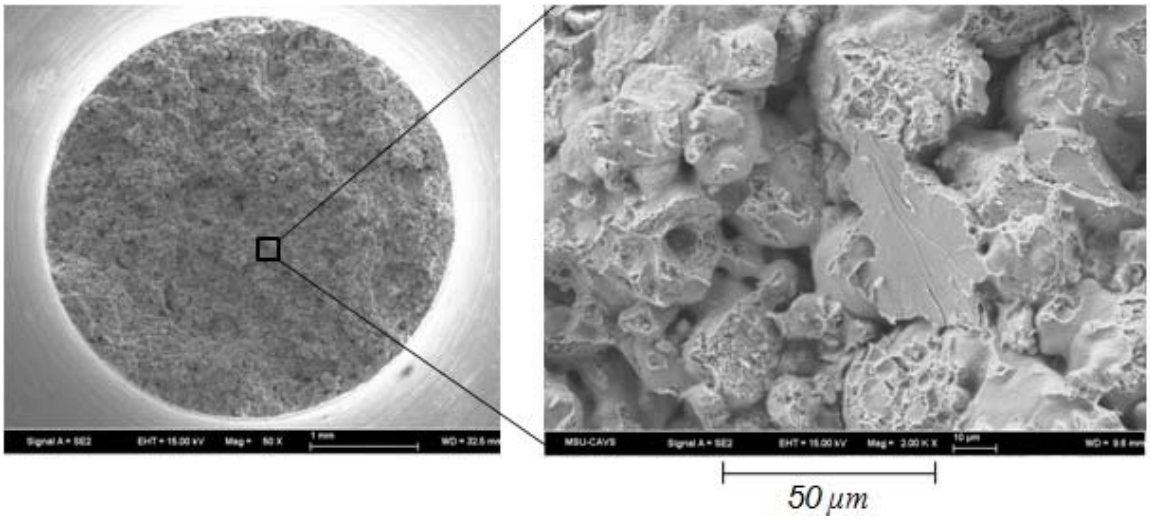

(b)

Figure 4.15 SEM fracture surface images of Bridgman specimens with notch radius of (a) 0.38 cm and (b) 0.15 cm.

Table 4.3 Damage parameters obtained from fracture surfaces of large and small notch root radii tensile specimens.

	Large Notch Root Radius	Small Notch Root Radius
Pore diameter, d (μm)	24.58	21.64
Void volume *coalescence, $v \cdot c$ (μm^2)	474.57	367.79
Void nucleation density, η (#/μm^2)	0.0018	0.0023
Porosity, φ	0.86	0.85
Nearest Neighbor Distance, *NND* (μm)	9.08	4.30

To validate the notch tensile tests and predict the location of failure, the notch specimen is modeled using the finite element method. The notch is modeled and then assembled in ABAQUS/CAE as shown in Figure 4.16. The notch is modeled as a deformable body with Young's Modulus as a function of density as defined in the user material subroutine UMAT. The notch is modeled with C3D8R continuum brick elements. The notch is subjected to displacement time loading in which the lowest cross-section of the notch is fixed and the top part is subjected to loading as shown in Figure 4.16. Under the loading, the stresses throughout the notch are within the elastic-plastic domain, the mechanical properties of the notch are therefore defined by a user material subroutine UMAT in which the elastic material properties are porosity-dependent. The density distribution in the notch is also defined in the user material sub routine for each material point of elements.

Figure 4.16 Model of Notch specimen for finite element analysis.

Damage levels are directly proportional to the magnitude of the triaxiality. Thus, larger levels of triaxiality will not only translate in a greater regions where the voids grow and coalesce. To validate the accuracy of the plasticity-damage model, both the plasticity and damage progression were analysed using the finite element model for each of the notched specimens tested. As shown in Figure 4.17, the contour plots of these results indicate that the central region in specimen has the highest level of triaxiality.

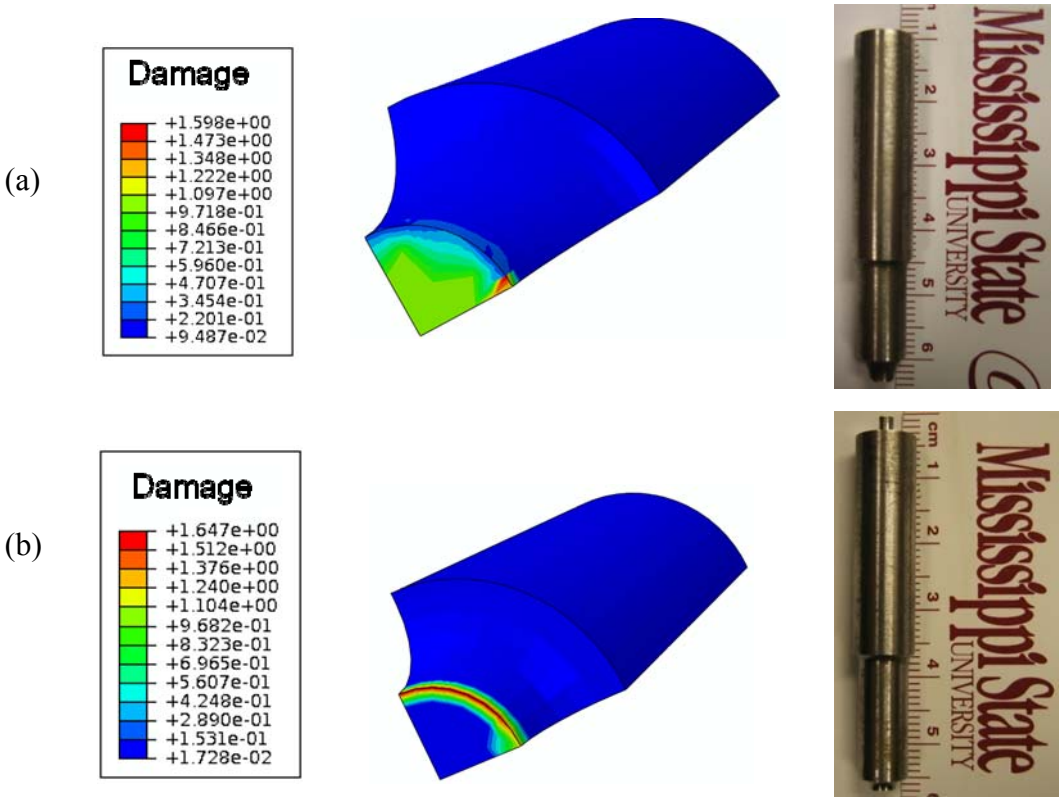

Figure 4.17 Comparison of failure location for the (a) R150 and (b) R60 notch tensile specimens with failure denoted by the damage parameter in the finite element simulations.

The load-displacement curves for the notch specimens are used to "validate" the plasticity of the model and clearly the model follows the experimental trends as shown in Figure 4.18. The model predicts the maximum load and fracture displacement for the R60 and R150 specimens. All modeled curves show a very slight variation in the elastic slope, while in the experiments the variation is more noticeable. The model also predicts satisfactorily the elongation path for the R60 and R150 notch specimens.

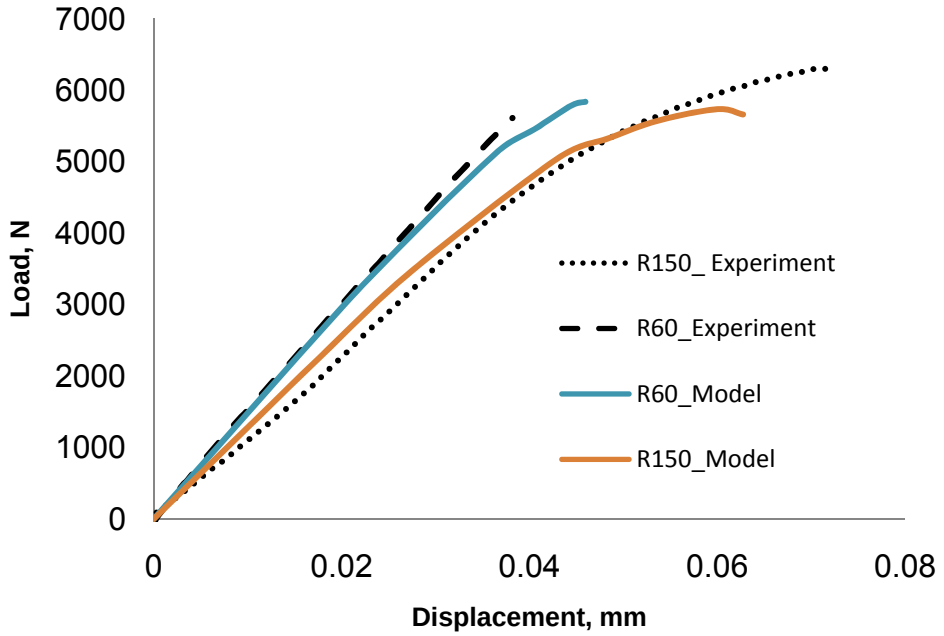

Figure 4.18 Load-displacement comparison between the experimental results and the finite element model (FEA) for notch tensile tests with R60 and R150 specimens.

Figure 4.18 shows a good correlation between the experimental and finite element model results. The model predicts satisfactorily the damage location of the notch subjected to tensile loading. Stress triaxiality at the centre of the notch as shown in Figure 4.16 causes the voids to grow and coalesce which results in damage near the center of the notch. Furthermore, the finite element model predicts the same load displacement curve as the experiment up to a maximum point where damage initiates.

Main Bearing Cap Validation

Computational and mathematical based modeling for describing the mechanical behavior of components during monotonic testing process is recognized as providing

significant contribution to study the durability and life of components. These techniques are helpful in predicting the location of failure of the component, stress distributions, cracks initiating during the tensile or fatigue loading. However, for constitutive laws to be accurate and successful, computer simulation should be accompanied with a complete experimental database for validation. These validation experiments comprise several test methods such as monotonic load testing and fatigue testing of the automotive main bearing cap.

Monotonic tension experiments were conducted on sintered main bearing caps (MBCs) at room temperature (~273 K) in laboratory air with relative humidity near 45-60 RH. The tests are being performed to validate the ISV plasticity-damage model developed for powder metallurgy material. Loading is applied on the legs of a MBC as shown by the arrows in Figure 4.19.

Figure 4.19 Test fixture and loading application of the MBC.

Testing was conducted on a 20 kip MTS load frame. Programming the test, controlling the experiment, and collecting data were performed by using the MTS controller application, Multipurpose Test Ware (MPT). Testing was conducted in displacement control at a rate of 0.25mm/s. The MBCs were preloaded to 30 lbf, which ensures the load is applied at the end of the bearing cap feet. A nut and bolt was used to set the location of loading and also to ensure the surface of the MBC parallel to the washers in Figure 4.19 stays in the same plane as per the finite element simulations. Data acquisition was recorded every 100 ms by MPT with extension, load, and displacement recorded. The load-displacement curves of the MBCs resulting from the monotonic tests are reported in Figure 4.20, where the displacement is reported from the crosshead displacement of the load cell. The failure location was the same for all the MBCs tested.

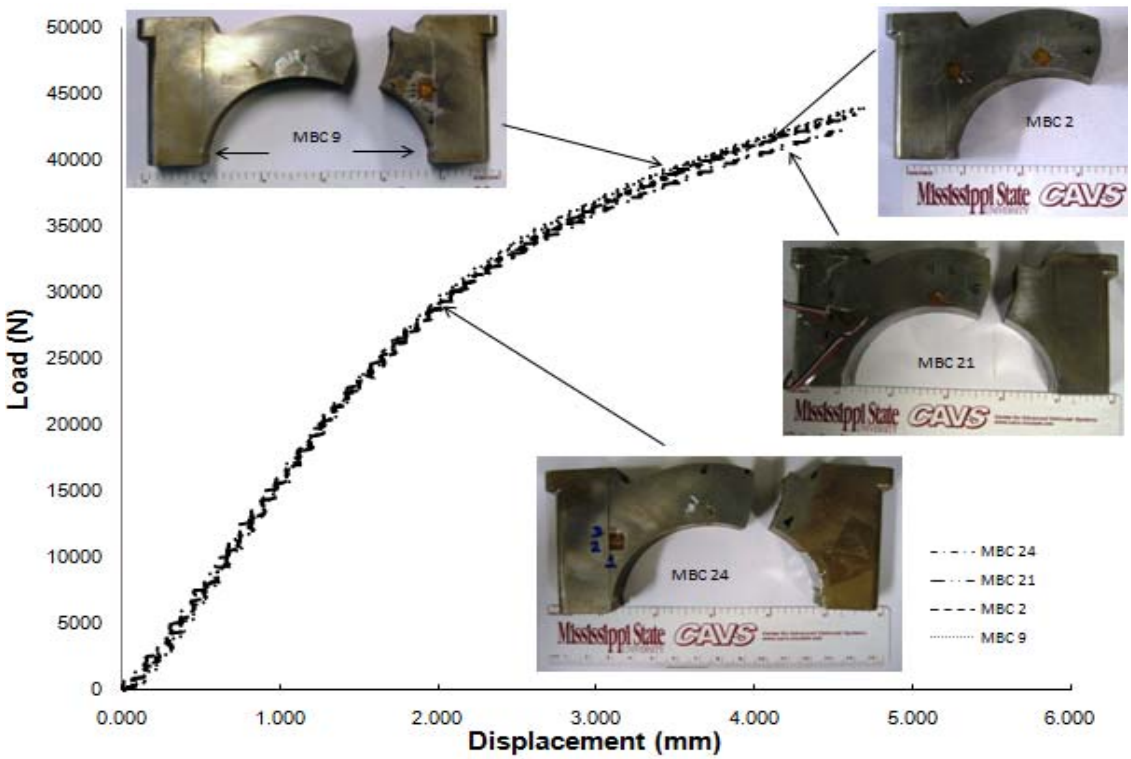

Figure 4.20 Plot of load versus displacement for the monotonic MBCs.

To validate the monotonic load tests and predict the performance of the MBC, the fixture for the performance test is modeled using the finite element method. All the components of the monotonic load fixture are modeled separately as shown in Figure 4.19 and Figure 4.21. The components of the monotonic load fixture were meshed separately and then assembled in ABAQUS/CAE (Figure 4.20b). The mesh consists of the MBC as a deformable body and two rods going through each end of the bearing cap. The rods are meshed as a rigid body with R3D4 rigid elements, while the bearing cap was meshed using C3D8R continuum brick elements. Since rods were defined as the rigid bodies, they were not influenced by the forces and stresses acting on the model.

Boundary conditions were applied to the rods, with loading applied to one rod while the other rod was fixed. As shown in Figure 4.21a, the porosity distribution of the MBC from the compaction computational results were used as input to the performance model (sintering in this case did not affect the porosity distribution). Because the density variation during sintering was very small (0.2-0.3%) for the FC-0205 iron-based powder, the density variation during sintering was not considered, so the density distribution was directly mapped from the compaction FE analysis after springback, using the feature *MAP SOLUTION in ABAQUS/Standard.

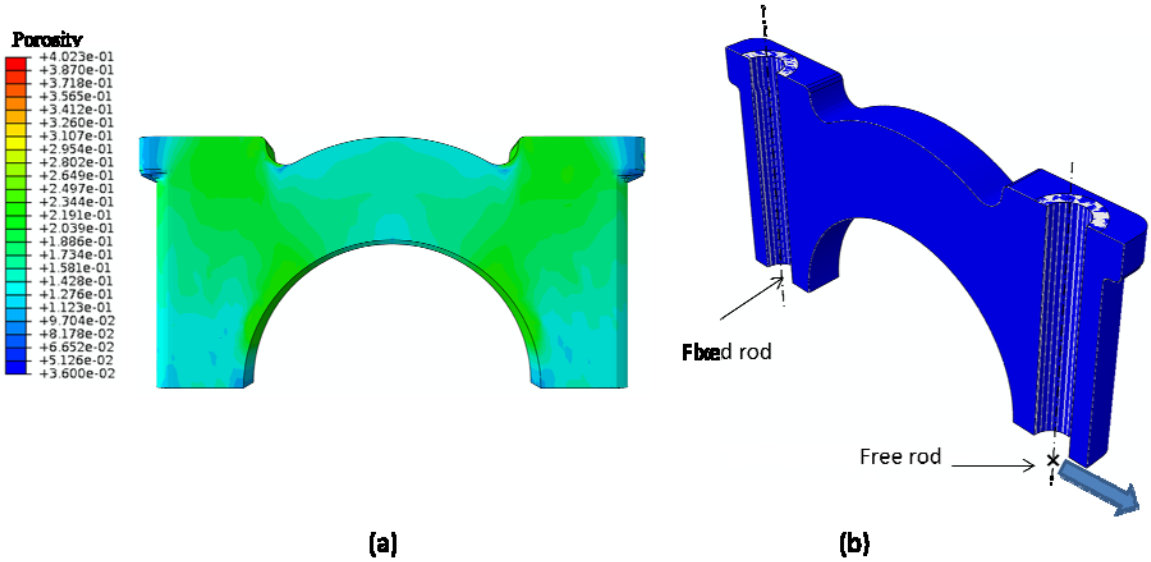

Figure 4.21 Finite element model for monotonic performance testing showing (a) the initial porosity solution (SDV28) of the MBC transferred from the compaction model results and (b) the performance model configuration with applied boundary conditions.

Once the validation of the model was finished for the notch specimens, we employed the model for further validation related to the main bearing cap (MBC). The mechanical properties of the MBC depended upon the heterogeneities of the porosity and

grain size. The material model includes damage dependent material parameters that include the direct measurements of the pore sizes, nearest neighbor distances of the pores, porosity, and grain size in order to capture the location of failure during monotonic loading. Figure 4.22 compares the monotonic testing of the MBC experiment to the finite element model results. Clearly, the performance model predicts the location of failure at the same point where the experiment predicts approximately 45 degrees in the arch. denoted by Region C. Regions A and B as shown in Figure 4.22 refer to the maximum Von Mises stress which is not the region of crack initiation and maximum damage. The Von mises stress is typically used to determine the "hot" spot on a component for failure. However, these simulations indicate that the Von Mises stress would have given the wrong location and thus should not be used for the criterion for crack initiation, because it does not take into account the heterogeneous porosity distribution in the bearing cap.

Another part of the validation is related to the measurement of strains in a region not necessarily near the fracture location. Strain gages were applied to the MBC as shown in Figure 4.22b. Figure 4.23 shows that the simulation strain versus displacement follows that of the experiment.

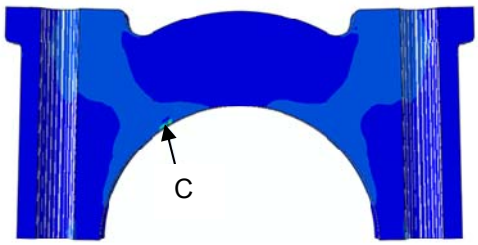

(a)

(b)

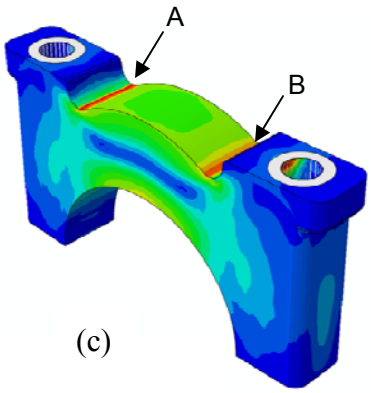

(c)

TYPE	REGION
Maximum von-Mises Stress	A, B
Crack initiation region	C

(d)

Figure 4.22 Comparison of (a) finite element model with (b) experimental results indicating the crack initiation point and (c) the regions of maximum von Mises with the tabulated results shown in (d).

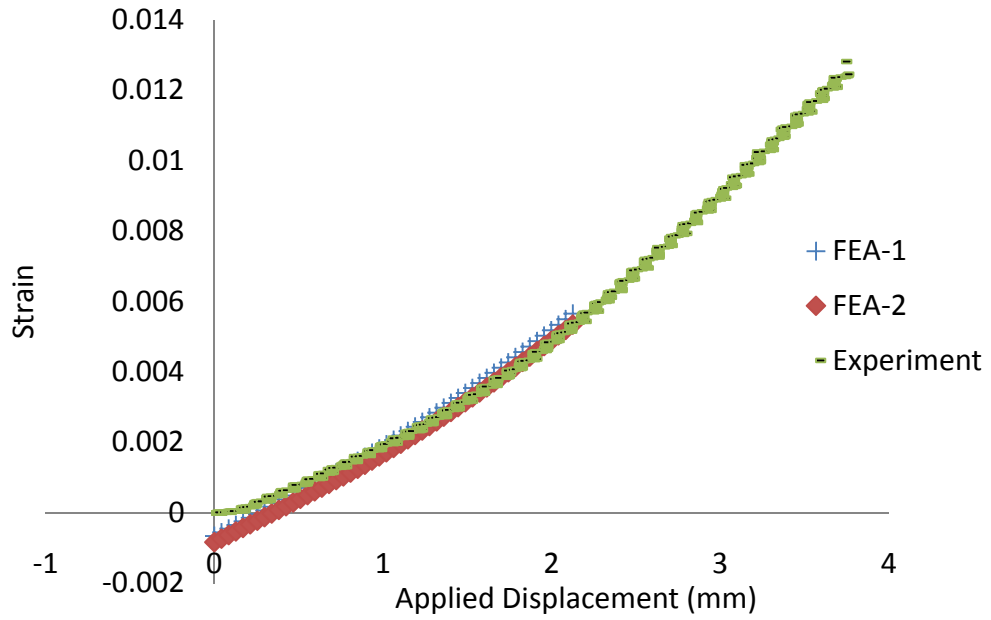

Figure 4.23 Comparison of the experimental data with the finite element model at two different locations of bearing cap (where the strain gage is located).

The comparison of the finite element simulations with the experimental results illustrates a good correlation between the model and tests. Now that the calibrated ISV plasticity-damage model was validated via the notch tensile specimens and the MBC, it can be used with confidence for design and analysis of powder metals and structural components.

Conclusions

An ISV constitutive model previously developed for wrought and cast materials was used to examine the microscale plasticity-damage model correlation with experimental monotonic tests on a commercially available powder metallurgy material

(FC-0205). The addition of a new coalescence ISV equation to the existing model allowed for accurate calibration of the model using experimental tension, compression, and torsion tests that allowed for material characterization of the material. Calibration of tension and compression experiments were done at temperatures of 293 K and 573 K, while torsion calibration was limited to 293 K. Calibration of the model was also performed by using high rate compression data at 293 K. Validation of the model was then accomplished using notched tensile specimens with different triaxiality levels and monotonic testing of PM components. The validation analysis utilized load versus displacement curves when comparing the model to the experimental results. The mechanical behavior was satisfactoraliy predicted for the quasi-static loading conditions even though certain discrepancies were observed in the results. Discrepancies were attributed to experimental uncertainties and model approximations.

CHAPTER V

MODELING AND EXPERIMENTAL STUDY OF THE FATIGUE OF FC-0205 POWDER METAL STEEL

Introduction

Computational and mathematical based modeling of the thermo-mechanical behavior for powder metallurgy component design and performance prediction are recognized as significant contributions to improving efficiency, quality and cost of current production and generating new business opportunities for the automotive industry. PM techniques are being incorporated to manufacture various complex shaped engineering components, which prove difficult to cast or shape by alternative procedures. A motivating factor driving the development of a mathematical based model is the ability to accurately predict the variation in property performance caused by inhomogeneous density distribution. Research addressing mathematical modeling will provide several benefits including: near net shape components, complex geometries, high strength and minimal or eliminated finishing operations Hammi, Stone et al. (2006).

Influence of Porosity on Fatigue Properties

Porosities effect on fatigue behavior has been documented by researchers such as Christian and German (1995) who reported pore size, pore shape, pore spacing, and

percent porosity as controlling factors of fatigue behavior for an Fe-Cu-C PM alloy. Klumpp, Eifler et al. (1992) also examined Fe-Cu-C alloys along with Fe-Cu and Fe-P alloys. The researchers observed that with decreasing porosity and increasing the number of rounded pores, the plastic deformation was more homogenous and crack initiation is delayed. Pores and pore clusters near the specimen surface were reported as the sites of crack initiation by many researchers according to Chawla and Deng (2005) who studied Fe-Mo-Ni steel alloys. The authors commented that pore size and pore clusters acted as stress concentrations for the initiation of fatigue cracks, which verifies the same conclusion reported by Sudhakar (2000). Sudhakar (2000) also found that crack propagation during fatigue was due to crack linking and/or joining of isolated pores. Previous work by Chawla, Murphy et al. (2001) similarly relate the propagation of cracks to be dependent on mean pore spacing. Stating the authors observed that a longer distance for cracks to travel between pores results in a higher fatigue life.

Other work on fatigue of PM materials has been done by Lindstedt, Karlsson et al. (1997) who tested austenitic stainless steel. The researchers reported that the nucleation of fatigue cracks predominately occurred at or near the surface, where cracks nucleated around 10% of the total life. Surface crack linking was identified in the higher porosity steel and tendency of linking was not found in the low porosity steel. High strength low alloy PM steel FL-4405 researched by Poland, Stephens et al. (1998) showed that lower porosities produced an increase in fatigue resistance over higher porosities, and concluded that pore size and percent porosity influenced tensile stress-strain, fracture toughness, and fatigue resistance compared to an increase in pore roundness.

Current PM Fatigue Modeling

Fatigue analysis of PM materials has been statistically analyzed by researchers Lin, Lee et al. (2001), Williams, Lee et al. (2003), Engler-Pinto Jr., Lasecki et al. (2006). However, fatigue models for PM materials have been developed that only apply to certain PM materials or only certain fatigue regimes. A comprehensive multistage model for PM components is still required.

Current work includes an artificial neural network approach to examine the stress-ratio effects on fatigue propagation has been undertaken by Iacoviello, Iacoviello et al. (2004). The artificial neural network model developed looked at R values from 0.1 to 0.9 and correlated fatigue crack growth rate, da/dN, stress intensity factor amplitude, ΔK, and stress ratio, R. The restrictions on the model are that the fatigue crack propagation mechanisms cannot change, and to completely develop the model a large quantity of fatigue tests, which can prove to be expensive, are needed to correlate crack propagation to different stress ratios for training and validation of the model.

A linear elastic fracture mechanics (LEFM) framework for predicting fatigue limit by Torres, Rodriguez et al. (2004) uses an approach based on a fatigue crack growth threshold. The authors assume fatigue failure in PM high speed steels is caused by crack propagation beginning at intrinsic processing defects (inclusions, carbides, pores). Model validation has been limited to one material with a relative error given by the authors as approximately 6%.

A probabilistic model developed by Yan, Li et al. (2004) for the LCF regime of a PM material incorporates a Lemaitre-Chaboche damage model. The damage model, which is capable of capturing internal inclusions, was added to Bussac's probabilistic model that considers surface inclusions. The model assumes all the inclusions are spherical in shape and uniformly distributed throughout the component. Further assumptions are: the damage variable of a material element is equal to the damage of a specimen, the initial damage is only dependent on the size and location of an inclusion, and the LCF life of a component depends on the initial maximum damage. Test data for specimens with internal inclusions is still required for the model to be validated.

Sintered density comparisons with fatigue behavior, Young's modulus, and monotonic stress-strain behavior have been compared by Chawla and Deng (2005) for sintered Fe-0.85Mo-Ni steel. Analytical modeling using the Ramakrishnan and Arunachalam approach was used to show the experimentally observed decrease of Young's modulus with increasing porosity. To simulate the cyclic behavior, the authors used a combined nonlinear isotropic/kinematic-hardening model. Modeling was performed by using two-dimensional microstructures taken of optical micrographs as a basis for the finite element simulations. Extrapolation of the constitutive behavior of the steel matrix from tensile tests was performed allowing that the constitutive behavior was assumed constant for all the porosity levels investigated. A concern is noted by the authors that in two-dimensional modeling the pores are treated as holes, where in actuality, they are surrounded by the material matrix. The results of the modeling showed that at low densities, the pores were larger, more irregular, and highly clustered causing

significant strain localization resulting in premature failure. When the density was increased so porosity was lower, spherical pores were observed to be distributed more homogenously relating to a larger fraction of the material experiencing distribution of the plastic strain. Cyclically, the modeling showed that plastic deformation developed gradually at the corners of pores and at highly clustered pores.

A microstructure-sensitive MultiStage Fatigue (MSF) model [McDowell et al. 2003] was implemented for use on a PM steel in this study. The MSF model has been applied to cast aluminum alloys [Xue et al., 2007a], cast magnesium alloys [Xue et al., 2007b], and wrought aluminum alloys [Xue et al., 2007c,d]. Hence, this is the first usage of the MSF model for a PM steel alloy. The fatigue behavior at two porosity levels for an FC-0205 PM steel was used to calibrate the model. Quantitative analysis of the microstructure determined the pore size and shape for the two porosity levels. Fractographic analysis of fracture surfaces was performed additionally to investigate the correlation of fatigue mechanisms to fatigue behavior.

Experimental Procedure

The MSF model needs to have model correlation and validation experiments to confirm its applicability to powder metal structural components. For model correlation, uniaxial fatigue experiments were conducted on smooth cylindrical fatigue specimens under constant amplitude loading at room temperature (~25^{o}C) in laboratory air with relative humidity near 45-60 RH. Two different densities were chosen for testing. The higher average density was 6.9 g/cc and the lower average density was 6.3 g/cc.

Specimens were machined from sintered blanks with an average length of 12.3 cm, an average width of 1.6 cm, and an average thickness of 2.2 cm. The specimen design was based on ASTM standard E606 utilizing a gage section diameter of 0.64 cm as observed in Figure 5.1.

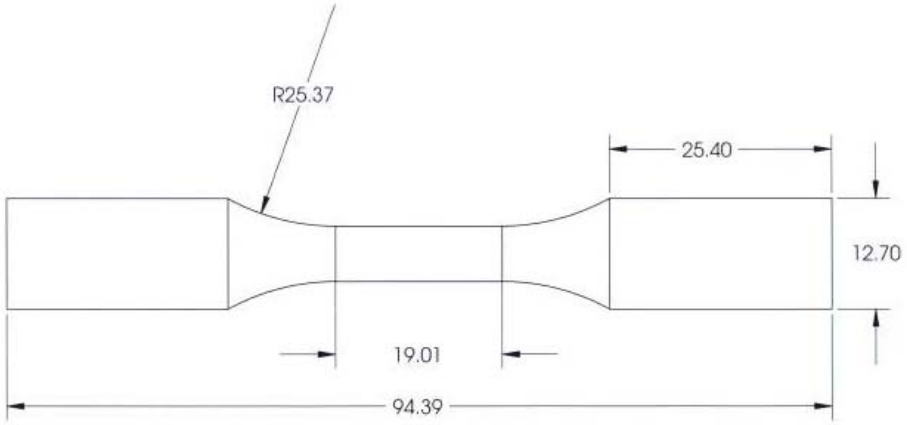

Figure 5.1 Low cycle fatigue specimen design. (units in mm).

Testing was conducted on a 20 kip MTS load frame. A MTS fatigue rated knife blade axial extensometer was used for measuring the strain. Programming the test, controlling the experiment, and collecting data were performed by using the MTS controller application, Multipurpose Test Ware (MPT). The data acquisition was set to record the data logarithmically and linearly for the MTS system. Loading was applied under strain control with a completely reversed strain amplitude. Specimens were cyclically tested by first applying a strain in tension, then uniaxially reloading in compression. The strain amplitudes tested for the high density specimens were: 0.4%, 0.3%, 0.2%, 0.175%, 0.15%, and 0.1%. The low density strain levels were 0.3%, 0.2%,

0.15%, 0.125%, and 0.1%. A frequency of 2 Hz was used when testing at strain amplitudes of 0.15% and greater. For the lower strain amplitudes, 0.125% and 0.1%, a frequency of 3 Hz was used. The aforementioned frequencies were chosen for their respective tests to avoid an instability that occurred when higher frequencies were attempted.

Results

Strain-life plots for both porosity levels are displayed in Figure 2, which also includes different R-ratios. The strain-life behavior shows that above the plastic strain limit of 0.002 mm/mm, where ubiquitous plasticity occurs, the two porosity levels are distinctly visible. However, specimens tested below the plastic limit, where failure is dominated by local cyclic plasticity, shows unclear distinctions between the two porosity levels.

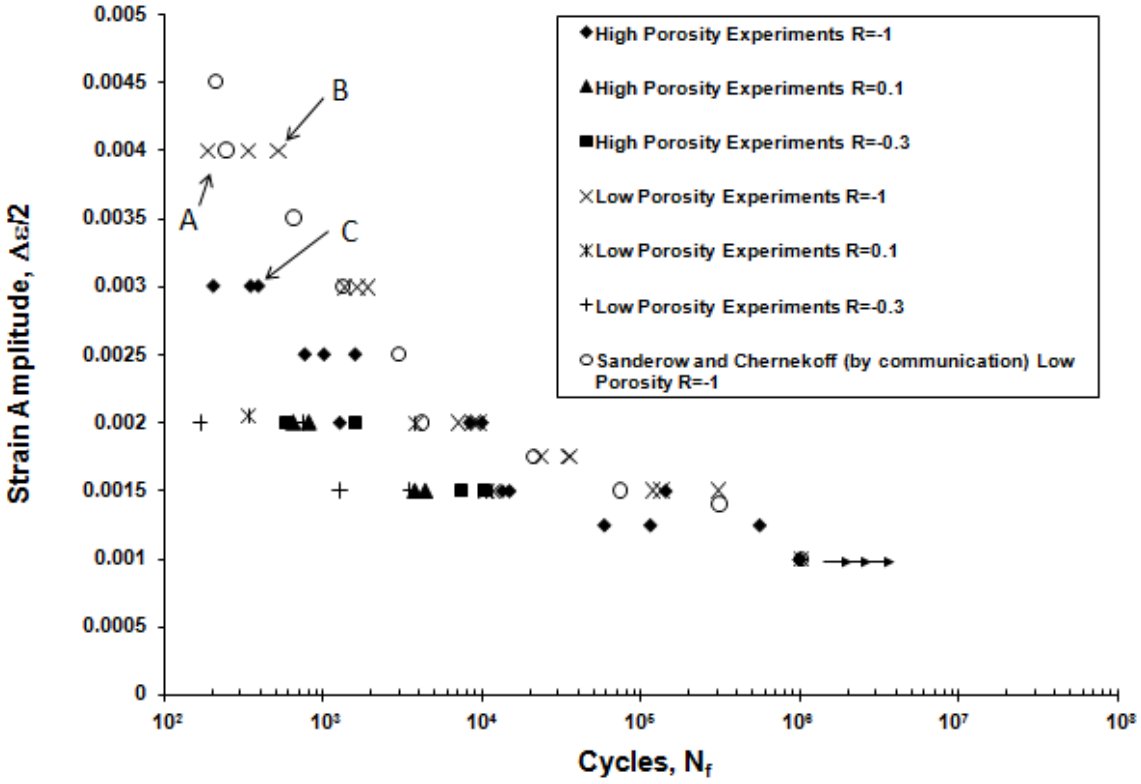

Figure 5.2 FC-0205 steel alloy strain-life curve for different porosity levels and R-ratios.

The location of fatigue crack initiation was investigated using the same FEG-SEM for the monotonic specimens. Striations were thought to have been identified that were similar to the appearance of striations reported for a PM steel alloy by Chawla [2001]. However, after analysis and comparison with the monotonic fracture surface, we observed the same microstructural features on both monotonic and fatigue fracture surfaces. Hence, the "striations" were not striations at all.

The fracture surfaces of the fatigue specimens referenced as Specimens A, B, and C in Figure 5.2 are shown in Figures 5.3, 5.4, and 5.5, respectively.

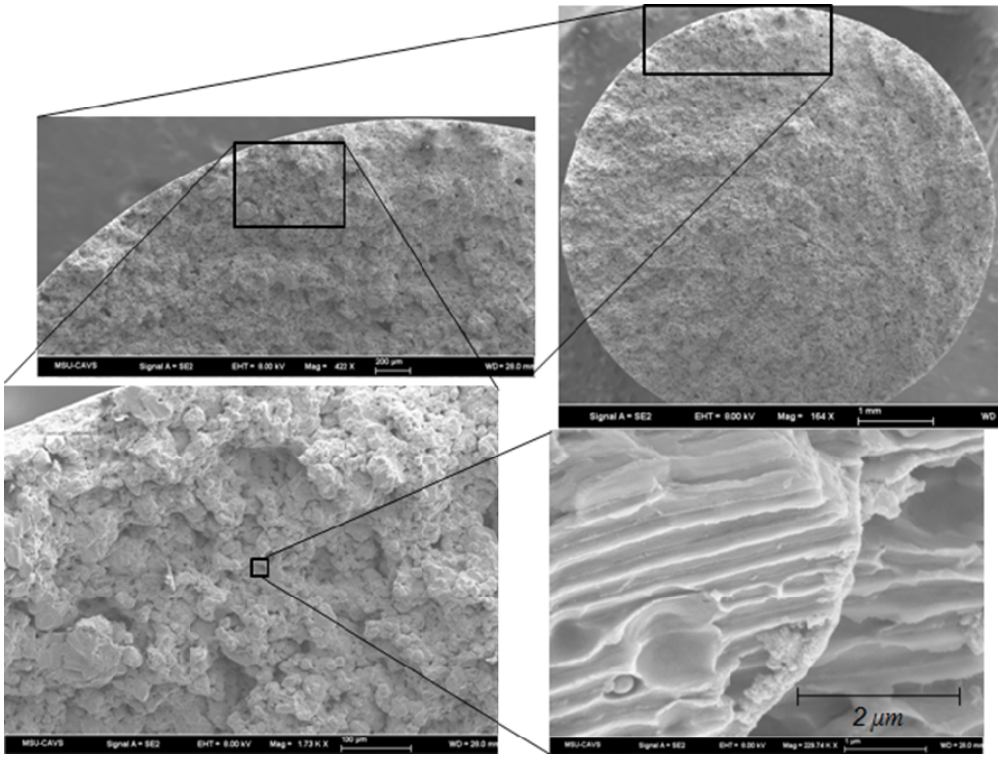

Figure 5.3 Fracture surfaces of fatigue Specimen A.

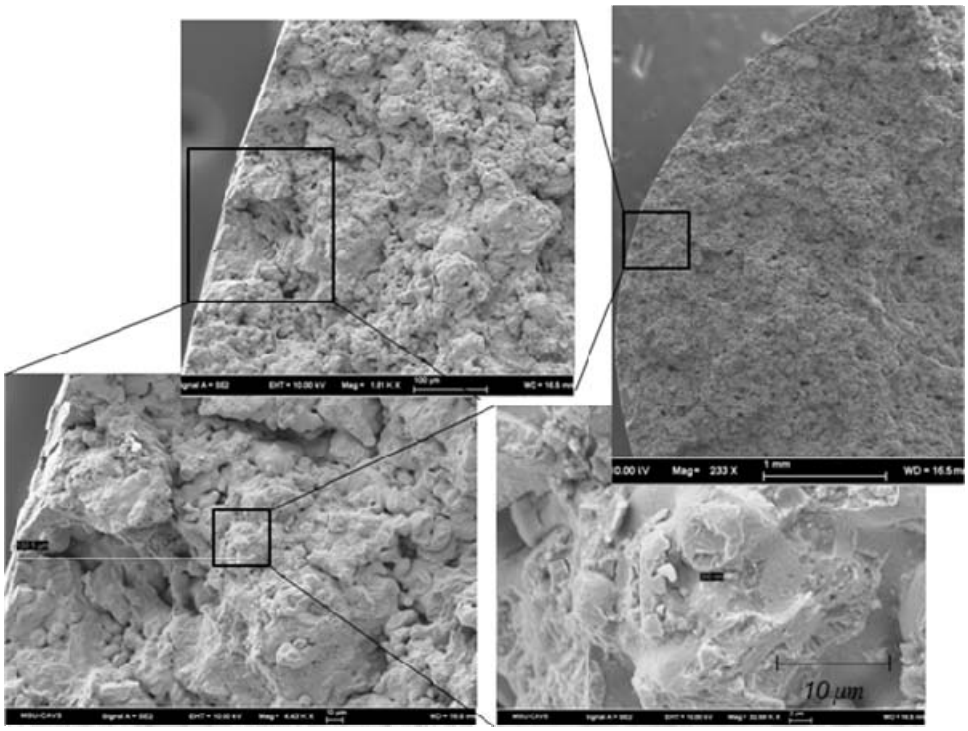

Figure 5.4 Fracture surfaces of fatigue Specimen B.

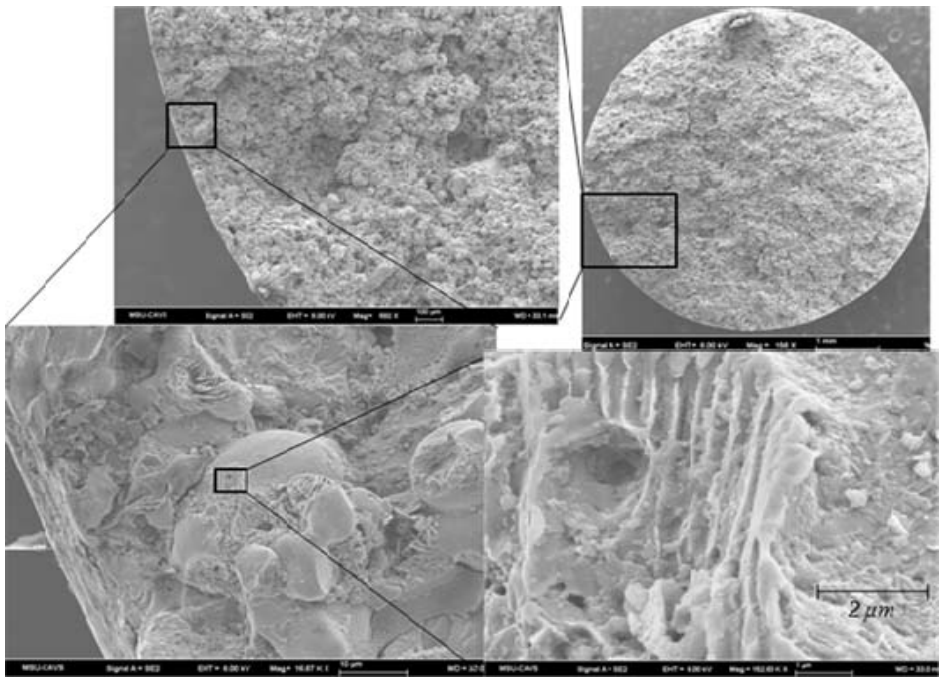

Figure 5.5 Fracture surfaces of fatigue Specimen C.

The magnified images of the fatigued specimens in Figure 5.3-5.5 reveal some microstructural features that appear to be fatigue striations. However, the same microstructural features are evident when compared to images of the fracture surfaces of the monotonic tensile sample shown in Figure 5.6. Thus, we cannot say definitively that these microstructural features are fatigue striations. Therefore, the determination of the location of crack initiation from analyzing the fatigue striation patterns is hindered by the lack of clear and concise striations on the fatigue specimen fracture surface.

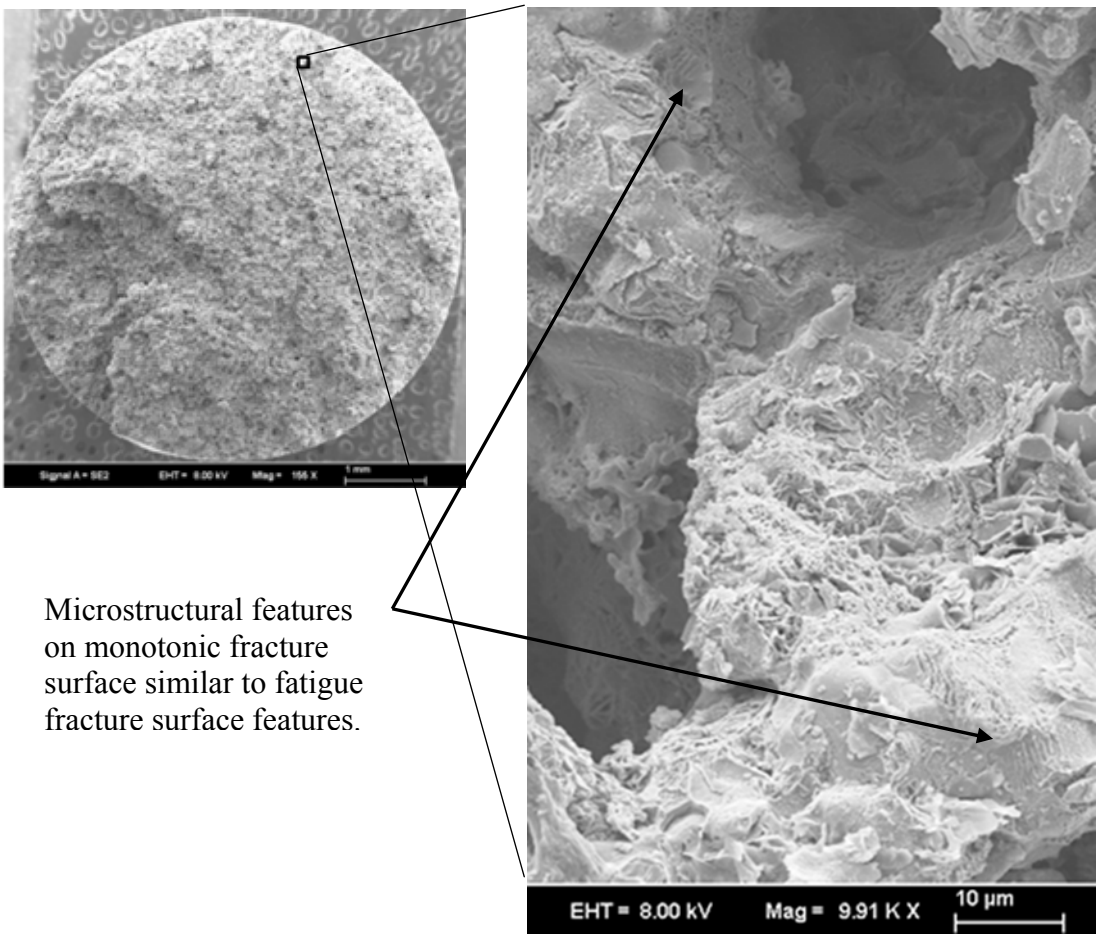

Figure 5.6 Monotonic tension specimen with microstructural features similar to uniaxial fatigue specimens. (zoom in on appeared striations)

The microstructure quantification of the fatigue fracture surfaces are provided for the macrovoids and microvoids in Table 5.1 and Table 5.2, respectively by using the image analysis software developed by Williams and Carino (2007).

Table 5.1 Macrovoid fatigue fracture surface characteristics.

Initial Porosity Level	Temperature (K)	Volume Fraction Macro-voids	Average NND (μm)	Maximum NND (μm)	Average Pore Diameter (μm)	Maximum Pore Diameter (μm)
Low	293	0.37	6.08	41.34	4.25	210.54
High	293	0.40	5.13	28.48	3.45	288.84

Table 5.2 Microvoid fatigue fracture surface characteristics.

Initial Porosity Level	Temperature (K)	Volume Fraction Micro-voids	Average NND (μm)	Maximum NND (μm)	Average Pore Diameter (μm)	Maximum Pore Diameter (μm)	Inter-void Ligament Distance (μm)
Low	293	0.86	0.40	1.27	0.33	7.19	0.07
High	293	0.87	0.25	1.96	0.13	7.14	0.12

A considerably lower volume fraction for the macrovoid fracture surface is shown in Table 5.1 when compared to the microvoid characteristics of Table 5.2, while there is not much difference between the low porosity and high porosity specimens' volume fraction. The average nearest neighbor distance (NND), the distance between the center of two pores, and average pore diameter is lower for the specimens with the higher initial porosity at both length scales. Macrovoid quantification of the maximum NND at the macroscale displays a greater value for the low initial porosity specimens, while the opposite trend is observed at the microscale. Fracture surfaces of the macrovoid showed the high initial porosity specimens containing the larger maximum pore diameters while the opposite was seen at the microvoid level. The microvoid fracture surfaces had the intervoid ligament distance (IVL), distance between the closest edge of two neighboring pores, where the higher initial porosity specimens contained a larger IVL.

Model Calibration

In this section, we discuss the MultiStage Fatigue (MSF) model that was developed during the previous USCAR PNGV program for aluminum cast alloys [Horstemeyer et al., 2001; McDowell et al., 2003]) and further enhanced for magnesium alloys [Horstemeyer et al. 2006]. Since the PM alloys discussed in this report have similar microstructures and inclusions/defects, we surmised that the modeling framework would be general enough to capture the fatigue behavior of these various PM alloys. However, we had to make to minor revisions to the model to account for the porosity degradation of the elastic modulus and void coalescence as it relates more directly to the nearest neighbor distance. The MSF model was fundamentally based on micromechanics simulations [Fan et al., 2001; Gall et al., 2000] and small-scale experiments for mechanical properties of small crack growth (Horstemeyer, 1998; Gall et al., 1999; Gall et al, 2000]. It was further generalized to incorporate material properties and microstructure relations for an incubation model [Xue et al., 2006]. In this model, high cycle fatigue (HCF) and low cycle fatigue (LCF) are both driven mainly by the porosity within the powder metal.

At the pores, the stress field concentration was described by the average plastic strain level that captured the loading history. This constrained microplasticity at the notch root, *e.g*. pore or particles, incubated and caused growth of the microstructurally small fatigue cracks during HCF. The growth of microstructurally small cracks (MSC) was dominated by the crack tip opening displacements, which is proportional to the crack size and $(\sigma_a)^n$, where n is a constant [Naitini and Goto, 1987; Shiozawa et al., 1997].

The long crack propagates to material failure according to linear elastic fracture mechanics with an associated number of cycles [Newman, 1994]. The total fatigue life, defined as cycles to failure, is modeled as the cumulative number of cycles spent in these consecutive stages as follows:

$$N_T = N_{inc} + N_{MSC} + N_{LC} \tag{5.1}$$

where N_{inc} is the number of cycles to incubate a crack (nucleation plus small crack growth through the region of notch root influence) of a micronotch scale crack with initial length, a_{i}, on the order of half of the maximum inclusion diameter. The incubation of the crack-life damage around the local discontinuity was induced by the local highly concentrated microplasticity such that a modified Coffin-Manson law was implemented with the ductility coefficient as a function of the local maximum plastic shear strain. N_{MSC} is the number of cycles required for propagation of a microstructurally small crack (MSC) with length $a_{\text{i}}<a<k$ DCS (dendrite cell size or grain size), where k is a nondimensional factor that represents a saturation limit when the three-dimensional crack front encounters a network of inclusion particles. The growth of MSC is dominated by the crack tip opening displacements, which is proportional to the crack size. The long crack propagates according to linear elastic fracture mechanics with an associated number of cycles N_{LC}. It should be noted that the incubation life was specifically formulated as a function of inclusion severity scale in terms of the ratio of the constrained microplasticity zone to the size of inclusion particles [McDowell et al., 2003].

In the MSF model, the total life was divided into three parts as shown in Eq. (5.1). The incubation model was developed with the combination of micromechanics finite element analysis and damage initiation experiments as mentioned earlier,

$$C_{inc} N_{inc}^{\alpha} = \beta = \frac{\gamma_{\max}^{P}}{2} \tag{5.2}$$

where β is the local maximum plastic shear strain amplitude around the inclusion, C_{inc}, and α are the linear and exponential coefficients in modified Coffin-Mansion law for incubation. C_{inc} is a function of local maximum plastic shear strain. The local maximum plastic shear strain amplitudes were obtained using finite element analysis on a reprehensive volumetric unit cell that contains various inclusions [Gall et al., 2000], that is

$$\beta = \frac{\Delta\gamma_{\max}^{P}}{2} = Y[100(\bar{\varepsilon}_a - \varepsilon_{th})]^q \left[\frac{MPS}{NND * GS}\right]^{\xi}, \quad \frac{l}{D} < \eta_{\lim} * \tag{5.3}$$

$$\beta = \frac{\Delta\gamma_{\max}^{P}}{2} = \max\left\{\frac{\Delta\gamma_{\max}^{P^*}}{2}, \bar{Y}[100(\varepsilon_{per} - \varepsilon_{th})]^q \left[\frac{MPS}{NND * GS}\right]^{\xi}\right\}, \quad \eta_{\lim} < \frac{l}{D} < 1 \tag{5.4}$$

where $\bar{\varepsilon}_a$, ε_{th}, and ε_{per} are the remote loading strain amplitude (von Mises equivalent strain for three-dimensional loading cases), the strain threshold for damage incubation, and the strain percolation limits for microplasticity, respectively. D is the averaged diameter of the inclusions, projected to the direction perpendicular to the loading direction, that incubated the fatigue damage, such as debonded or fractured particles or pores, and l is the plastic zone size in the front of the inclusion projected to the direction

perpendicular to the loading. The ratio l/D was used to quantify the micronotch root plasticity due to the inclusions. The limiting factor for this ratio, $\eta_{\lim}$, indicated that the transition from the proportional micronotch root plasticity to nonlinear micronotch root plasticity with respect to the applied strain amplitude. The correlation of the local plastic shear strain range with respect to the remote loading strain is developed a using finite element simulation, so are the forms of *Y*, *q*, and $\eta_{\lim}$. The parameter *Y* includes the load ratio effect in terms of $Y = y_1 + (1+R)y_2$ where *R* is the load ratio and y_1 and y_2 are model constants. Further, when l/D reached its limits, the parameter *Y* was revised to include the geometric effects $\bar{Y} = (1+\xi)Y$. Here, we used the estimated fatigue "limit" that corresponding to the strain amplitude gives 10^7 cycles to failure to mimic the strain threshold for damage incubation. The percolation limit for microplasticity denotes that the incubation becomes an insignificant part of the total fatigue life as the extensive shear localization becomes dominant in the region near the inclusions. The correlation of the plastic zone size is calculated using the nonlocal plastic shear strain with the remote loading strain amplitude.

$$\frac{l}{D} = \frac{\langle \bar{\varepsilon}_a - \varepsilon_{\text{th}} \rangle}{\text{c}}, \quad \frac{l}{D} < \eta_{\lim} \tag{5.5}$$

$$\frac{l}{D} = 1 - \xi \left(\frac{\varepsilon_{per}}{\bar{\varepsilon}_a} \right)^{\frac{1}{r}}, \quad \eta_{\lim} < \frac{l}{D} < 1 \tag{5.6}$$

where *r* is a shape constant for the transition to the limited plasticity, *c* is a model constant, and ξ is the linear factor. The development of the MSF model presented in this

document is focused on incubation and MSC growth around pores. The MSC growth was characterized into the crack tip opening displacement.

$$\left(\frac{da}{dN}\right)_{MSC} = \chi\left[\frac{MPS}{NND * GS}\right]^{\xi}\left(\Delta CTOD - \Delta CTOD_{th}\right) \tag{5.7}$$

$$\Delta CTD = f(\phi)C_{11}\left[\frac{U\Delta\hat{\sigma}}{S_{ut}}\right]^{\zeta} a + C_1\left(\frac{\Delta\gamma_{\max}}{2}\right)^2 \tag{5.8}$$

where χ is a constant for a given microstructure, typically less than unity and usually taken as 0.32 for aluminum alloys, $\Delta CTOL$ is the crack tip opening displacement, equivalent stress defined as $\Delta\hat{\sigma} = \theta_1\left[\frac{3}{2}\frac{\Delta\sigma'_{ij}}{2}\frac{\Delta\sigma'_{ij}}{2}\right]^{0.5} + \theta_2\Delta\sigma_1$, the porosity in front of the crack is defined as $f(\phi) = 1 + \omega\left\{1 - \exp\left(-\frac{\bar{\phi}}{2\phi_{th}}\right)\right\}$, U is the load ration parameter as $U = \frac{1}{1+R}$, and C_1, C_{11}, and ζ are material dependent parameters. The Modified Paris law, a linear elastic fracture mechanics based crack growth model, was used for long crack growth model, that is

$$\frac{da}{dN} = C\left[\left(\Delta K_{\text{eff}}\right)^m - \left(\Delta K_{\text{th,eff}}\right)^m\right] \tag{5.9}$$

where C and m are material constants and a function of R-ratio and local plasticity. The stress intensity factor could be obtained based on the linear elastic fracture mechanics model and a geometric factor for cylindrical specimens with semi-circular surface cracks, as

$$K_{\max} = f\left(\frac{a}{d}\right)\sigma_{\max}\sqrt{\pi a} \tag{5.10}$$

$$f\left(\frac{a}{d}\right) = 0.67 - 1.24\left(\frac{a}{d}\right) + 28.0\left(\frac{a}{d}\right)^2 - 162.4\left(\frac{a}{d}\right)^3 +$$

$$+ 472.2\left(\frac{a}{d}\right)^4 - 629.6\left(\frac{a}{d}\right)^5 + 326.1\left(\frac{a}{d}\right)^6 \tag{5.11}$$

where d is the diameter of the cylindrical specimen. The transition from MSC growth to LC growth is based on the following notion,

$$\frac{da}{dN} = \max\left[\left(\frac{da}{dN}\right)_{\text{MSC}}, \left(\frac{da}{dN}\right)_{\text{LC}}\right] \tag{5.12}$$

For the K_{t1} type specimens described earlier nearly all of the fatigue life comprises incubation with some microstructurally small cracks. For the main bearing cap, the long crack regime will experience some cycles. Figure 5.7 shows a comparison of how the model can capture the strain-life phenomena with different porosity levels. The model shows good correlations with the experimental data for both porosity levels plotted.

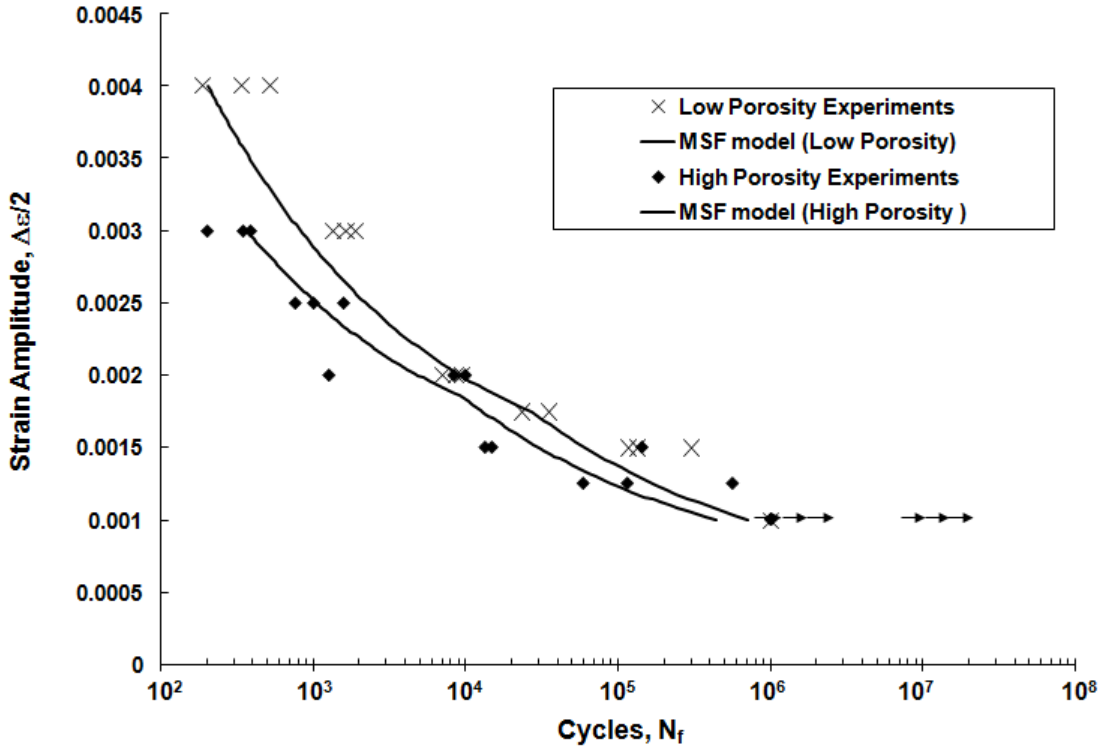

Figure 5.7 MultiStage Fatigue (MSF) model calibration with low and high porosity fatigue experimental data.

Conclusions

Uniaxial fatigue experiments conducted on specimens with low and high initial porosity levels were used to calibrate a microstructurally-based multistage fatigue model. The strain-life behavior of the experiments displayed that above the plastic strain limit of 0.002 mm/mm, where ubiquitous plasticity occurs, the two porosity levels are distinctly visible. However, specimens tested below the plastic limit, where failure is dominated by local cyclic plasticity, shows unclear distinctions between the two porosity levels. Analysis of the fracture surfaces did not clearly depict the presence of striations due to

similar geometrical features being observed on the fracture surface of monotonically loaded specimens.

Material model constants were determined using experimental and microstructure data that allowed for satisfactory prediction of the high and low porosity specimens strain-life curves. The MSF model constants were then used by Dr. Hammi at Mississippi State University's Center for Advanced Vehicular Systems to validate the model with automotive main bearing cap fatigue experiments, which are being published in a separate study.

CHAPTER VI

SUMMARY AND FUTURE WORK

Summary

Monotonic and fatigue loading of a powder metallurgy steel were performed to calibrate and validate a microstructurally-based internal state variable (ISV) plasticity-damage model and a microstructurally-based multistage fatigue (MSF) model. These specific models were previously developed and used for cast and wrought materials and this was their first application to powder metallurgy materials.

The ISV model was calibrated using experimental results with varying stress state, strain rate, and temperatures at low and high initial porosity levels. For each experiment, microstructure quantification was performed for the initial state of the material and the fracture surface of the specimen using optical and scanning electron microscopy. In turn, the microstructure data was then used in calibration of the ISV model. A theoretical study of elastic constants dependence on porosity allowed for a more accurate expression of porosity dependence modulus by McAdam (1950) to be implemented into the updated ISV model. Additionally, a new physically motivated coalescence ISV equation was included to capture the local stress interaction influenced by the intervoid ligament distance of neighboring pores due to the highly porous nature of

powder metals. Satisfactory agreement between model and experimental monotonic results justified the next step of validating the model with additional experimental tests.

Notched tensile specimens with different triaxiality levels and monotonic tensile loading of automotive main bearing caps were tested to validate the model. Prediction of the notch tensile load versus displacement experimental results by the model curves were obtained for the varying triaxiality levels. The location of damage initiation on the main bearing caps and the experimental results were further predicted by the model validating the models ability to be used for materials with inhomogeneous porosity distributions.

Uniaxial fatigue experiments were conducted at ambient temperature in-order to generate strain-life curves for specimens with two different initial porosity levels. Microstructural quantification was also performed on the fatigue specimens for calibration of the MSF model. Experimental results showed that above the plastic strain limit of 0.002 mm/mm, where ubiquitous plasticity occurs, the effects of the two porosity levels are distinctly visible. However, specimens tested below the plastic limit, where failure is dominated by local cyclic plasticity, showed no clear distinctions between the two porosity levels. Determination of the MSF model constants resulted in accurate predictions of the high and low porosity specimens strain-life curves.

Future Work

Calibration of the ISV model discussed in Chapter IV was limited to high rate compression specimens. Additional testing of tension and torsion high rate coupons

should allow for the ISV model to more accurately predict strain rate effects on PM materials.

Further fatigue studies would also be beneficial to the scientific community. Specifically, a study of the Bauschinger effect for FC-0205 PM steel could be extrapolated from the experimental data used in this study. The characterization of fracture behavior for FC-0205 using in-situ SEM would allow for the MSF model to be compared with how many cycles are experimentally observed at the individual stages of incubation, microstructurally/physically small crack, and long crack.

Finally, the calibration of the ISV plasticity-damage model and the MSF model with aluminum PM material is needed to develop a bearing cap with an improved property to weight ratio.

REFERENCES

(2000). Materials standards for PM structural parts. MPIF Standard. Princeton, NJ, Metal Powders Industries Federation. **35**.

Allison, P. G., H. Grewal, M. F. Horstemeyer, Y. Hammi and H. R. Brown (Under Review). "Modeling and experimental study of the plasticity and fracture of a powder metal steel (FC-0205) under various strain rates, temperatures, and stress states." Journal of Engineering Materials and Technology.

Aly, M. S. (2005). "How metal foams behave if the temperature rises." Metal Powder Report **60**(9): 38-45.

ASM (2000). ASM Handbook. Mechanical Testing. Metals Park, American Society for Metals. **8:** 50-51.

ASTM (2004). ASTM E8-04 Standard test methods for tension testing of metallic materials.

Bammann, D. J. (1984). "An internal variable model of viscoplasticity." International Journal of Engineering Science **22**(8-10): 1041-1053.

Bammann, D. J. (1990). "Modeling temperature and strain rate dependent large deformations of metals." Applied Mechanics Review 43 **5**(Part 2): 312-319.

Bammann, D. J. and E. C. Aifantis (1989). "A damage model for ductile metals." Nuclear Engineering & Design **116**: 355-362.

Bammann, D. J., M. L. Chiesa, M. F. Horstemeyer and L. I. Weingarten (1993). Failure in ductile materials using finite element methods. Structural Crashworthiness and Failure. N. Jones and T. Weirzbicki. Amsterdam, Elsevier**:** 1-54.

Bammann, D. J., M. L. Chiesa, M. F. Horstemeyer and L. I. Weingarten (1993). Failure in ductile materials using finite element methods. Structural Crashworthiness and Failure. N. Jones and T. Wierzbicki**:** 1-54.

Bammann, D. J., M. L. Chiesa and G. C. Johnson (1997). Modeling large deformation and failure in manufacturing processes. Theoretical and Applied Mechanics. T. Tatsumi, E. Watanabe and T. Kambe**:** 359-376.

Bert, C. W. (1985). "Prediction of elastic moduli of solids with oriented porosity." Journal of Materials Science **20**(6): 2220-24.

Buch, A. and S. Goldschimdt (1970). "Influence of porosity on elastic moduli of sintered materials." Materials Science and Engineering A **5**(2): 111-118.

Budiansky, B. (1965). "On the elastic moduli of some heterogeneous materials." Journal of Mechanics and Physics of Solids **13**(4): 223-27.

Chawla, N. and X. Deng (2005). "Microstructure and mechanical behavior of porous sintered steels." Materials Science and Engineering A **390**: 98-112.

Chawla, N., T. F. Murphy, K. S. Narasimhan, M. Koopman and K. K. Chawla (2001). "Axial fatigue behavior of binder-treated versus diffusion alloyed powder metallurgy steels." Materials Science and Engineering A **308**: 180-188.

Christian, K. D. and R. M. German (1995). "Relation between pore structure and fatigue behavior in sintered iron-copper-carbon." International Journal of Powder Metallurgy **31**(1): 51-62.

Cocks, A. C. F. and M. F. Ashby (1982). "On creep fracture by void growth." Prog. Mater. Sci. **27**: 189-244.

Dustoor, M. R., A. C. Taylor and R. M. German (1989). "An assessment of high temperature sintering and the alternatives." Advances in Powder Metallurgy **1**: 203-222.

Engler-Pinto Jr., C. C., J. V. Lasecki, R. J. Frisch Sr., M. A. DeJack and J. E. Allison (2006). "Statistical approaches applied to fatigue data analysis." SAE Transactions: Journal of Materials & Manufacturing **114**: 422-431.

Fedorchenko, I. M., Y. F. Shevehuk, V. N. Miroshnikov and V. A. Borisenko (1976). "Elevated temperature mechanical properties of sintered iron-base materials containing calcium flouride additions." Soviet powder metallurgy and metal ceramics **15**(3): 238-242.

Firstov, S. A., E. P. Pechkovsky, I. I. Ivanova, N. P. Brodnikovsky, V. F. Gorban and A. N. Demidik (2006). "High-temperature mechanical properties of powder

metallurgy: Porous lightweight titanium nanolaminates." High Temperature Materials and Processes **25**(1): 47-58.

Gary, G. (2005). "DAVID Manual." from http://www.lms.polytechnique.fr/dynamique/greef/web4034_david.html.

German, R. M. (1996). Sintering theory and practice. New York, John Wiley & Sons, Inc.

German, R. M. (2005). Powder metallurgy and particulate materials processing. Princeton, MPIF.

Hadrboletz, A. and B. Weiss (1997). "Fatigue behaviour [sic] of iron based sintered material: a review." International Materials Reviews **42**(1): 1-44.

Hammi, Y., T. Y. Stone and M. F. Horstemeyer (2006). "Constitutive modeling of metal powder behavior during compaction." SAE Transactions: Journal of Materials & Manufacturing: 293-299.

Hardin, R. A. and C. Beckermann (2007). "Effect of porosity on the stiffness of cast steel." Metallurgical and Materials Transactions A **38A**: 2992-3006.

Hashin, Z. (1962). "The elastic moduli of heterogeneous materials." Journal of Applied Mechanics **29**(1): 143-50.

Hashin, Z. and S. Shtrikman (1963). "A variational approach to the theory of the elastic behavior of multiphase materials." Journal of Mechanics and Physics of Solids **11**(2): 127.

Haynes, R. (1981). The Mechanical Behaviour of Sintered Metals. London, Freund.

Hill, R. (1965). "A self-consistent mechanics of composite materials." Journal of Mechanics and Physics of Solids **13**(4): 213-22.

Horstemeyer, M. F. (2001). From atoms to autos: a new design paradigm using microstructure-property modeling. Part 1: monotonic loading conditions. Livermore, Sandia Nat. Labs.

Horstemeyer, M. F. and A. M. Gokhale (1999). "A void-crack nucleation model for ductile metals." International Journal of Solids and Structures **36**: 5029-5055.

Horstemeyer, M. F., J. Lathrop, A. M. Gokhale and M. Dighe (2000). "Modeling stress state dependent damage evolution in a cast Al-Si-Mg aluminum alloy." Theoretical & Applied Fracture Mechanics **33**: 31-47.

Horstemeyer, M. F., M. M. Matalanis, A. M. Sieber and M. L. Botos (2000). "Micromechanical finite element calculations of temperature and void configuration effects on void growth and coalescence." International Journal of Plasticity **16**: 979-1015.

Iacoviello, F., D. Iacoviello and M. Cavallini (2004). "Analysis of stress ratio effects on fatigue propagation in a sintered duplex steel by experimentation and artificial neural network approaches." International Journal of Fatigue **26**: 819-828.

Kalashnikova, O. Y., I. A. Gulyaev and E. I. Dovgan (2004). "Feasibility of reducing the porosity of steels made from partially alloyed iron powder." Metallurgist **48**(1-2): 31-37.

Klumpp, S., D. Eifler, O. Vohringer and E. Macherauch (1992). Cyclic deformation behaviour [sic] of sintered pure and alloyed iron. Powder Metallurgy Conference & Exhibition, Princeton, NJ.

Kroner, E. (1960). "Allgemeine kontinuumstheorie der versetzungen und eigenspannungen." Archive for Rational Mechanics and Analysis **4**: 273-334.

Lee, E. H. (1969). "Elastic plastic deformation at finite strain." ASME, Journal of Applied Mechanics **36**: 1-6.

Lemaitre, J. and J. Dufailly (1987). Damage Measurements.

Lemaitre, J. and J. Dufailly (1987). "Damage measurements." Engineering Fracture Mechanics **28**(5/6): 643-661.

Lin, S.-K., Y.-L. Lee and M.-W. Lu (2001). "Evaluation of the staircase and the accelerated test methods for fatigue limit distributions." International Journal of Fatigue **23**: 75-83.

Lindstedt, U., B. Karlsson and R. Masini (1997). "Influence of porosity on deformation and fatigue behavior of PM austenitic stainless steel." International Journal of Powder Metallurgy **33**(8): 49-61.

Lowhaphandu, P. and J. J. Lewandowski (1999). "Fatigue and fracture of porous steels and Cu-infiltrated porous steels." Metallurgical and Materials Transactions A **30A**: 325-334.

Mackenzie, J. H. (1950). "The elastic constants of a solid containing spherical holes." Proceedings of the Physical Society **63**(1): 2-11.

McAdam, G. D. (1950). "Some relations of powder characteristics to the elastic modulus and shrinkage of sintered ferrous compacts." Journal of the Iron and Steel Institute **168**: 346.

McClintock, F. A. (1968). "A criterion for ductile fracture by void growth of holes." ASME, Journal of Applied Mechanics **35**: 363-371.

Metaldyne. (2007). "FC-0205 powder metal production." from http://metaldyne.com.

O'Brien, R. C. (1988). Fatigue properties of PM materials. SAE Congress. Detriot, MI, SAE.

Poland, D. D., R. I. Stephens and T. Prucher (1998). "Influence of density and sintering temperature on smooth, notched, and cracked variable amplitude fatigue behaviour [sic] of FL4405 high strength PM steel." Powder Metallurgy **41**(4): 274-280.

Polasik, S. J., J. J. Willliams and N. Chawla (2002). "Fatigue crack initiation and propagation of binder-treated powder metallurgy steels." Metallurgical and Materials Transactions A **33**(1): 73-81.

Ramakrishnan, N. and V. S. Arunachalam (1993). "Effective elastic moduli of porous cermaic materials." Journal of American Ceramic Society **76**(11): 2745-52.

Saritas, S., R. Causton, B. W. James and A. Lawley (2005). "Rotating-bending fatigue of pre-alloyed and hybrid P/M steels." International Journal of Powder Metallurgy **41**(3): 63-70.

Spitzig, W. A., R. E. Smelser and O. Richmond (1988). "The evolution of damage and fracture in iron compacts with various initial porosities." Acta Materialia **36**(5): 1201-11.

Stone, T. Y., L. Tucker, Y. Hammi, T. N. Williams, H. El Kadiri and M. F. Horstemeyer (2009). "Comparison of density measurement techniques for large PM components." Journal of Powder Metallurgy **Under Review**.

Stossel, R. J. and T. Prucher (1993). Comparison of tensile and torsion properties of PM steels. International Conf. & Exhibition on Powder Metallurgy & Particulate Materials, MPIF.

Sudhakar, K. V. (2000). "Fatigue behavior of a high density powder metallurgy steel." International Journal of Fatigue **22**: 729-734.

Torres, Y., S. Rodriguez, A. Mateo, M. Anglada and L. Llanes (2004). "Fatigue behavior of powder metallurgy high-speed steels: fatigue limit prediction using a crack growth threshold-based approach." Materials Science and Engineering A **387-389**: 501-504.

Walpole, L. J. (1969). "On the overall elastic moduli of composite materials." Journal of Mechanics and Physics of Solids **17**(4): 235-251.

Williams, C. R., Y.-L. Lee and J. T. Rilly (2003). "A practical method for statistical analysis of strain-life fatigue data." International Journal of Fatigue **25**: 427-436.

Williams, T. N. and R. L. Carino. (2007). "Image analyzer - a software tool for calculating certain material model constants from optical images."

Yan, X.-J., H.-Y. Li and J.-X. Nie (2004). "A probabilistic model for prediction of LCF life of PM alloys." Aircraft Engineering and Aerospace Technology **76**(3): 286-292.

Yeh, R. H. T. (1970). "Variational principles of the elastic moduli of composite materials." Journal of Applied Physics **41**(8): 3353-56.

Yu, C. J. and T. Prucher (1993). "Measuring Young's modulus and shear modulus - A comparison of dynamic and mechanical techniques." Advances in Powder Metallurgy & Particulate Materials **1**: 273-286.

APPENDIX A

MICROSTRUCTURE-PROPERTY (ELASTIC-PLASTIC) MODEL CONSTANTS FOR FC-0205

Table A.1 Microstructure-property (elastic-plastic) model constants for FC-0205

	Constants	
Material property information	G (MPa)	80,384
	a	0
	Bulk (MPa)	174,167
	b	0
	Melting temp (K)	1,811
Specifies the yield stress	C1 (MPa)	0
	C2 (K)	0
	C3 (MPa)	376
	C4 (K)	0
	C5 (1/MPa)	1e-5
	C6 (K)	0
Kinematic hardening and recovery terms	C7 (1/MPa)	1.47
	C8 (K)	87.5
	C9 (MPa)	59,000
	C10 (K)	0.75
	C11 (s/MPa)	0
	C12 (K)	0
Isotropic hardening and recovery terms	C13 (1/MPa)	0.01
	C14 (K)	14
	C15 (MPa)	7800
	C16 (K)	0.04
	C17 (s/MPa)	0
	C18 (K)	0
Hardening and recover cons.	Ca	-9.1
	Cb	-0.35
Temperature	Init. Temp (K)	293
	Heat gen. coeff	0.34

Table A.2 Microstructure-property (damage) model constants for FC-0205.

	Constants	**High initial porosity**	**Low initial porosity**
McClintock void growth	Void growth exp	0.3	0.3
	Init. radius (mm)	0.0055	0.0035
Nucleation	a	1	1
	b	1	1
	c	1	1
	Nuc coeff	2e-006	2e-006
	Fract. toughness MPa (m^1/2)	40	40
	Part. Size (mm)	0	0
	Part. vol fract.	0	0
Coalescence	Nearest Neighbor Distance (mm)	0.0103	0.0098
	Zeta	4	4
	Init. void vol. fract.	0.19	0.09
CA pore growth	void growth constant	16	16
Nucleation	Nuc. temp. depend.	0	0
Yield strength adjustment terms	c19	0	0
	c20	0	0
Modulus-porosity adjustment term	β	3	3

APPENDIX B

MSF MODEL CONSTANTS FOR FC-0205 POWDER METALLURGY STEEL

Table B.1 Multi-Stage Fatigue model constants for FC-0205 powder metallurgy steel.

Properties	upper bound	lower bound
Syld (MPa)	400	320
z	4.80	4.80
a	-0.6	-0.6
C_m	0.64	0.64
CTD_{th}	0.0002860	0.0002860
CI (in microns)	80000	80000
CII (in microns)	3.66	3.66
GS (microns)	12	12
NND (microns)	8.92	8.46
MPS (microns)	267	448
Porosity (%)	9	19
CNC	0.5	0.5
ω	2	2
r	0.3	0.3
q	2.30	2.30
y1	165	165
y2	300	300
θ	0.25	0.25
β	3	3